NORTHWESTERN UNIVERSITY

Photophysics of Colloidal Two-Dimensional Semiconductor Nanoparticles

A DISSERTATION

SUBMITTED TO THE GRADUATE SCHOOL
IN PARTIAL FULFILLMENT OF THE REQUIREMENTS

for the degree

DOCTOR OF PHILOSOPHY

Field of Chemistry

By
Alexandra Brumberg

EVANSTON, ILLINOIS

September 2021

Abstract

Recent progress in the field of nanomaterials has enabled significant advances in optoelectronic devices such as solar cells, light-emitting diodes, photocatalysts, and sensors. Nanoparticles feature superior optical and electronic properties that arise from quantum confinement and therefore cannot be attained used bulk materials. However, further developments in the field of nanotechnology require increased knowledge regarding how to further improve the properties of these novel materials. Because nanoparticles are quantum confined, methods of altering nanoparticles properties extend beyond just changes of material composition to also those of nanoparticle size and shape. The modification of shape is especially useful when it involves changing the number of nanoscale dimensions, as quantum confinement in one, two, or three dimensions results in drastically different optical and electronic properties. However, because the electronic behavior of one- and two-dimensional nanomaterials is not captured by either that of nanoparticles confined in all three dimensions (i.e. zero-dimensional nanomaterials), nor by that of bulk materials, experimental investigations into their photophysical behaviors are needed to gain fundamental understanding regarding how nanoparticle dimensionality affects optoelectronic behavior.

This dissertation investigates the effect of nanoparticle dimensionality on the photophysical behavior of semiconductor nanoplatelets (NPLs)—colloidal, two-dimensional nanoparticles that are quantum confined in only one dimension. In each study, time-resolved spectroscopy is employed to characterize the optical or structural properties of CdSe NPLs following photoexcitation, in order to gain insight into the behavior of NPLs in conditions relevant to optoelectronic applications. In the first study, a magneto-optical experiment is used to determine the lateral spatial extent of the excited electron-hole pair ("exciton"), which dictates electronic interactions between NPLs and other materials. Although the exciton in two-dimensional materials is often assumed to be spatially extended throughout the plane of the material, we show that the exciton in CdSe NPLs is relatively spherical in shape.

An example of a type of electronic interaction that is affected by exciton spatial extent is demonstrated in the study of electron transfer between pairs of nanoparticles with varied dimensionalities presented in the following chapter, which reveals that systems containing NPLs undergo charge transfer more rapidly than those containing zero-dimensional particles ("quantum dots"). Another type of electronic interaction is that of Auger recombination, an undesirable process through which excess electronic energy is transferred to a third carrier (either an electron or hole) instead of light. Here, we investigate the scaling of rates of Auger recombination with respect to NPL size, revealing that the universal volume scaling relationship present for zero- and one-dimensional nanoparticles does not carry over to two-dimensional NPLs. Furthermore, despite the common assumption that multiexciton recombination is dominated by nonradiative (Auger) recombination in quantum-confined systems, measurements of Auger lifetimes as a function of temperature reveal that multiexcitons become radiative at low temperatures in NPLs.

Finally, the effect of intense photoexcitation on NPL crystal structure (and therefore optoelectronic properties) is probed using time-resolved X-ray diffraction, revealing that, following photoexcitation, the NPL lattice loses crystallinity more significantly in the out-of-plane direction than in the in-plane direction. Although this is cause for concern as the out-of-plane direction is the one that dictates optoelectronic properties, the excitation intensity required to induce disordering in NPLs is significantly higher than that observed for quantum dots, suggesting NPLs are still the more promising material for optoelectronics. Together, the studies in this dissertation delve into many of the photophysical processes that bear relevance to optoelectronic devices, showing that nanoparticle dimensionality is an important factor to consider in the design of nanotechnology.

Acknowledgements

First and foremost, I would like to acknowledge Prof. Richard Schaller, who oversaw the entirety of my Ph.D. Under his guidance, I have been able to explore as many topics as I've wanted, and potentially more than I should at any one time, and that has been the most exhilarating experience.

Second, I have been extremely fortunate to have found a second home at the Center for Nanoscale Materials replete with a number of secondary advisors who are more than willing to help young scientists with ambitious projects. Benjamin Diroll has been my unofficial mentor throughout my time at the CNM, and I will strive to match his productivity and expansive extent of knowledge as I move on to my postdoctoral studies. In addition, Dave Gosztola has spent countless hours helping me on more projects than will ever be recognized—but let it at least be stated here that Dave taught me how to operate many instruments and resulted in the collection of many piles of unpublished data that have undoubtedly contributed to my growth as a scientist.

I joined the Schaller group at a time when there was only one graduate student, prepared full well for a rather isolating office environment. Instead, I was joined by three peers in my year who made my graduate experience far from isolating. Samantha Harvey, Ariel Leonard, and Nicolas Watkins have been absolutely central to my graduate school experience; I had three friends to share my experiences with along the way, and three labmates to challenge me and keep me motivated, too. In addition, Matthew Kirschner deserves significant acknowledgement for the huge undertaking of the onboarding four new students. Throughout my Ph.D., you have remained someone I look up for how much you were able to accomplish in graduate school, and for just how good at MATLAB you are.

Meanwhile, it has been an absolute delight welcoming Shelby Cuthriell and Shobhana Panuganti to the group, and even further seeing the group expand once again with the additions of Caitlin Coplan and Chelsie Greene. It truly feels like I have four little sisters and I will keep giving you advice as long as you keep coming to me for it!!

At Northwestern, I have had the pleasure of working with many of my peers and being shown firsthand how passionate and curious the students here are. I truly hope that my collaborations with Austin Evans, Nathan Flanders, Justin Hoffman, and many other dedicated classmates continue beyond these walls. Along those lines, I'd also like to acknowledge John Philbin (UC Berkeley) and Viktoriia Morad (ETH Zürich), both of whom I've had the pleasure of collaborating with on multiple projects. One of the best parts of my Ph.D. was working on side projects because I got to test and expand my knowledge, and I am incredibly grateful for the opportunities I got.

It is also absolutely necessary that I thank Prof. Mary Jane Shultz, my undergraduate research advisor, for having the most confidence in me I have ever come across. I am still not quite sure why you were so impressed with me, but I try to live up to that expectation whenever I can.

And finally… it is completely true when I say that none of this could have happened without Andrew Rosen. There is a quote out there that advises: “Choose the person who makes you better.” I very selfishly chose someone who not only makes me better, generally speaking, but more specifically someone who makes me a better scientist.

Dedication

Victor A. Brumberg

To my grandfather, whom I have always admired for his simultaneously whimsical and scholarly character

Table of Contents

List of Figures

List of Tables

1 Introduction to Semiconductor Nanoplatelets

Control over the synthesis of colloidal semiconductor nanocrystals (NCs) was developed in 1993 by Chris Murray, David Norris, and Moungi Bawendi.[1] The effect of quantum confinement, whereby an electron's wavefunction is modified by the presence of a potential barrier, had already been attributed to the optical properties displayed by semiconductor nanoparticles.[2,3] Scientists had identified that the walls of a nanoparticle could act as a potential barrier, such that altering the nanoparticle diameter would modify the extent of confinement. In this way, the optical band gap of a material – the difference in energy between the valence and conduction bands, or the lowest energy at which the material will absorb light – could be modified without any change in the particle composition. Now, the development of reliable colloidal synthesis would make them easier to work with, study, and incorporate into electronics.

Since this period of discovery, semiconductor nanoparticles – or "quantum dots," as they are also commonly termed – have been developed in a wide range of sizes, shapes, and compositions, and their utility in a number of applications has been demonstrated.[4–6] Just as

changing the size of the nanoparticle alters its bandgap, altering the shape likewise influences the electronic bandgap. In this regard, altering the number of quantum-confined dimensions is one of the most effective ways of tuning nanoparticle electronic structure, as whether a particle is quantum confined in one, two, or three dimensions will have drastic implications on its electronic structure. One- and two-dimensional nanoparticles are thus of immense interest in the research community; in this dissertation, I will focus on a specific subset of materials, aiming to understand how their dimensionality influences their photophysical properties.

1.1 Optical Properties of Semiconductor NPLs

Nanoplatelets (NPLs) are colloidal, two-dimensional semiconductor nanocrystals that are quantum confined in only one dimension—that of their thickness. They benefit from the same advantages as conventional semiconductor quantum dots, such as solution processability, bandgap tunability,[7] and strong light absorption,[8–10] but with the added benefits that arise from quantum confinement in one dimension.[11] The NPL bandgap is defined almost entirely by its thickness, which is atomically defined, owing to the fact that NPLs contain a discrete number of unit cells along their vertical dimension. As a result, NPLs feature exceptionally narrow emission linewidths that make them exceptional candidates for optoelectronic applications.[11–13] Indeed, NPLs feature such narrow emission linewidths that NPL ensembles have been shown to have the same emission linewidths as single NPLs, featuring only homogeneous broadening.[12] This is in contrast to the heterogeneous linewidths associated with zero-dimensional NCs, where even the most monodisperse samples will still feature inhomogeneous broadening.

To date, most of the work in the field of semiconductor NPLs has focused on CdSe and/or CdS. CdSe NPLs of 2.5 to 8.5* monolayers (ML) thickness have been synthesized,[11,14–21] allowing for bandgap tunability between 1.98 and 3.16 eV. By exchanging the ligands on the surface of the NPLs, growing a semiconductor shell or crown,[22–24] or compositional alloying,[25] further modification of the band energies are possible. Here, we focus on CdSe NPLs of 3.5, 4.5, and 5.5 ML (referred to in this work as 3, 4, and 5 ML NPLs), where the NPL surfaces are terminated by layers of Cd^{2+} and ligated with oleate, as these were the thicknesses that were first available to the scientific community. While the syntheses of 4 and 5 ML CdSe NPLs that were first introduced are analogous, the syntheses of thinner (2 ML) and thicker (6+ ML) NPLs require alternate methodologies like the use of halides,[14,15,20,21] or colloidal atomic layer deposition.[18,26,27] Other compositions of semiconductor NPLs aside from the II-IV semiconductors are now accessible as well, such as ZnX,[28] HgX,[29] PbX,[28,30–33] (X = S, Se, or Te) and the widely studied class of perovskite-based lead halides[34–36] like $CsPbBr_3$ NPLs.[37–39]

The absorption spectrum of CdSe NPLs is shown below in Figure 1.1a. Three distinct excitonic features can be observed, corresponding to the heavy-hole, light-hole, and split-off bands, which are related in Figure 1.1b for bulk zinc blende CdSe. Also depicted in Figure 1.1a is the photoluminescence spectrum of CdSe NPLs, which features a very small Stokes shift (<30 meV) in comparison to the typical Stokes shift of CdSe NCs (30–80 meV).[40] Like the narrow emission spectrum, the small Stokes shift of CdSe NPLs arises from the lack of inhomogeneity in NPL ensembles.

* Higher thicknesses are possible, but are hard to isolate (and thus will be present with thinner NPLs) or display very weak emission.

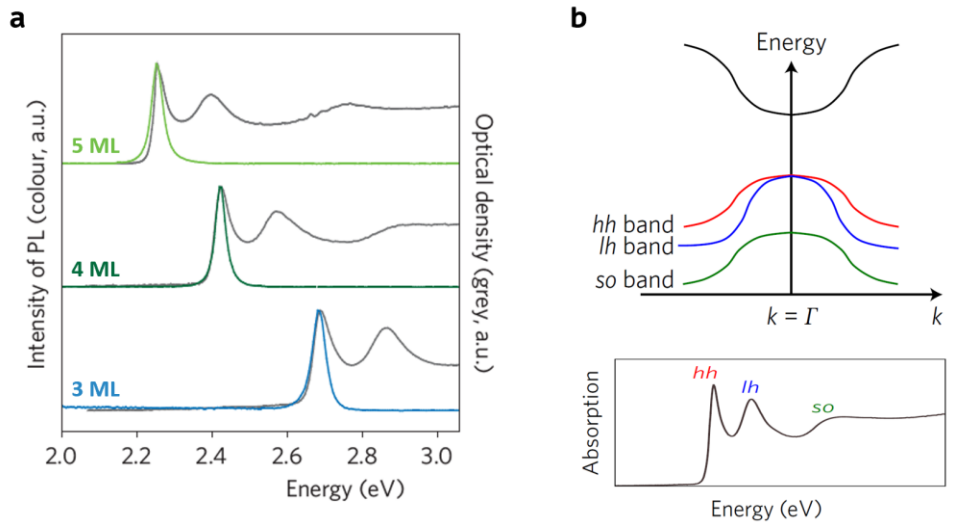

Figure 1.1. (a) Absorption and emission spectra of 3, 4, and 5 ML CdSe NPLs. Adapted from Ref. [11]. **(b)** Band diagram (energy vs. carrier momentum) of bulk zinc blende CdSe showing the conduction band and the heavy-hole, light-hole, and split-off bands of the valence band. The lower panel indicates the corresponding NPL absorption spectrum features derived from quantum confinement of the bulk valence band. Adapted from Ref. 41.

Notably, CdSe NPLs feature large absorption cross-sections that are an order of magnitude greater than those of zero-dimensional NCs and that can be further tailored via NPL thickness and lateral area.[8–10] It thus becomes natural to think about employing NPLs as light absorbers and then transferring either the excitations or the carriers into neighboring, electronically-coupled materials that can perform alternate functions.[42,43] In this regard, CdSe NPLs have been shown to be promising, as they exhibit highly efficient rates of Förster resonance energy transfer amongst one another[44–46]—even outpacing rates of nonradiative biexciton recombination, such that energy transfer can occur at high excitation fluences before the electron-hole pair has undergone recombination.[44,47] This energy transfer occurs even between NPLs of uniform thickness,

quenching the photoluminescence quantum yield in environments with a high proportion of stacked NPLs.[48,49]

1.2 Photophysical Properties

The photophysical properties of CdSe NPLs – namely, the carrier dynamics and behavioral response following photoexcitation – are important to understand if the aforementioned optoelectronic properties are to be harnessed and optimized for use in applications. The aim of this thesis and many other studies published in the field of NC carrier dynamics is thus to understand the processes that take place following NPL photoexcitation.

In most cases, excitation is executed using above bandgap energy photons, such that electrons are excited into above-band-edge conduction band states. Hot carrier (intraband) relaxation from these higher states to the conduction band edge takes place within 2 ps.[50] The fast lifetime of intraband relaxation represents a significant loss of energy, since the energy that is released during the process is unable to be harnessed for other applications. Instead, the energy is simply dispersed throughout the lattice as heat; more specifically, intraband relaxation happens via phonon generation, or lattice vibrations. If higher excitation densities are used, for example in the case of photoelectrical injection for light-emitting diodes or for establishing a population inversion for lasing, cooling takes longer. At these higher excitation densities, cooling requires tens of picoseconds as hot electrons cool via emission of longitudinal optical (LO) phonons, which are subsequently reabsorbed by the carriers before they can decay.[51] These two populations reach a

thermal equilibrium that then decays together through interaction with acoustic phonons, which ultimately defines the longer carrier cooling lifetime.[51]

As shown in Figure 1.2, following intraband relaxation, carriers reside at the band edge. In the case of low excitation fluence, single excitation recombination will proceed, the lifetime of which is on the order of a few nanoseconds for CdSe NPLs.[11,52] While CdSe NCs typically display luminescence that decays with a lifetime on the order of tens of nanoseconds,[53] the photoluminescence quantum yield of CdSe NPLs is typically lower than that of CdSe NCs, owing to poorer surface passivation. Poor surface passivation can result in the creation of inter-bandgap trap states that electrons and/or holes can occupy, thereby hindering recombination. Nevertheless, quantum yields are still respectable at around 20-50%.[40] As shown in the bottom panel of Figure 1.2, at higher excitation densities, multiple excitons will be generated. An appreciable advantage of CdSe NPLs lies in their biexciton dynamics, where nonradiative Auger recombination is observed to occur on the order of hundreds of picoseconds,[54,55] in comparison to the single picosecond lifetimes of CdSe NCs.[56,57] This enables higher efficiencies in light-emitting diodes and higher gain in lasing,[58,59] pairing well with the narrow emission linewidths of NPLs for prospective applications.

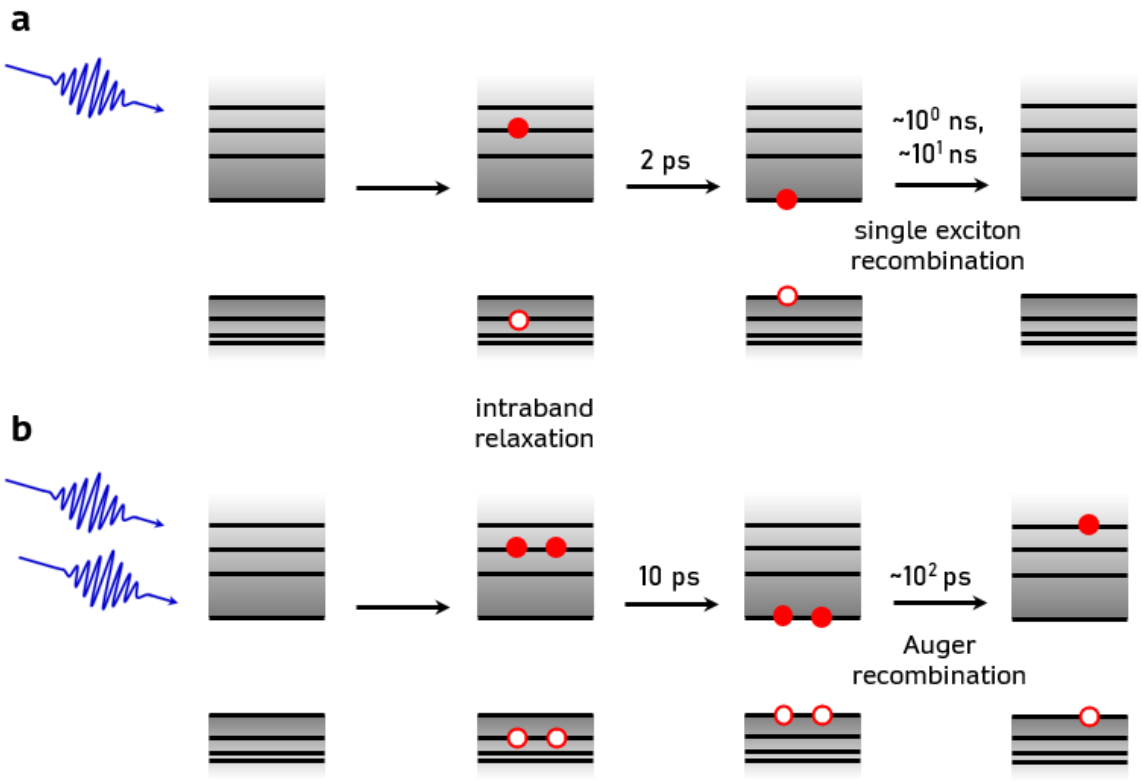

Figure 1.2. Relaxation processes following **(a)** low and **(b)** high fluence, above bandgap excitation. Above bandgap excitation creates hot carriers that undergo intraband relaxation down to the conduction and valence band edges. For a single exciton, recombination can occur radiatively or nonradiatively. For a biexciton, recombination tends to occur nonradiatively through Auger recombination.

1.3 Active Challenges in NPL Photophysics

While there are many aspects of NPL photophysics that are already understood, there remain equally as many – if not more – that remain open as active challenges. The complications that arise as a result of strong quantum confinement in one dimension and a lack thereof in the other two create scenarios where carrier dynamics are difficult to predict *a priori* or challenging to comprehend once they have been probed. When they exist, results on other two-dimensional

systems such as quantum wells or transition metal dichalcogenides are not blindly transferrable, necessitating the need for experiments specific to these colloidal materials. In this dissertation, I apply time-resolved methods such as transient absorption spectroscopy, time-resolved photoluminescence spectroscopy, magneto-optical spectroscopy, and time-resolved X-ray diffraction to better understand multiple aspects of the photophysics of CdSe NPLs.

In particular, I begin by examining the in-plane spatial extent of the exciton radius. Given the lack of quantum confinement in the lateral plane of the NPL, there is reason to believe that the exciton would be spatially extended throughout the plane of the NPL—or, at least, as spatially extended in-plane as it would be in bulk CdSe. Theoretical arguments have not agreed upon a size, and experimental estimates based on binding energy are inconsistent, so in Chapter 3 we apply a more direct method of measuring the in-plane exciton radius using magneto-optical spectroscopy to determine whether or not the exciton is spatially confined within the plane of the NPL.

The spatial extent of the exciton influences NPL electronic interactions with other materials, which brings us to Chapter 4, where I investigate the effect of nanoparticle dimensionality on rates of charge transfer between $CsPbBr_3$ and CdSe nanoparticles. By keeping all other variables the same—namely, interparticle separation and electron transfer driving force—and only varying the nanoparticle dimensionality—we are able to compare rates of electron transfer for 0D → 0D, 0D → 2D, 2D → 0D, and 2D → 2D nanoparticle combinations. We find that systems containing 2D NPLs as the electron acceptor exhibit faster rates of electron transfer than systems containing 0D quantum dot acceptors, establishing that NC dimensionality plays a role in rates of electron transfer.

In Chapter 5, we move past single electron-hole pairs, to considering NPLs that hold multiple excitations and consider the process of Auger recombination, in which an excited electron-hole decays nonradiatively by transferring its energy to a third carrier. As mentioned above, this process is one of the many benefits of NPLs, as rates of Auger recombination for NPLs are an order of magnitude slower than they are for zero-dimensional NCs. Nevertheless, we have very little understanding of the behavior of how these rates scale with respect to parameters such as NPL lateral area, volume, and temperature, and we investigate these aspects in Chapter 5.

Another aspect worth considering when working with NPLs at high excitation fluences is what the effect of such high excitation fluences is on the NPL structure and, therefore, optoelectronic properties. As introduced previously, above bandgap excitation is followed by intraband relaxation, whereby hot electrons relax to the band-edge via the generation of phonons. These phonons heat the NC lattice. Given the low thermodynamic stability of high surface area NCs, does this lattice heating negatively influence the NC structure? Since NC optoelectronic properties are so closely tied to their structures, this is a critical question to answer, and one that I describe in Chapter 6 for an anisotropic material featuring high surface energy corners and edges that are likely to impact their physics of melting.

1.4 Appendix – Synthesis of CdSe NPLs

Below, the synthesis of 3, 4, and 5 ML CdSe NPLs is provided for reference, as these methods are common to all the chapters in the thesis. The syntheses is adapted from the initial work of Ithurria

et al.,[11] with additional modifications developed by Igor Fedin and Benjamin Diroll to achieve better thickness control and also enable manipulation of lateral area.[58,60]

Prior to the synthesis of 4 or 5 ML CdSe NPLs, cadmium myristate precursor is prepared by dissolving cadmium nitrate (650 mg) in methanol (20 mL) and then adding it to a solution of sodium myristate (1.5 g) also dissolved in methanol (100–125 mL). The resulting powder is isolated via centrifugation and then washed three times with methanol and once with acetone, and then dried overnight in a vacuum oven.

1.4.1 Synthesis of 3 ML NPLs

Cadmium acetate (960 mg), oleic acid (600 μL), and octadecene (60 mL) are added to a three-neck flask and degassed for 1 hour at 80 °C. The solution is then heated to 180 °C under nitrogen, at which point selenium powder dissolved in trioctylphosphine (600 μL, 1 M) is rapidly injected. After 5 minutes, the reaction is stopped and the NPLs are washed twice with isopropanol and then redispersed in 1-methylcyclohexane.

1.4.2 Synthesis of 4 ML NPLs

Cadmium myristate (170 mg), selenium powder (12 mg), and octadecene (14 mL) are added to a three-neck flask and degassed for 1 hour under stirring. The solution is then heated under nitrogen; at 190 °C, cadmium acetate (40 mg) is added. Heating is continued until 240 °C, which is maintained for 5 minutes before cooling the reaction back down. When the temperature reaches 70 °C during cooling, oleic acid (2 mL) and hexane (15 mL) are added. The solution is then centrifuged and the resulting pellet is dissolved in 1-methylcyclohexane and filtered through a 0.2 μm polytetrafluoroethylene (PTFE) syringe filter.

To achieve small lateral area platelets, the solution is only heated to 225 °C prior to cooling. To achieve medium or large plates, the solution is heated to and then held at 240 °C for 1 minute (medium plates) or 5 minutes (large plates) and then cooled.

1.4.3 Synthesis of 5 ML NPLs

Cadmium myristate (170 mg) and octadecene (14 mL) are added to a three-neck flask and degassed for 30 minutes. The solution is then heated under nitrogen to 250 °C. At 250 °C, selenium powder (12 mg) sonicated in octadecene (1 mL) is rapidly injected. After 60 seconds, cadmium acetate (90 mg) is added. The solution is held at 250 °C for 10 minutes and then cooled. When the temperature reaches 70 °C, oleic acid (2 mL) and hexane (15 mL) are added. The solution is then centrifuged and the resulting pellet is dissolved in 1-methylcyclohexane and filtered through a 0.2 μm PTFE syringe filter.

2 Time-Resolved Methods

Throughout the studies presented in this thesis, two types of time-resolved spectroscopies are frequently employed to gain insight into the photophysical properties of semiconductor nanocrystals: transient absorption spectroscopy and time-resolved photoluminescence spectroscopy. In addition, Chapter 6 focuses on a time-resolved diffraction technique that provides time-resolved structural information that is highly complementary to the types of ultrafast electronic studies commonly conducted to gain insight into nanomaterial dynamics. In this chapter, the basics of each technique are explained and some general details regarding data processing are provided that are inherent to the overall techniques, rather than specific to the individual works presented in the following chapters.

2.1 Pump-Probe Methods

Transient absorption (TA) spectroscopy (Section 2.2) and time-resolved X-ray diffraction (TR-XRD, Section 2.4) are both pump-probe methods wherein the sample is first excited using an optical “pump” pulse and then probed to obtain information about the sample in its excited state.

In the case of semiconductor nanoparticles, excitation moves an electron from the valence band (ground state) into the conduction band (excited state). Following this excitation, the sample is characterized in its excited state via a probe pulse. The probe determines the type of information that will be determined. Common types of pump-probe methods employ optical, electronic, magnetic, or X-ray probes. Even within the class of optical pump, optical probe spectroscopy, the amount of information that can be obtained varies greatly depending on the wavelength of probe that is chosen and whether it lies in the ultraviolet (UV), visible, near-infrared (near-IR), or IR region. In this thesis, I employ pump-probe spectroscopy using an optical probe in the visible wavelength range (TA, Section 2.2; see also Chapters 4 and 5) as well as an X-ray diffraction probe (TR-XRD, Section 2.4; see also Chapter 6). While TA provides information about electronic structure following excitation, owing to the use of the optical probe, TR-XRD provides structural information, owing to the use of an X-ray diffraction probe. Short pulse widths are critical to obtaining high time resolution information; as later described, the optical pump used for TA has a 35 fs pulse width, affording sub-picosecond time resolution that is narrow enough to resolve all of the electronic processes described in Chapter 1.

The probe permits characterization of the sample at a variety of fixed time delays following photoexcitation. In this way, the response of the sample following photoexcitation can be monitored as a function of time and the lifetimes of the processes discussed in Chapter 1, Section 1.2 can be determined. A time delay between the pump and the probe can be established according to varying path lengths along an optical table; since light travels at a speed of 3×10^8 m/s, establishing a time delay of 1 ps between the pump and the probe simply requires having the probe

travel 0.3 mm further than the pump. The distance the probe (or the pump) has to travel can be adjusted throughout the experiment using a delay track (see Figure 2.2).

Although the sample is being photoexcited by the pump, not all of the sample will undergo excitation and produce a detectable response in response to photoexcitation. This is because of two reasons. Firstly, the pump typically does not irradiate the full sample region, typically as a matter of concentrating the photons over a small area to generate the desired fluence (i.e. power density). Second, even within the irradiated area, the sample will not absorb every photon; materials have *absorption cross-sections* that dictate how many photons will actually be absorbed. As such, regardless of the actual incident radiation, only a fraction of the sample will enter an excited state and produce a detectable response. The information that the probe collects at this point will thus contain contributions from both ground state and excited state populations. To isolate the contribution from the excited state population, pump-probe spectra are typically evaluated as a difference:

$$\Delta I = I_{\text{pump on}} - I_{\text{pump off}} \tag{2.1}$$

where the ground state spectrum (acquired with no photoexcitation, or by having the "pump off") is differenced from the excited state spectrum (acquired by having the "pump on"). The ground state spectrum is continuously recollected throughout the experiment, rather than just being measured once, in order to account for potential instrumental instability or sample evolution through the experiment. As such, one alternates collecting ground state and excited state spectra by using a chopper to alternate sending the pump through to the sample at half the frequency of the probe, in addition to performing and then averaging multiple scans of the sample in the laboratory time frame.

2.2 Transient Absorption Spectroscopy

In its most basic configuration, absorption spectroscopy provides information about the electronic transitions within a material. White light is passed through the sample, and based on how much of that light is absorbed by the sample, and at what wavelengths, we are able to discern information about resonant transitions that suggest the electronic structure of the material.

TA spectroscopy is a time-resolved technique that compares the excited-state absorption spectrum of a material to its ground state absorption spectrum according to Equation 2.1 for absorption: $\Delta A = A_{\text{pump on}} - A_{\text{pump off}}$. Following photoexcitation, the absorption spectrum of the nanoparticle sample is distinct from that of the ground state owing to the presence of an electron(s) in the conduction band. For a direct gap semiconductor such as CdSe, the intensity of the transition from the valence band to the conduction band in the nanoparticle absorption spectrum becomes weaker in the excited state in comparison to the unexcited state (i.e. *bleached*), as there is already one electron occupying the conduction band state. Since the TA spectrum is plotted as a difference between the excited and ground state spectra in order to hone in on the electron changes induced by photoexcitation, a bleached transition appears as a negative ΔA signal. The static and transient absorption spectra for CdSe NPLs are plotted in Figure 2.1; the blue arrows at 550 and 520 nm indicate the location of two bleaches that arise owing to the presence of the electron in the conduction band following photoexcitation.

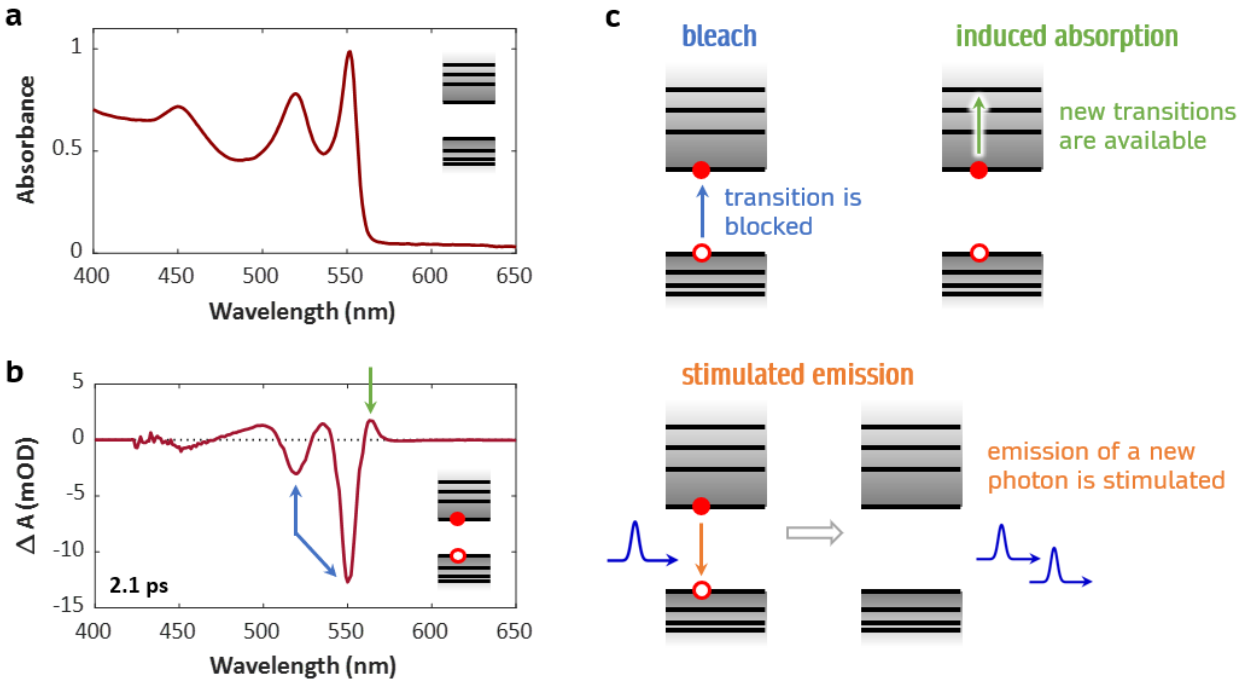

Figure 2.1. (a) Visible absorption spectrum of CdSe NPLs in the ground state. **(b)** Transient absorption spectrum, 2.1 ps after photoexcitation, of CdSe NPLs in the excited state. Bleach and induced absorption features can be seen and are indicated by the blue and green arrows, respectively. **(c)** Schematics indicating how bleach, induced absorption, and stimulated emission features can arise in TA spectroscopy.

On the other hand, the occupancy of this conduction band state by this electron opens up the possibility of accessing other transitions within the higher states of the conduction band that were not previously accessible for the ground state material. As a result, at some energies we observe increased absorption, or *induced absorption*, that manifests as a positive ΔA signal. Lastly, the presence of a conduction band electron allows for the possibility of *stimulated emission*, in which interaction with a bandgap-energy photon causes emission of two bandgap-energy photons. Since this process causes the probe beam to emerge from the sample with increased intensity at this photon energy, it also results in a negative ΔA signal at the wavelength of the bandgap. Figure 2.1c summarizes these three common TA features.

In each instance that TA is mentioned in this dissertation, TA was conducted using a 35 fs pulse width, amplified Ti:sapphire laser operating at 2 kHz. A 400 nm pump pulse was produced by frequency-doubling the 800 nm fundamental output of the Ti:sapphire laser in a β-barium borate (BBO) crystal, and was reduced to 1 kHz upon directing it through a synchronized mechanical chopper. The probe was a visible white light source produced by focusing the 800 nm output of the same Ti:sapphire laser into a sapphire plate. Probe spectra were recorded after passing through the sample by dispersing the light onto a grating and then detecting the intensity at each wavelength on a single shot basis using a complementary metal-oxide-semiconductor (MOS) sensor.

The most basic analysis of TA data involves analyzing the dynamics/kinetics at one particular probe wavelength of interest—for example, that of a bleach or induced absorption feature. This can be effective when the goal is to observe the dynamics of an electronic process, as one can simply monitor the arrival or departure of carriers into the electronic state involved in the electronic process of interest (i.e. charge or energy transfer) by analyzing the growth or decay of the bleach or induced absorption associated with that electronic state. This technique is demonstrated in Chapter 4, in which the bleach of CdSe NPLs is monitored as an indicator for the transfer of electrons from $CsPbBr_3$ nanoparticles to CdSe. In cases where a simple wavelength analysis is not sufficient, more advanced methods of analysis such as singular value decomposition or global target analysis can be used to analyze time-resolved spectral data.[61,62]

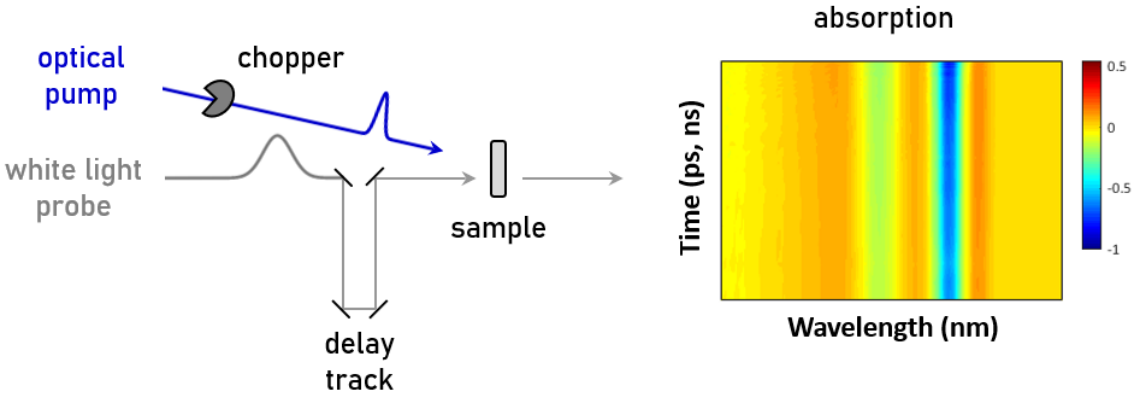

Figure 2.2. Schematic of transient absorption (TA) spectroscopy. In TA, an optical pump photoexcites the sample, exciting an electron from the valence band to the conduction band. After a fixed time delay, which is mechanically generated by a delay stage, a white light probes the sample, acquiring an absorption spectrum of the sample in its excited state. The ground state absorption spectrum is then differenced from this excited state absorption spectrum to generate the transient absorption spectrum, which can reveal features such as bleaches and induced absorptions.

2.3 Time-Resolved Photoluminescence Spectroscopy

Complementary to TA is time-resolved photoluminescence spectroscopy, another type of spectroscopy that provides optical (and therefore electronic) information about a sample. In time-resolved photoluminescence spectroscopy, the emission of a nanoparticle ensemble is collected as a function of time following pulsed optical excitation, allowing one to obtain dynamics regarding emission dynamics and spectral profile as a function of time.

One way this can be executed is using time-correlated single photon counting (TCSPC), in which an avalanche photodiode is used to detect single photons as they arrive at various time delays with respect to the time at which photoexcitation occurred. In this case, only photons of one

specified wavelength are detected; this is typically selected to be the peak emission wavelength of the sample.

In this thesis, time-resolved photoluminescence data was typically collected using a streak camera, where emission is collected not only as a function of time, but also as a function of wavelength. In a streak camera, photons are first resolved by a grating as in a typical spectrometer, such that a range of photon energies (wavelengths) can be detected. These photons are then sent to a linear strip photocathode where they are converted into electrons; the conversion of incident photons to electrons allows for the photoluminescence to be displaced as a function of time via the application of a time-dependent voltage through which the electrons travel. Electrons are then amplified using a microchannel plate, impacted into a phosphor screen, and detected via a charge-coupled detector (CCD).

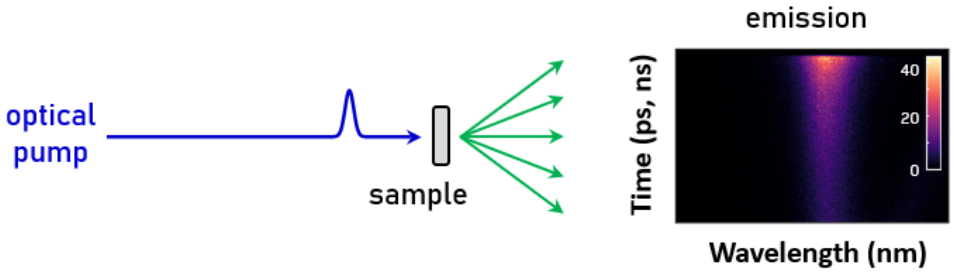

Figure 2.3. In time-resolved photoluminescence, an pulsed laser source photoexcites the sample. Emission is collected on a streak camera in order to resolve photons as both a function of time and wavelength.

An example of the two-dimensional data that results from streak camera data collection is shown in Figure 2.3. Data is typically analyzed by integrating the data either as a function of time, to produce a time-resolved spectrum, or as a function of wavelength, to produce spectrally-resolved dynamics that reflect emission from a given electronic state(s) in the sample. As in TA,

information about electronic processes can be gleaned by tracking the dynamics of the wavelength regions corresponding to states that necessarily relate recombination of an electron and hole to produce the detected photons.

2.4 Time-Resolved X-Ray Diffraction

Time-resolved X-ray diffraction (TR-XRD) provides structural characterization of materials following photoexcitation. As shown in Figure 2.4, in TR-XRD, the sample is pumped using an optical excitation wavelength of choice – typically 400 nm – and then probed using monochromated synchrotron X-ray pulses to obtain diffraction from the sample. As is typical in pump-probe methods, diffraction from the sample before and after photoexcitation is differenced to obtain a transient X-ray diffraction pattern. That is, $\Delta S = S_{\text{pump on}} - S_{\text{pump off}}$, as per Equation 2.1 for the specific case of diffraction scattering. The time delay between the optical pump and X-ray probe can be varied to obtain dynamics describing the structural response of the nanoparticle ensemble, while the fluence of the optical pump can be altered to obtain information regarding its fluence dependence. Diffraction is collected on a Pilatus 2M detector and then azimuthally integrated to obtain 1D powder X-ray diffraction patterns as a function of q.

The use of a synchrotron X-ray source is particularly important, as diffraction from nanocrystalline samples presents multiple challenges. First and foremost, the number of crystalline planes present in a nanocrystal is quite obviously significantly lower than the number that are present in a bulk material. A natural result of this reduced number of crystalline planes is that the Bragg diffraction from the sample is broadened. The Scherrer equation captures this effects via the relationship

$$\tau = \frac{K\lambda}{\beta \cos\theta} \tag{2.2}$$

where τ is the average size of the nanoparticles in the ensemble, K is a constant that is typically taken to be 0.9, λ is the X-ray wavelength, β is the full-width at half-maximum of the peak being analyzed (after instrumental line broadening has been accounted for), and θ is the Bragg angle.[63] By analyzing a series of peaks in the nanoparticle diffraction pattern, an estimate for the nanoparticle size that is comparable in accuracy to that from transmission electron microscopy (TEM) can be obtained.[64,65] Though diffraction intensity can be improved by using high quantities of monodisperse material, Scherrer broadening is a notorious issue for nanoparticle diffraction studies, and higher energy X-ray sources are thus of critical importance. Broadening of diffraction peaks can also arise from surface reconstruction, which can impact a large number of atoms, such that the lattice is not perfectly crystalline throughout the nanoparticle.[66] In addition to peak broadening, this can result in diffraction peak shifts owing to different values for lattice plane separations in comparison to the bulk composition.

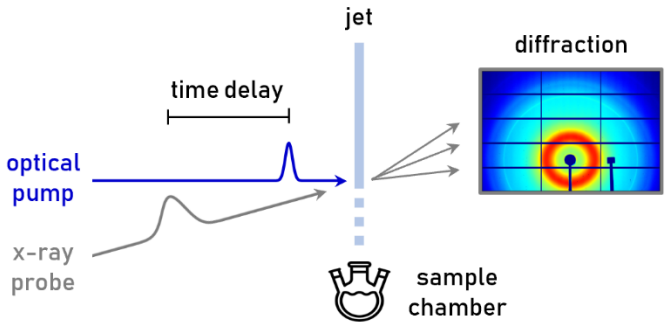

Figure 2.4. Experimental configuration of time-resolved X-ray diffraction. An optical pump photoexcites the sample, followed after some time delay by an X-ray probe that characterizes the sample via X-ray diffraction. Here, the sample is shown circulating as a colloidal liquid jet, however samples can also be examined as films.

Some types of common structural responses and their characteristic transient lineshapes are shown in Figure 2.5. In TR-XRD experiments where above band-gap photoexcitation is used, as is the standard for the experiments performed by our group thusfar and the experiment discussed in Chapter 6, the excess energy deposited into the nanocrystal as a result of the above bandgap excitation is converted into heat. Multiple electron-hole pairs can also rapidly annihilate to produce heat as well. As a result, lattice expansion is often observed,[67–71] although in principle investigation of a negative thermal expansion coefficient material would introduce an exception to that behavior. Increased diffraction at lower q values, owing to increased lattice spacings in real space, along with decreased diffraction at higher q values, results in the derivative-like lineshape presented in Figure 2.5a. As the amount of heat deposited into the NC becomes greater, other structural effects can be observed. Phase transitions can in some cases be identified via the loss or appearance of new diffraction peaks as one crystal phase converts into the other (see Figure 2.5a).[68] Additionally, structural degradation in the form of decomposition or melting manifests as loss of diffraction, or negative transient diffraction peaks (see Figure 2.5b).[67,69,70]

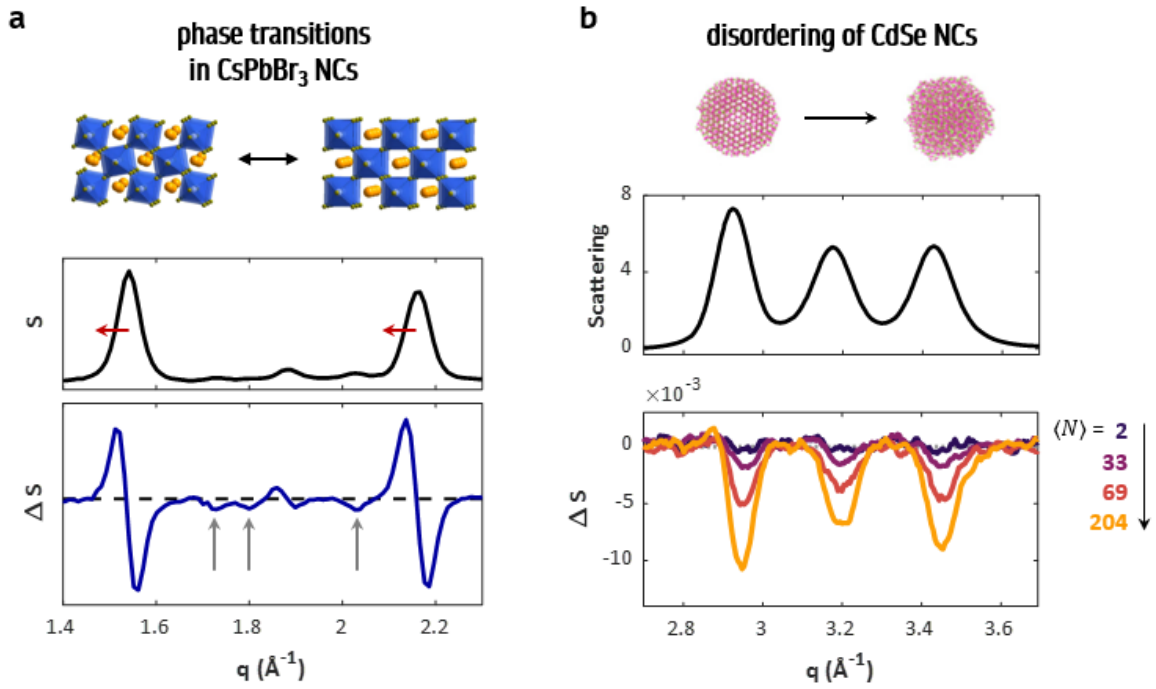

Figure 2.5. Examples of transient structural responses observed using TR-XRD. **(a)** Orthorhombic to cubic phase transition in $CsPbBr_3$ NCs, as reported in Ref. 68. The bottom panel shows a loss of the orthorhombic diffraction peaks, as indicated by the gray arrows. Note also the derivative-like lineshapes observed near $q = 1.5$ and 2.15 that arise from lattice expansion. **(b)** Disordering in CdSe NCs, as reported in Ref. 67. The bottom panel shows how disordering increases as a function of excitation fluence, or $\langle \boldsymbol{N} \rangle$, the average number of excitons per particle.

3 In-Plane Exciton Extent in CdSe Nanoplatelets

3.1 Introduction

Semiconductor nanoplatelets (NPLs) present thicknesses that are smaller than the bulk excitonic Bohr radius, and yet they are quasi-infinite in lateral extent. Given the strong, thickness-defined quantum confinement, NPLs constitute colloidal analogues of epitaxially grown quantum wells. In the case of zinc blende CdSe, NPLs with three to eight monolayers (MLs) measuring roughly 0.3 nm per ML can be synthesized with negligible ensemble thickness dispersity[11,12,14,15] as well as lengths and widths of tens of nanometers.[11,58,72,73] Given the 5.4 nm bulk CdSe Bohr radius, this scenario might suggest pancake-like, nearly two-dimensional excitons with a large value for the in-plane exciton radius, $r_{\text{plane}} \approx r_l \approx r_w$. On the other hand, interplay between confinement energy and electron-hole Coulomb attraction may yield a small and relatively spherical exciton with $r_h \approx r_l \approx r_w$. Given the synthetic control over thickness and, to a lesser degree, lateral extent of the two-dimensional morphology,[11,35,37,38,74–76] CdSe NPLs present an ideal material for examination of this fundamental question.

This chapter is adapted from:

Brumberg, A.; Harvey, S. M.; Philbin, J. P.; Diroll, B. T.; Lee, B.; Crooker, S. A.; Wasielewski, M. R.; Rabani, E.; Schaller, R. D. Determination of the In-Plane Exciton Radius in 2D CdSe Nanoplatelets *via* Magneto-Optical Spectroscopy. *ACS Nano* **2019**, *13* (8), 8589–8596.

Since the first detailed report of CdSe NPLs,[11] the topic of excitons in CdSe NPLs has been treated theoretically,[9,77–79] but with only one explicit calculation of exciton size.[80] As in Ref. [80], estimated regarding exciton size can be developed based on the exciton binding energy,[81] but discrepancies in reports of this energy exist, with experimental and theoretical papers conveying values ranging from about 100 meV to greater than 400 meV.[9,77,80,82] Derived values also depend upon whether the structures are treated using 3D or 2D Coulomb potentials. Whereas it is apparent that the change in dimensionality from three-dimensional bulk material to quasi-two-dimensional NPLs increases the exciton binding energy through reduced dielectric screening, as is the case with monolayer transition metal dichalcogenides,[83,84] it is not clear to what degree this alters the lateral exciton extent.

Treatments of excitons in conventional quantum wells offer a starting point for determining the lateral size of the exciton in NPLs. Calculations of exciton binding energies in GaAs and $GaAs/Ga_{1-x}Al_xAs$ quantum wells yield values on the order of tens of meV.[85,86] Given such small binding energies, excitons in quantum wells can be expected to have a large in-plane lateral extent. On the other hand, work by Miller notes that the exciton in a quantum well may be compressed not just vertically, due to potential changes at the quantum well faces, but also laterally, so as to minimize orbital kinetic energy.[87,88] However, results from quantum wells cannot necessarily be extrapolated to NPLs, given the finite lateral sizes of NPLs and their interactions with lower dielectric constant ligands, in comparison to semiconductor templating substrates.

Studies on two-dimensional transition metal dichalcogenides provide an additional comparison of relevance. Work probing monolayer WS_2 and WSe_2 suggests that the exciton lateral extent is between 1 and 2 nm,[89–92] consistent with large binding energies on the order of 200-500

meV.[83,84,93] These results suggest that the exciton in colloidal, quasi-two-dimensional NPLs may also be small; however, the potentially smaller binding energy in CdSe NPLs – which arises due to a smaller electron and hole mass and multilayer thickness – could engender a more spatially extended exciton.

Exciton size can be accessed via magneto-optical measurements. In a magnetic field, the energy of the exciton is modified and can be expressed as

$$E_{\pm}(B) = E_0 \pm \frac{1}{2} g_{\text{ex}} \mu_B B + \sigma B^2 + \cdots \tag{3.1}$$

where E_0 is the unperturbed exciton energy, g_{ex} is the excitonic g-factor, μ_B is the Bohr magneton, and σ is the diamagnetic shift coefficient. The application of a magnetic field both induces a linear Zeeman splitting that lifts the degeneracy of the exciton angular momentum states and introduces a diamagnetic shift term, which grows quadratically with the field. In magnetic fields where the cyclotron energy $\hbar eB/\mu_r$ is significantly smaller than the exciton binding energy, the diamagnetic shift coefficient is equivalent to

$$\sigma = \frac{e^2}{8\mu_{r,\text{plane}}} \langle r^2 \rangle \tag{3.2}$$

where e is the elementary charge, $\mu_{r,\text{plane}}$ is the in-plane exciton reduced mass, and r is a radial coordinate in the direction perpendicular to the field.[94,95] Thus, $\langle r^2 \rangle$ is the expectation value of $x^2 + y^2$ with respect to the exciton wave function. When NPLs are oriented perpendicular to the direction of the applied magnetic field, $\langle r^2 \rangle$ provides a measure of the in-plane exciton radius. Note that the root-mean-square exciton radius, $r_{\text{rms}} = \sqrt{\langle r^2 \rangle}$, is not the same as the often-used

Bohr radius, a_B; in bulk semiconductors, $r_{\text{rms}} = \sqrt{2}a_B$. With diamagnetic shift coefficients on the order of 1 μeV/T^2, even 60 T magnetic fields only provide energy shifts of a few meV. As indicated in Table 1, the cyclotron energy (tens of meV) at these high fields remains an order of magnitude less than the (100 meV or greater) exciton binding energy in CdSe NPLs, such that the in-plane exciton radius can be calculated via a diamagnetic shift. Previously, this approach has been implemented to experimentally probe exciton radii in two-dimensional materials such as monolayer transitional metal dichalcogenides and quantum wells.[89–91,94,96–98]

Table 3.1. Reduced masses, cyclotron energies, and binding energies of the heavy-hole excitons in 3, 4, and 5 ML CdSe NPLs. Reduced masses are taken from Ref. 77.

Sample	Reduced Mass (m_0)	Cyclotron Energy at 60 T (meV)	Binding Energy (meV)
3 ML	0.21	33	~ 210
4 ML	0.17	41	~ 190
5 ML	0.14	49	~ 170

Determination of the in-plane exciton radius, r_{plane}, requires orientation of NPLs such that their lateral areas are perpendicular to the direction of the applied magnetic field. Orientation of CdSe NPLs has previously been attempted by incorporating NPLs into polymer films with subsequent stretching[99,100] or by manipulating solvent interfaces upon NPL monolayer deposition.[101–103] For optical measurements in magnetic fields, the former option presents advantages with regard to the optical density required for absorption measurements.

In this work, CdSe NPLs were first oriented by biaxially stretching polymer films and probed using small-angle X-ray scattering (SAXS), which determined that sufficient in-plane orientation was successfully achieved. Optical absorption spectra of both unstretched and stretched

films were then measured versus magnetic field strength at low temperature to calculate diamagnetic shift coefficients, covering three different NPL thicknesses and lateral areas. The observed diamagnetic shifts are small and support a picture of tightly bound excitons with small lateral extent. Atomistic calculations, conducted by using a semi-empirical pseudopotential method[104,105] and solving of the Bethe-Salpeter equation[106] that accounts for electron-hole interactions, are consistent with the experimental findings.

3.2 Methods

3.2.1 Nanoplatelet Synthesis

For a description of CdSe NPL synthesis, see Chapter 1, Section 1.4.

3.2.2 Preparation of Polymer Films

A 5 wt% solution of poly(butyl methacrylate-*co*-isobutyl methacrylate in chloroform was prepared by dissolving the polymer (460 mg) in chloroform (10 mL). The desired amount of CdSe NPLs was dried in a small vial, redispersed in 400-450 μL of the polymer solution, and then agitated using a Vortex mixer to ensure full dispersion of the NPLs. The entire quantity of solution was then deposited on a 22 mm × 22 mm glass coverslip and allowed to dry.

Prior to stretching, polymer films were removed from glass substrates using a razor blade. Binder clips were attached to two opposing ends of the films on top of 2 cm × 5 mm glass pieces wrapped in Teflon tape to evenly distribute force along the edges of the film. Films were then placed in a hot water bath and heated to above the glass transition temperature of the polymer (35 °C) before stretching along the first axis. After stretching along this first axis and then being

allowed to cool back down to room temperature, an additional set of binder clips were added to the remaining two sides. The film was then once again placed in the bath, and once warmed, stretched along the second axis while maintaining force along the first. The film was allowed to cool completely to room temperature before the clips were removed. Films were typically stretched to 200% along the first axis and to just less than 200% along the second axis.

3.2.3 Small Angle X-Ray Scattering

Small angle X-ray scattering (SAXS) was conducted using Beamline 12-ID-B at the Advanced Photon Source (Argonne National Laboratory) using 13.3 keV X-rays. The scattered radiation was detected using a Pilatus detector positioned approximately 2 m away from the sample. A silver behenate sample was used as a standard for q calibration.

3.2.4 Absorption Measurements vs. Magnetic Field

Absorption measurements in high magnetic fields were acquired on stretched polymer films at 4 K using a 65 T pulsed magnet located at the National High Magnetic Field Laboratory in Los Alamos, NM. An optical fiber was used to deliver white light from a xenon lamp through a thin-film circular polarizer and the sample. The transmitted light was reflected back into a collection fiber and into a 300 mm spectrometer with a charged-coupled device (CCD) detector, which was synchronized to the magnetic field pulse.

The use of circularly polarized light facilitates probing of the different heavy-hole exciton angular momentum states, as optical selection rules dictate that $\Delta m = +1$ for left circularly polarized light (σ^-) and $\Delta m = -1$ for right circularly polarized light (σ^+). Pulsing the magnetic field in both the positive (to +60 T) and negative (to -60 T) directions permits access to each polarization state with a fixed polarizer, as these are equivalent by time-reversal symmetry.

3.3 Data Processing

Transmission spectra were collected as a function of magnetic field in wavelength space. These spectra were then converted to energy space according to

$$E = \frac{hc}{\lambda} \tag{3.3}$$

$$f(E) = -f(\lambda)\frac{hc}{E^2} \tag{3.4}$$

where $f(\lambda)$ and $f(E)$ are the intensities at a given wavelength λ or energy E.

Figure 3.1 highlights the entire fitting procedure for extracting the peak shifts of the heavy-hole exciton peak. Figure 3.1a shows raw transmission spectra at 0 T, 26.2 T, and 58.9 T. For analysis, the data was truncated at some energy between the heavy-hole and light-hole peaks so that the only peak in the spectrum was that of the heavy-hole. The data was then normalized at an energy lower than that of the peak, as indicated in Figure 3.1b by the star. Two points on either side of the normalization point were selected as the two points needed to define the baseline, which is also shown in Figure 3.1b. The result of baseline subtraction is shown in Figure 3.1c; baseline subtraction helped fix the peak asymmetry brought upon by the fiber background, although the resulting peak was still slightly asymmetric. To counteract this, only the tip of the peak—which was mostly symmetrical—was fit, as shown in Figure 3.1d. Only the points below some signal threshold (in the case of these 4 ML NPLs, -0.53) were considered. The signal threshold was selected by running the analysis at a range of signal thresholds and then selecting the value that gave the smallest error for the diamagnetic shift. Each set of points was then fit to a Gaussian using the MATLAB (version R2016b) '`gauss1`' fit function.

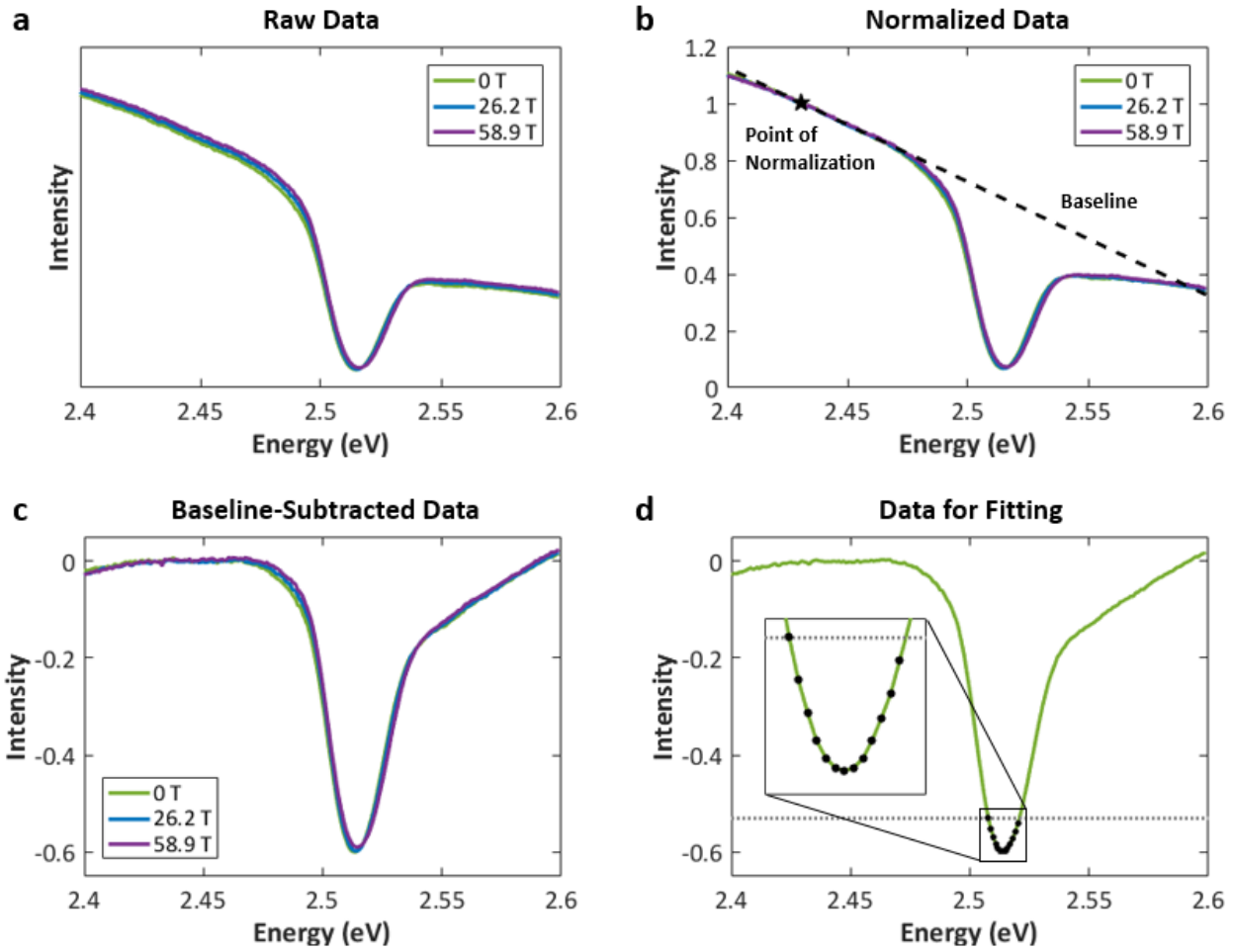

Figure 3.1. (a) Acquired transmission spectra. **(b)** Acquired transmission spectra, normalized at the point marked by the star. The dashed line represents the baseline that was subtracted to yield the data in the next panel. **(c)** Baseline-subtracted transmission spectra. **(d)** Baseline-subtracted transmission spectra at 0 T, showing the points (black dots) below the signal threshold (gray dotted line). Only the black points were fit to a Gaussian to determine the position of the peak.

Using the peak positions obtained from the Gaussian fitting, the two sets of peak shifts (from the +60 T data and -60 T data) were fit to Eq. 3.1 in the text using `nlinmultifit`, a function provided through MATLAB File Exchange.[107] In this way, both sets of data were fit simultaneously to obtain E_0, g_{ex}, and σ. (Fitting g_{ex} and σ independently via $g_{\mathrm{ex}}\mu_B B =$

$(E_+ - E_-)B$ and $\sigma B^2 = \frac{1}{2}(E_+ + E_-)B^2$ yields values that are within 2% of those obtained using `nlinmultifit`.) The inverse of the root mean square error (rmse) squared (i.e. the inverse variance) for each data point from the Gaussian fit was used as the weight in the fit. The 95% confidence intervals for σ are reported in the main text as the errors on the fit. These errors are believed to provide an accurate depiction of the error inherent to the measurement, as changing the signal threshold returned a value of σ that was within the 95% confidence interval of the value reported in the text.

3.4 Results and Discussion

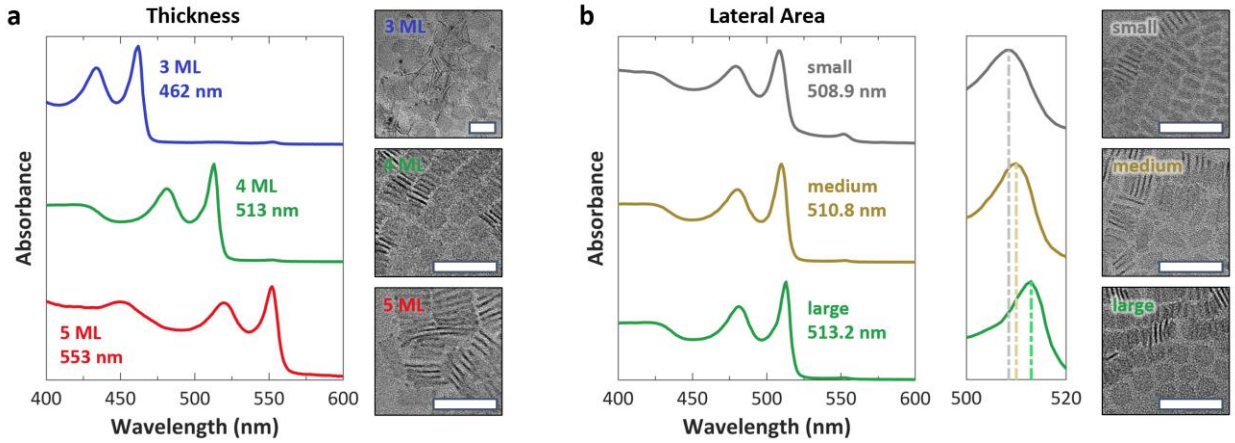

Figure 3.2. UV-Vis absorption spectra and transmission electron microscopy images of **(a)** 3, 4, and 5 ML thick CdSe NPLs and **(b)** small, medium, and large 4 ML thick NPLs.

CdSe NPLs of 3, 4, and 5 ML thickness as well as small, medium, and large lateral areas of 4 ML thickness were synthesized according to previous reports.[58,60,75] As shown in Figure 3.2, the NPLs studied here feature thicknesses of 0.9, 1.2, ad 1.5 nm for 3, 4, and 5 ML NPLs, respectively. Both

4 and 5 ML NPLs typically have widths and lengths around 10-30 nm, whereas currently accessible 3 ML NPLs yield larger lateral size greater than 40 nm across in both directions.[58]

3.4.1 Nanoplatelet Orientation

In these experiments, NPLs were dispersed in a solution of chloroform and poly(butyl methacrylate-*co*-isobutyl methacrylate) and dropcast to form low-scatter films that were then biaxially stretched. To discern whether stretching achieved in-plane orientation of NPLs, SAXS data was acquired in both transmission and reflection geometries. Figure 3.3 shows SAXS data for polymer films containing 5 ML NPLs, before and after applying biaxial strain. Prior to stretching, the transmission pattern (Figure 3.3a) is isotropic, indicating no net NPL orientation in the plane of the film. Anisotropy of the reflection mode pattern (strong scattering in the horizontal direction, as shown in Figure 3.3b) additionally suggests that NPLs preferentially orient perpendicular to the plane of the film in stacks, as has been previously observed.[100,108,109] After being stretched, the transmission and reflection scattering signals (Figure 3.3c,d) are present at the same q value as before, indicating that stacks of NPLs remain with the same spacing. However, the lack of transmission scattering intensity at most detection azimuthal angles in Figure 3.3c suggests that many of the stacks with perpendicularly oriented NPLs have broken apart or rotated from a perpendicular orientation to one in which the stacks lay within the plane of the film. This rotation is corroborated by the reversal of scattering intensity from being primarily in the horizontal direction (Figure 3.3b) to being primarily in the vertical direction (Figure 3.3d).

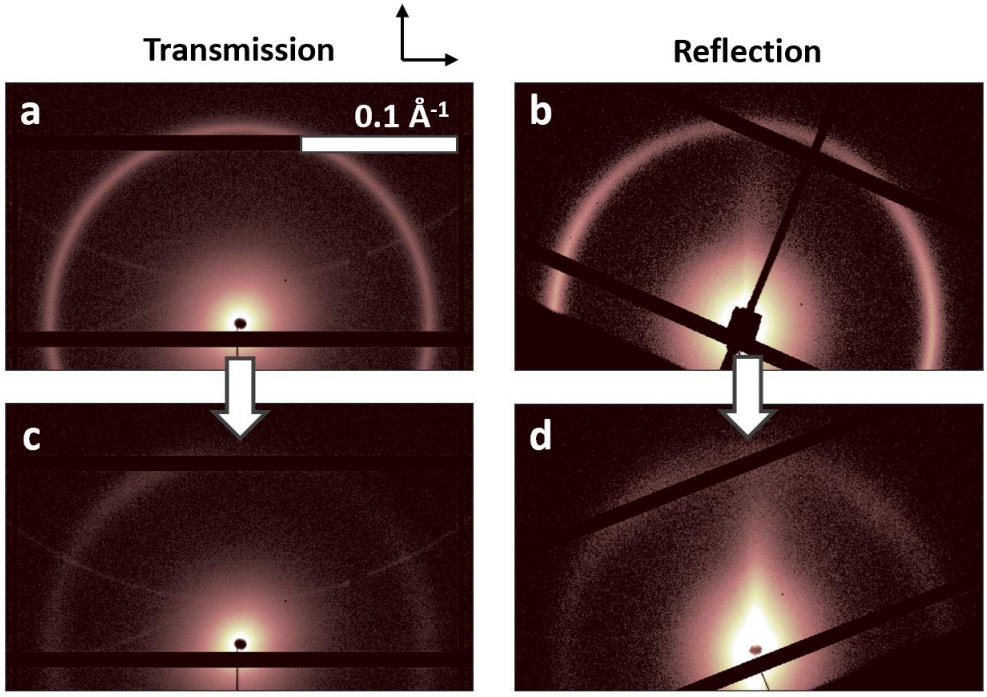

Figure 3.3. Transmission (left column) and reflection (right column) SAXS images of films containing 5 ML CdSe NPLs in polymer **(a, b)** before and **(c, d)** after stretching. Stretching axes are roughly identified by the two black arrows. Intensities are logarithmic and are only consistent between the transmission patterns.

It should be noted that, as shown in Figure 3.3, the scattering intensity after stretching decreases significantly. In part, this is due to a reduction in stretched film thickness (by up to a factor of 4). However, there is the additional consideration that stretching breaks up some of the NPL stacks, as highlighted by the significant reduction of scattering intensity in Figure 3.3c,d and as has been reported previously.[100] The broad vertical streak in Figure 3.3d suggests that the majority of NPLs are not arranged within stacks (which would appear within the ring at higher q) and are instead separated. Unfortunately, for those NPLs that are not arranged in stacks, there is no quantiative way to determine their orientation relative to the plane of the film. However, literature on polymer composites suggests that single NPLs likely align parallel to the flow

direction,[110] although the degree to which this would occur may be subject to the interaction between the NPLs and the polymer matrix.[111]

3.4.2 Magneto-Optical Spectroscopy

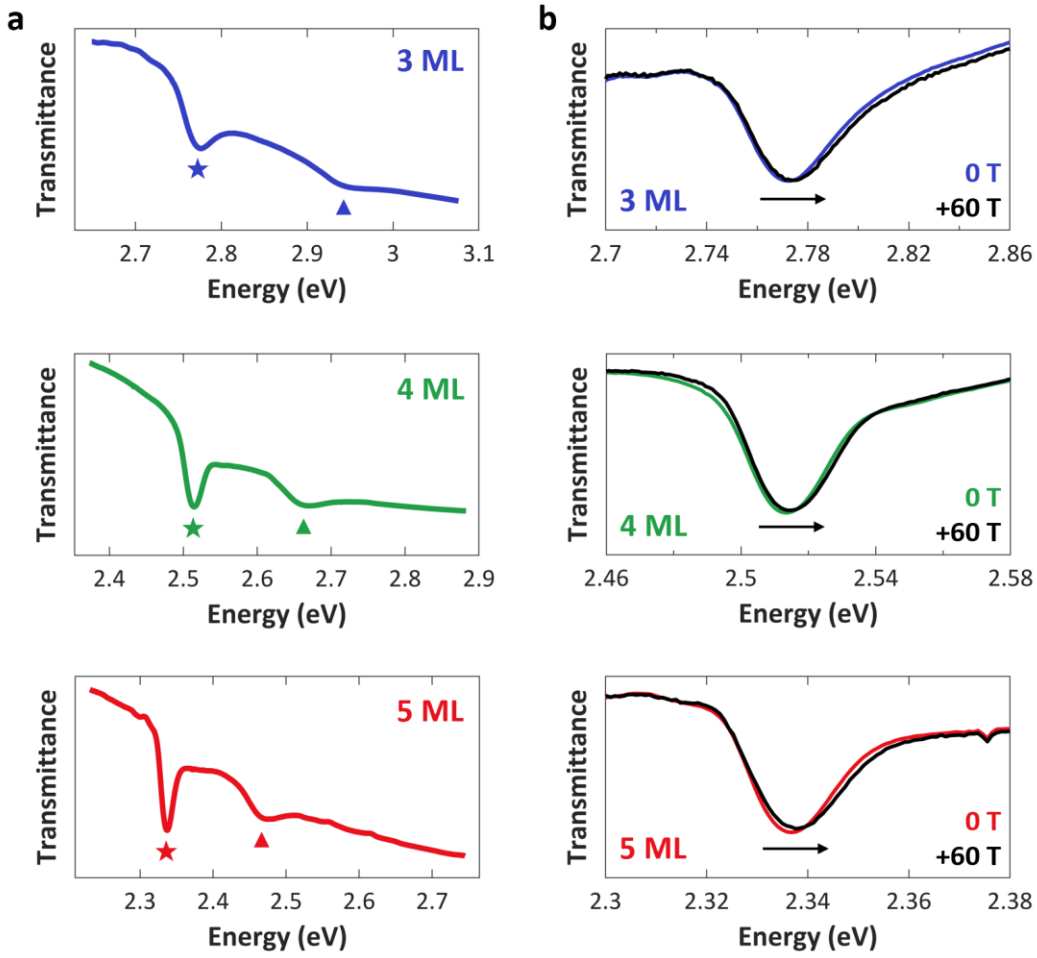

Figure 3.4. (a) Transmission spectra of 3, 4, and 5 ML CdSe NPLs at 0 T (no applied magnetic field) and 4 K. Stars and triangles indicate the heavy-hole and light-hole/split-off exciton transitions, respectively. **(b)** Baseline-subtracted spectra of 3, 4, and 5 ML CdSe NPLs at 4 K with an applied magnetic field of 0 T and 60 T, showing the shift in heavy-hole exciton energy with magnetic field (as indicated by the arrow in each panel).

Figure 3.4a shows transmission spectra at 4 K of oriented 3, 4, and 5 ML NPLs in stretched polymer films at 0 T. Upon application of a magnetic field, the band-edge heavy-hole exciton peak shifts, as shown in Figure 3.4b, and is accompanied by a slight change in the line shape. To track the shift of the heavy-hole exciton in the magnetic field, a linear baseline was subtracted from the transmission spectrum and the peak was fit to a Gaussian function. The resulting peak positions were then used as inputs for fitting to Eq. 3.1 to obtain the diamagnetic shift coefficient, σ.

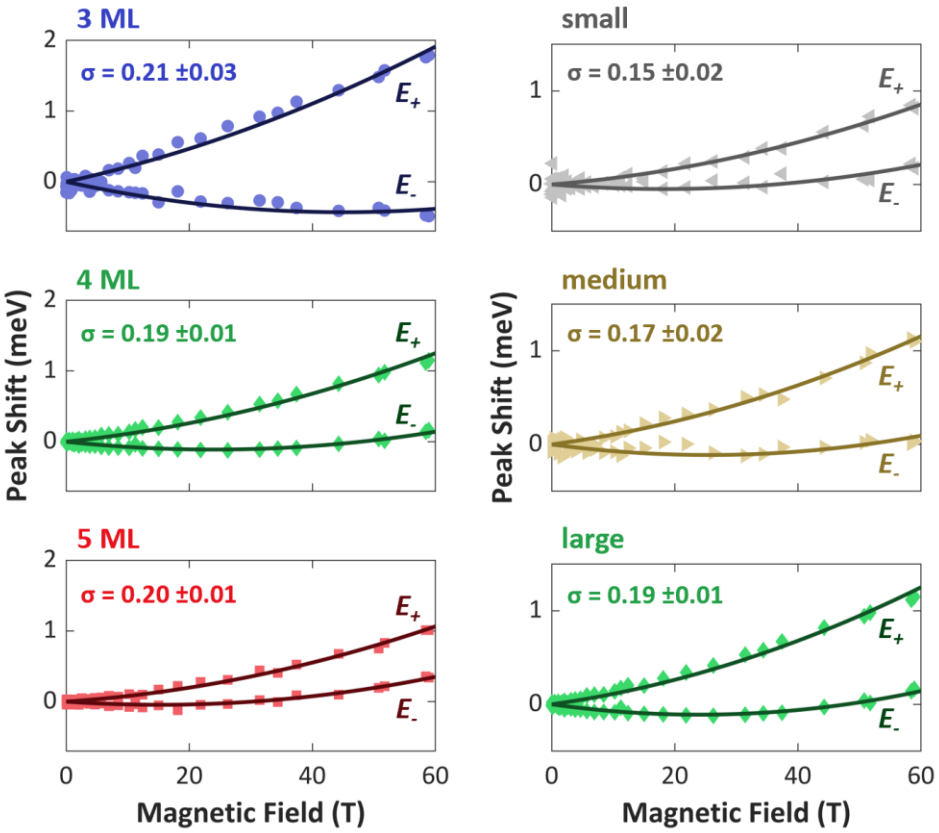

Figure 3.5. Heavy-hole exciton peak shifts for 3, 4, or 5 ML thickness, and for 4 ML NPLs of small, medium, or large lateral area. The vertical scale is consistent between panels in the same column. Diamagnetic shifts for each sample are indicated in units of μeV/T^2.

Figure 3.5 shows the shifts in exciton energy as a function of magnetic field for CdSe NPLs in stretched polymer films. The solid lines depict fits of the data to Eq. 3.1, from which the values of the excitonic g-factors and the diamagnetic shift coefficients are obtained. Notably, by plotting the average exciton energy, $(E_+ + E_-)/2 = \sigma B^2$, as in Figure 3.6, a diamagnetic shift is observed. This shift is clearly quadratic through the full 60 T range, consistent with our estimate that the magnetic fields accessed act as weak perturbations on the tightly bound CdSe NPL excitons. Thus, Eq. 3.2 is appropriate for conversion of the observed diamagnetic shift coefficients to the root-mean-square in-plane exciton radius.

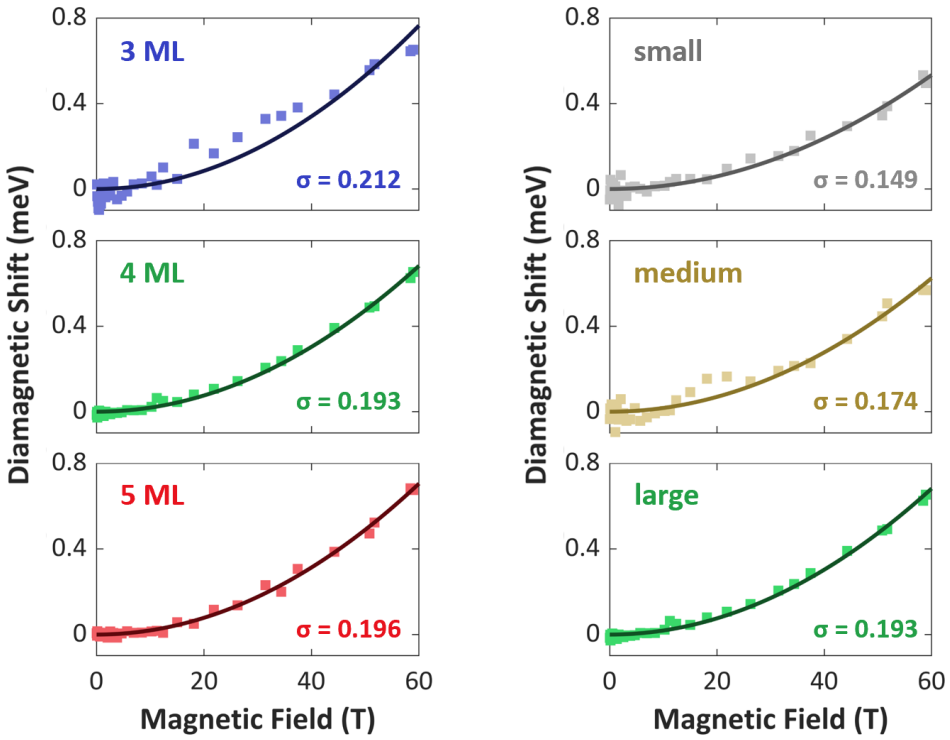

Figure 3.6. Diamagnetic shift, isolated by taking the average excitonic energy of the two states $E_{\text{avg}} = \frac{1}{2}(E_+ + E_-)$, for each set of NPLs. The shift can be fit to σB^2 to obtain the diamagnetic shift coefficient, σ, indicated on each plot in units of μeV/T².

The in-plane exciton radius depends not only on σ, the measured diamagnetic shift coefficient, but also on $\mu_{r,\text{plane}}$, the in-plane reduced mass of the heavy-hole exciton, which we do not experimentally access. Reports of μ_r vary between $0.14m_0$ and $0.21m_0$ (where m_0 is the free electron mass), depending on the literature source and NPL thickness.[11,77,112] The small diamagnetic shifts of 0.15–0.21 μeV/T^2 reported in Figure 3.5 and Figure 3.6 thus suggest in-plane exciton radii in the range of 1.1–1.4 nm for all probed samples. This is significantly smaller than the bulk exciton Bohr radius of 5.4 nm for bulk CdSe and is consistent with large exciton binding energies.

It is important to emphasize that the magnitude of the diamagnetic shift depends on NPL net orientation. When NPLs lie flat in the plane of the polymer film, perpendicular to the direction of the applied magnetic field, a greater diamagnetic shift is expected than when NPLs lie parallel to the direction of the field. Notably, as the exciton lateral extent approaches its vertical extent (approaching a spherical exciton), net orientation effects diminish. Conversely, if the exciton lateral extent approaches large values, such as the bulk Bohr radius (5.4 nm), the observed diamagnetic shift increases quadratically. For example, for an in-plane exciton radius of 2.4 nm, twice as large as the ~1.2 nm radius observed here, a 0.8 μeV/T^2 diamagnetic shift coefficient would result, which is 4 times greater than that observed experimentally. Such a difference would be discernible in these measurements. As a result of this behavior, the possibly that the in-plane exciton radius reported in this work of ~1.2 nm is a result of poor orientation, rather than an actual small exciton size, is small.

3.4.3 Atomistic Electronic Structure Calculations

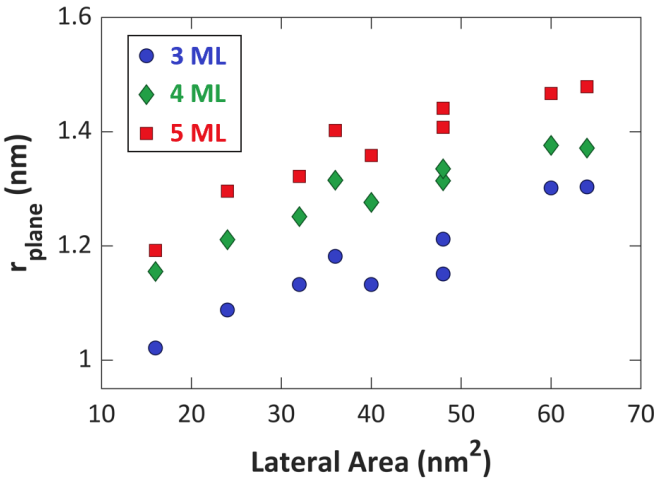

Figure 3.7. Atomistic electronic structure calculations of r_{plane} for 3, 4, and 5 ML CdSe NPLs of varying lateral sizes.

To further probe how NPL dimensions impact exciton size and whether theoretical pictures of NPLs reflect the experiment, our collaborator John Philbin of UC Berkeley performed atomistic electronic structure calculations for a series of 3, 4, and 5 ML CdSe NPLs. Each calculated series spanned a range of NPL lateral sizes, beginning with lateral dimensions small than the bulk exciton Bohr radius (4 nm × 4 nm) and ending with lateral dimensions approaching twice the size of the bulk exciton Bohr radius (8 nm × 8 nm). The calculated in-plane exciton radii, shown in Figure 3.7, are of similar magnitude to the experimentally determined in-plane exciton radii—in the range of 1.0–1.5 nm and depending only weakly on the NPL thickness and lateral area. The increase of the in-plane exciton radius with increasing NPL dimensions (both lateral area and thickness) can be justified on account of the reduction in Coulombic attraction between the electron and hole when the volume of the NPL is increased. Notably, although dielectric screening affects the overall

lateral extent of the exciton, the exciton spatial extent remains small (in the range of 1.2–2.0 nm) even when a larger, less warranted dielectric constant is chosen.

3.4.4 Conclusion

In conclusion, we have prepared films of oriented CdSe NPLs by embedding NPLs in polymer films that were then stretched biaxially. Absorption measurements in pulsed magnetic fields show that the heavy-hole exciton energy shifts with the applied field in a way that can be characterized via the diamagnetic shift coefficient. Diamagnetic shifts of three different thickness and three different lateral area NPLs reveal that the in-plane exciton radius of CdSe NPLs is in each case small, despite the lateral dimensions exceeding those of the conventional bulk CdSe Bohr radius. Atomistic modeling using realistic, discrete NPL structures arrives at similar r_{plane} values and supports the hypothesis that the NPL exciton is a small and relatively compact spheroid, roughly 1.0–1.4 nm in radius.

3.5 Outlook

Arguably, the in-plane exciton spatial extent is still not agreed upon within the scientific community. Following the publication of our work, a study by Morgan and Kelley reported on the spatial extent of the exciton in CdSe NPLs using transient absorption (TA) spectroscopy and found that the exciton spatial extent varied between 18 and 24 nm^2, yielding an exciton radius of 2.7 nm—nearly double that which we report here.[113] This value is roughly three times as large as what we report here when it is converted to a root-mean-square radius according to the relation $r_{\text{rms}} = \sqrt{2}a_B$, yielding 3.8 nm in comparison to our 1.0–1.4 nm. Their major criticism of the small exciton

sizes reported in our work is that they cannot be used to accurately capture the long radiative lifetimes observed for CdSe NPLs at room temperature. Li *et al.* likewise conducted measurements of the exciton spatial extent using TA spectroscopy; through a different method of analysis, they arrived at even larger areas of ~100 nm^2 at room temperature.[114]

Nevertheless, experimental measurements by Scott *et al.* and theoretical calculations by Ayari *et al.* support our picture of small in-plane excitons.[80,115] Additionally, a practical application of our work by Halim *et al.*, in which the optimal NPL lateral size and FRET fluorophore coverage were determined in order to optimize FRET efficiency between CdSe NPLs and a diethienyl benzothiadiazole derivative, likewise confirmed that the NPL exciton spatial extent is small.[116] Given the small, localized exciton area, they found that simply increasing NPL lateral areas to increase absorption cross-sections did not yield improved FRET efficiencies. Likewise, this argument helps rationalize the results of previous studies that have looked at charge transfer between CdSe NPLs and molecular acceptors as a function of NPL lateral area and found that rates decrease as NPL lateral area increases,[60] as the likelihood of the molecular acceptor being bound at the area of exciton localization is lowered.

Given the influence of the exciton spatial extent on both NPL optoelectronic properties and their electronic interactions with other materials, one question that frequently arises is how to manipulate the size of the exciton. One method is via alteration of the external dielectronic environment of the NPL. Ayari *et al.* demonstrated that as the dielectric constant of the surrounding environment is increased, the exciton Bohr radius increases, thereby increasing the excitonic spatial extent.[115] Since organic ligands tend to have similar dielectric constants of around $\varepsilon \approx 2$, the most effective ways of altering dielectric environment are to replace organic ligands with

inorganic ones or to grow a semiconductor shell on the CdSe core. Alternatively, moving the NPLs from a low dielectric environment solvent system such as hexane ($\varepsilon = 1.9$) to acetonitrile ($\varepsilon = 38$) has also been shown to be highly effective for HgTe NPLs, although this method did not work for CdSe, CdTe, or HeSe.[117]

4 Effect of Nanoparticle Dimensionality on Rates of Electron Transfer

4.1 Introduction

Semiconductor nanoparticles (NPs) have been successfully implemented in numerous optoelectronic and photovoltaic applications, owing to synthetic control over the electronic structure via particle composition, size, and morphology. In many of these applications, NP shape has already been recognized as an additional way of improving functionality; NPs of various morphologies, such as nanorods, nanoplatelets, and tetrapods, have been used for solar cells,[118–127] photocatalysts,[128–130] light-emitting diodes,[131,132] lasers,[58,59,133] and biosensors,[134] achieving superior results compared to devices constructed from their spherical quantum dot counterparts.

Colloidally prepared, two-dimensional semiconductor nanoplatelets (NPLs) present a promising alternative to the zero-dimensional quantum dots (QDs) that are used in the aforementioned applications, owing to strong light absorption and the possibility of rapid charge transfer. NPLs are well-suited to function as light absorbers or emitters since large total volumes

---

This chapter is adapted from:

Brumberg, A.; Diroll, B. T.; Nedelcu, G.; Sykes, M. E.; Liu, Y.; Harvey, S. M.; Wasielewski, M. R.; Kovalenko, M. V.; Schaller, R. D. Material Dimensionality Effects on Electron Transfer Rates Between $CsPbBr_3$ and CdSe Nanoparticles. *Nano Lett.* **2018**, *18* (8), 4771–4776.

result in large per-particle absorption cross-sections that are typically an order of magnitude greater than those of QDs,[8,135,136] while near-zero dispersity of NPL thickness leads to narrow band-edge absorption and emission that can be tuned synthetically.[11,12,58] Studies of CdSe NPLs have also shown that these structures exhibit faster rates of energy transfer between particles than QDs.[44,45] Fast rates were attributed to large space filling of the acceptors in proximity to donors, and similar considerations could suggest that charge transfer may likewise occur more rapidly between NPLs.

For molecular systems, Marcus theory provides a description of the rate of electron transfer between two molecules as a function of separation distance and driving force.[137] While driving force remains straightforward to calculate for NP systems provided that redox levels are known, other parameters, such as distance, are more complex, raising the question of whether a standard form of Marcus theory remains valid for systems comprised of spatially-extended NPs. Others have pursued this question in QD-donor and molecular-acceptor systems by investigating the dependence of the electron transfer rate on distance and driving force.[138–141] Owing to these studies, an analogous formation of Marcus theory for QDs with strongly bound acceptors has been reported, in which electron transfer is accompanied by hole excitation in the donor.[140,142,143] On the other hand, more recent studies of charge transfer in systems in which both the electron donor and the electron acceptor are comprised of QDs suggest that Marcus theory is still valid provided that the final electronic states are summed over.[144] While both approaches relate that Marcus theory necessitates modification when describing charge transfer to or from a NP, they do not contemplate the additional factor of NP shape (dimension), which must be considered to relate rates of electron transfer for NPs of the same energetics but different physical extent.

Evaluating the role of dimensionality is complicated by the need to control for factors that could result in different rates of electron transfer, independent of the particle shape. Fortunately, for some materials it is possible to synthesize NPs of different shapes of dimensions (such as zero-dimensional QDs and two-dimensional NPLs) yet isoenergetic band gaps, allowing for the charge transfer driving force to be kept constant. For example, studies looking at the effect of lateral area of NPLs[60] or aspect ratio of nanorods[145] on charge transfer to a molecular acceptor have successfully compared rates between particles of varying sizes and nearly isoenergetic band gaps. Distance is a more difficult factor to control when the acceptor is not chemically bound to the donor, although the use of identical surface ligands can accomplish such a task.

In this chapter, the impact of NP dimensionality on charge transfer rates is studied using $CsPbBr_3$ and CdSe NPs. Both $CsPbBr_3$ and CdSe can be synthesized as NPLs,[11,37,75] presenting an appropriate system in which to study the effect of dimensionality on electronic interactions. Moreover, $CsPbBr_3$ has recently received significant attention both in optoelectronic and photovoltaic applications,[146–149] while CdSe represents a well-studied material for which it is possible to synthesize QDs and NPLs of not just the same crystal structure, but also the same band gap. Zero- and two-dimensional (0D and 2D) NPs of both $CsPbBr_3$ and CdSe are studied so as to compare electronic interactions between 0D-0D, 0D-2D, and 2D-2D systems, extending the work of previous studies that have demonstrated electron transfer between 0D cesium lead halide perovskites and 0D cadmium chalcogenides.[150,151] Electron transfer is observed via transient absorption (TA) and static and time-resolved photoluminescence (PL and trPL) measurements. Electron transfer rates are extracted from time-resolved dynamics and become faster in systems

containing 2D NPs versus systems with 0D NPs, relaying a potentially benefit of spatially extended structured in derived optoelectronics.

4.2 Experimental Methods

4.2.1 Nanoparticle Synthesis

CdSe QDs were synthesized using an adaptation[60] of a previously published[152] injectionless technique. 186 mg of cadmium acetylacetonate, 12 mg of selenium powder, 25 mL of octadecene, and 1.0 mL of oleic acid were added to a three-neck flask and heated to 120 °C for one hour under vacuum. Then, the solution was heated to 240 °C under nitrogen. Aliquots were extracted from the reaction flask and measured by UV-vis spectroscopy until the first excitonic feature reached 544 nm, at which point the reaction was cooled back to room temperature. The QDs were precipitated by adding isopropanol and then centrifuging and repeating as necessary with hexane and isopropanol. The QDs were then dispersed and stored in hexane.

CdSe NPLs were synthesized according to previously published procedures with slight modifications,[11,58,75] as discussed in Chapter 1, Section 1.4. First, a cadmium myristate precursor was prepared by adding 40 mL of 0.05 M cadmium nitrate in methanol to 240 mL of 0.025 M sodium myristate in methanol; the resulting precipitate was washed with methanol and dried under vacuum overnight.

Then, 170 mg of cadmium myristate and 14 mL of octadecene were placed in a three-neck flask and degassed for 30 minutes under vacuum. The solution was then heated under nitrogen to 250 °C, at which point 12 mg of selenium powder (sonicated in 1 mL of octadecene) was rapidly

injected. After 60 seconds, 90 mg of finely-ground cadmium acetate was added to the reaction flask, which was maintained at 250 °C for 10 minutes. The reaction was then allowed to cool; when the temperature reached 70 °C, 2 mL of oleic acid and 15 mL of hexane were added. The solution was then centrifuged at 14500 RPM and the resulting pellet was dissolved in 1-methylcyclohexane and filtered through a 0.2 μm PTFE syringe filter.

$CsPbBr_3$ QDs were prepared according to a previously published procedure.[153] First, a solution of cesium oleate was prepared by heating 0.407 g of cesium carbonate (1.25 mmol), 1.25 mL of oleic acid, and 20 mL of octadecene to 120 °C under vacuum for one hour and then to 150 °C under nitrogen until the cesium carbonate was fully dissolved. Before use, the cesium oleate was heated to 100 °C in order to resolubilize the cesium oleate.

Then, 0.069 g of $PbBr_2$ (0.19 mmol) and 5 mL of octadecene were added to a three-neck flask and dried under vacuum for one hour at 120 °C, at which point 0.5 mL of dried oleylamine and 0.5 mL of dried oleic acid were injected. After the $PbBr_2$ had dissolved completely, the temperature was raised to 180 °C and 0.4 mL of cesium oleate was injected. After 5 seconds, the flask was cooled using a water bath. The QDs were then centrifuged and redissolved and stored in toluene.

$CsPbBr_3$ NPLs were prepared according to a previously published synthesis of $CsPbBr_3$ QDs with major modifications.[153] (The detailed procedure for the synthesis of these $CsPbBr_3$ NPLs was later published separately.[154]) Briefly, a solution of 61.5 mmolal $PbBr_2$ in mesitylene was obtained after $PbBr_2$, pre-dried oleic acid (0.896 g) and pre-dried oleylamine (0.893 g) were mixed in a 25 mL three-neck flask containing mesitylene (4.32 g). The flask was connected to a Schlenk line, flushed three times at room temperature in order to remove the excess of O_2, and heated to

130 °C. Cesium oleate (0.8 mL) was swiftly injected and the reaction mixture was immediately cooled down by a water bath.

4.2.2 Film Preparation

In order to create films of $CsPbBr_3$ and CdSe mixed in controlled ratios, first the concentration of NPs in the stock solutions of CdSe and $CsPbBr_3$ were determined according to Beer's Law, $A = \varepsilon bc$. The molar absorptivity of each solution at 400 nm, ε_{400}, was calculated according to

$$\varepsilon_{400}[\mathrm{M^{-1}\ cm^{-1}}] = \frac{N_A \sigma_{400}[\mathrm{cm^2}]}{1000 \ln 10} \tag{4.1}$$

where N_A is Avogadro's number and σ is the absorption cross-section of the material.[155] Absorption cross-sections were measured using transient absorption (TA) spectroscopy using a 400 nm pump wavelength. The TA signal at different pump powers was measured at 6 ns and then fit to $A - B\exp(-\sigma x)$, where x is the pump fluence in photons/cm^2. For the $CsPbBr_3$ QDs, the value for the absorption cross-section was taken from Ref. 156.

For film preparation, portions of the stock solutions of $CsPbBr_3$ and CdSe were dried down and then redispersed in either hexanes or methylcyclohexane at the desired concentration of particles. Solutions using a mixture of $CsPbBr_3$ and CdSe at the desired mole ratio were then prepared and mixed using a Vortex mixer. 1-2 μL of each solution was then dropcast onto a glass coverslip and allowed to dry.

4.2.3 Static Characterization

UV-vis absorption and photoluminescence excitation spectra were acquired on commercial spectrophotometers and spectrofluorometers, respectively. Static photoluminescence spectra were collected from samples photoexcited by a 35 ps, 405 nm pulsed diode laser through a fiber optic to a thermoelectrically-cooled charge-coupled device (CCD). Emission was detected through a 420 nm longpass filter.

4.2.4 Time-Resolved Spectroscopy

Time-resolved measurements were performed on samples photoexcited using the 400 nm, frequency-doubled output of a 35 fs, Ti:sapphire laser operating at 2 kHz. For transient absorption measurements, a small portion of the 800 nm Ti:sapphire output was focused into a sapphire plate to produce a white light probe. The pump repetition rate was reduced to 1 kHz, and single shot spectra were collected and averaged to produce transient absorption data. For time-resolved photoluminescence, PL was detected using a single-photon sensitive streak camera. Emission was detected through a 420 nm longpass filter.

4.3 Data Processing

4.3.1 Deconvolution of $CsPbBr_3$ and CdSe Components in Emission

The emission from the $CsPbBr_3$ component of the films containing mixtures of the two materials in static and time-resolved photoluminescence (PL) was analyzed by fitting the spectra of the pure materials to the spectrum of the mixture:

$$\begin{bmatrix} p_1 & c_1 \\ \vdots & \vdots \\ p_m & c_m \end{bmatrix} \begin{bmatrix} tp_1 & \cdots & tp_n \\ tc_1 & \cdots & tc_n \end{bmatrix} = \begin{bmatrix} f_{11} & \cdots & f_{1n} \\ \vdots & \ddots & \vdots \\ f_{m1} & \cdots & f_{mn} \end{bmatrix} \tag{4.2}$$

where p is the spectrum of pure $CsPbBr_3$, c is the spectrum of pure CdSe, and f is the spectrum of the mixture (static when $n = 1$ and time-resolved when $n > 1$). The weights for p and c as a function of time (or overall, in the case of static PL), tp_i and tc_i, were obtained using matrix division in MATLAB.

It should be noted that the above procedure assumes that the p and c spectra are static and thus do not have dynamics of their own. For time-resolved PL, p and c were determined by taking the sum of the time-resolved spectra over time to obtain a pseudo-static spectrum. For the CdSe QDs and NPLs and $CsPbBr_3$ QDs, the integrated spectrum matched the time-resolved spectra fairly well, and so the assumption that the spectra were static was fairly valid. In the case of $CsPbBr_3$ NPLs, although its spectral profile does evolve over time, the results obtained from analyzing peak dynamics via integration (as opposed to the method outlined here) yielded essentially identical results. We thus chose to use our matrix fitting procedure for analysis of all four mixture types since three of the four series of films exhibited spectral overlap between CdSe and $CsPbBr_3$ and satisfied the assumption that the pure CdSe and $CsPbBr_3$ did not evolve over the time range investigated.

4.3.2 Fitting the CdSe Emission in PLE

When monitoring the emission of CdSe NPLs in mixed films of CdSe NPLs and $CsPbBr_3$ QDs, even at the lower energy wavelengths of 560+ nm, there is some emission that is still present from the strongly luminescent $CsPbBr_3$ QDs. As such, when analyzing photoluminescence

excitation data, the emission from 530 to 600 nm was fit to a Gaussian (for the CdSe emission) on top of a second-order polynomial (to account for the tail of the $CsPbBr_3$ emission).

4.4 Results and Discussion

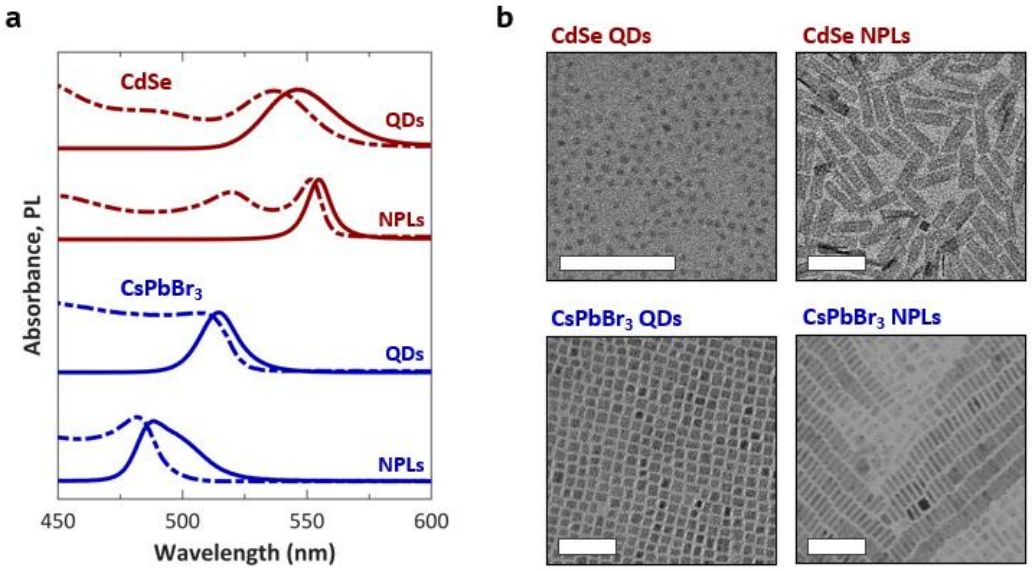

Figure 4.1. (a) Normalized solution absorption (dashed lines) and film photoluminescence (solid lines) spectra, offset vertically for clarity and **(b)** TEM images of CdSe QDs and NPLs and $CsPbBr_3$ QDs and NPLs. TEM scale bars are 50 nm.

Absorption and emission spectra of the CdSe and $CsPbBr_3$ QDs and NPLs used in this work appear in Figure 4.1a. Notably, the examined zinc blende CdSe QDs and NPLs exhibit nearly isoenergetic emission maxima at 546 and 555 nm, respectively, placing the difference in their band gaps at approximately 37 meV, which is only moderately larger than thermal energy at room temperature (26 meV). As shown in Figure 4.1b, the particles present quite different shapes and sizes. The CdSe QDs are roughly 3 nm in diameter,[152] whereas the 5.5 monolayer-thick CdSe

NPLs are 1.5 nm thick and 8 nm × 34 nm in lateral size. The examined $CsPbBr_3$ QDs are roughly 8 nm on each side with a nearly cubic morphology,[153] similar to the side lengths of 10-11 nm and 12-14 nm of the $CsPbBr_3$ NPLs but larger than the 3-4 nm thickness.

Stock solutions of either $CsPbBr_3$ or CdSe NPs in hexane were mixed in controlled ratios by concentration (i.e. particle number) and then dropcasted, such that solvent rapidly evaporated. Particle ratios spanned the range of dilute to concentrated amounts of one composition in the other in order to explore the additive kinetics of electronic interactions. When $CsPbBr_3$ and CdSe NPs are mixed, substantive regions of mixed particles do form, as shown by TEM in Figure 4.2. We note this because, reports show that, under some conditions, disparate particle types can resist mixing in attempts at forming ordered binary superlattices,[157–159] which are not pursued here.

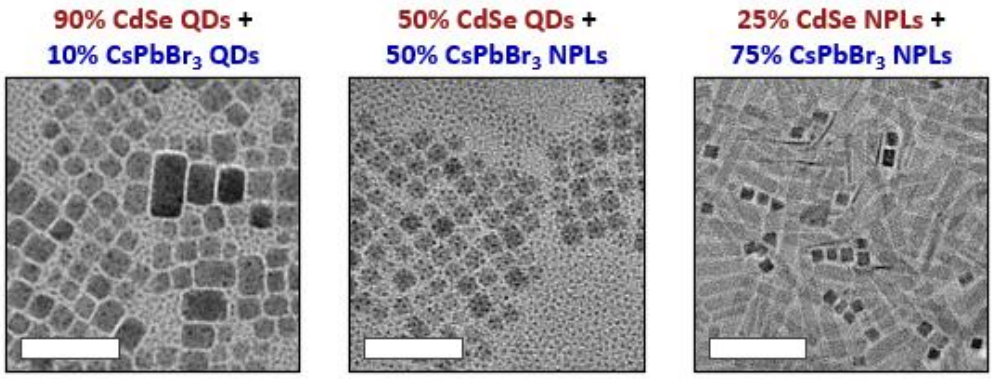

Figure 4.2. TEM images of CdSe and $CsPbBr_3$ NPs mixed together. In each case, substantive mixed regions of NPs are observed. TEM scale bars are 50 nm.

In mixed particle films where different particle types surround one another, electron transfer (ET) and fluorescence resonance energy transfer (FRET) may occur. As shown in

Figure 4.3, ET is possible in our system, as the measured conduction band of $CsPbBr_3$ is more reducing than that of CdSe by ~50 to 150 meV.[54,160,161] FRET from $CsPbBr_3$ to CdSe is also possible, as $CsPbBr_3$ emission overlaps with CdSe absorption (see Figure 4.1a).

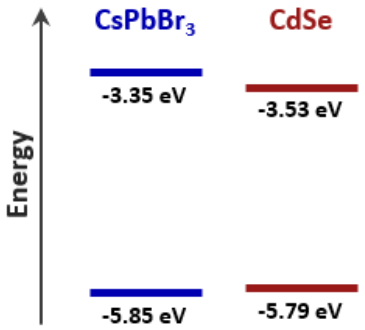

Figure 4.3. Conduction and valence band levels of $CsPbBr_3$ QDs and CdSe NPLs, based on values reported in Refs. [160] and [54]. Although the exact energies vary for QDs and NPLs of each material, electron transfer is energetically favorable for each combination of $CsPbBr_3$ and CdSe NPs.

4.4.1 Identification of Electronic Processes

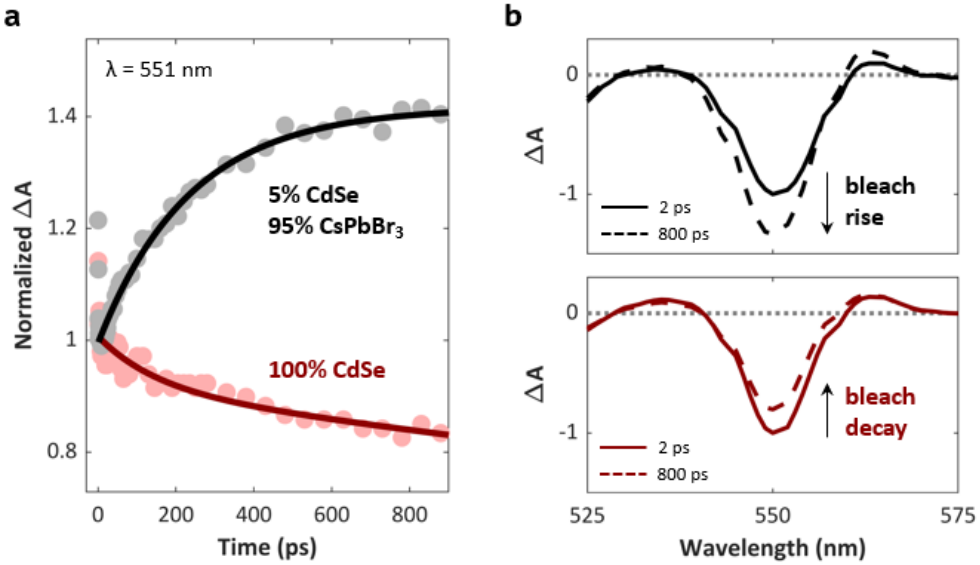

Figure 4.4. Evidence for an influx of electrons in CdSe NPLs from $CsPbBr_3$ QDs through transient absorption (TA). **(a)** TA dynamics of the CdSe NPL bleach, monitored at 551 nm, in films excited at 400 nm.

While the bleach of the CdSe film decays over time, the decay in a film with both CdSe NPLs and $CsPbBr_3$ QDs slows down as the fraction of $CsPbBr_3$ is increased until a rise in the bleach is seen instead for films of 5% CdSe and 95% $CsPbBr_3$. Solid lines are exponential fits to the data. **(b)** TA spectra of the same films as in (a) at 2 ps (solid lines) at 800 ps (dashed lines).

To probe the electronic dynamics in dropcast films of $CsPbBr_3$ and CdSe, low fluence 400 nm excitation was used so as to avoid multiexcitonic processes. Figure 4.4a shows the TA dynamics of the CdSe NPL absorption bleach that appears at 551 nm, arising from state-filling of the conduction (and/or valence band—see footnote†).[162,164] For a neat CdSe NPL film, the bleach decays slowly over a 1 ns time window, conveying a loss of conduction band electrons through recombination. Conversely, a distinct rise of the CdSe bleach occurs for a mixed film containing 95% $CsPbBr_3$ QDs and 5% CdSe NPLs. Since pure $CsPbBr_3$ lacks spectral signatures near 551 nm, the rise of the 551 nm bleach relates a clearly increasing population of electrons in the CdSe conduction band. The differing dynamics of the pure and mixed films is also apparent from the time-resolved spectra presented in Figure 4.4b. Note that without further investigation, we cannot identify whether this increasing population of electrons is accompanied by an increased population

† At the time of writing, no formal investigations into the nature of the CdSe NPL bleach had been published, and the accepted consensus was that the bleach of CdSe NCs (generally speaking, regardless of NC shape) arises from state-filling of the conduction band. Following the publication of our work in 2018, Morgan *et al.* published an investigation specifically into the transient absorption response of CdSe NPLs, which found that state-filling of both the conduction band (by electrons) *and* the valence band (by holes) contributes to the heavy-hole bleach signal.[162] Furthermore, an additional work in 2019 found that the bleach of well-passivated CdSe NCs is likewise influenced by the presence of holes, suggesting that the TA signal of CdSe NCs should not be assumed to arise from solely electron state-filling.[163] **Nevertheless, the production of the heavy-hole bleach from either conduction band and/or valence band state-filling does not alter the results of our work. The rise in the bleach observed in Figure 4.4b could be from electron transfer from $CsPbBr_3$ to CdSe, hole transfer from $CsPbBr_3$ to CdSe, or both electron and hole transfer (i.e. energy transfer). We show that energy transfer does not appear to be present. Though we cannot really differentiate between hole vs electron transfer, the energy levels presented in**

Figure 4.3 suggest that electron transfer is more likely to be the dominant mechanism of electronic interaction.

of holes in the valence band as well; that is, we do not know whether the observed dynamics are a result of electron transfer, energy transfer, or both.

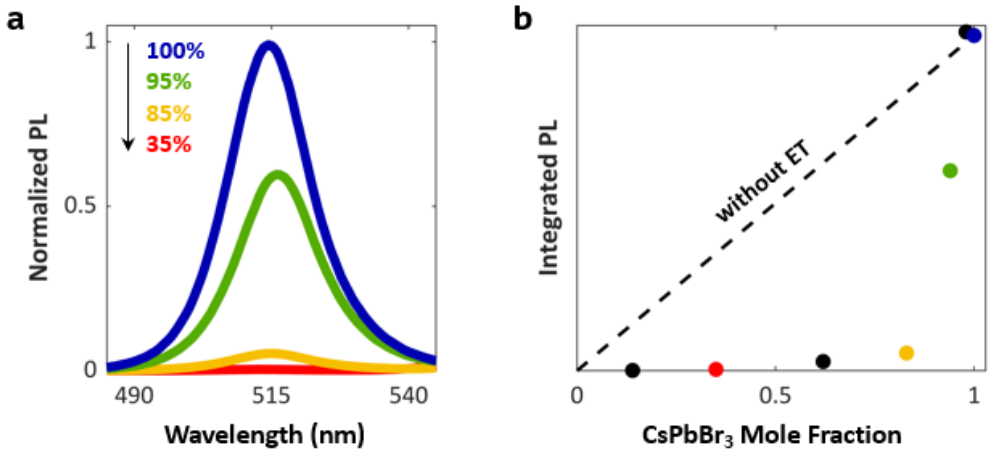

Figure 4.5. Evidence for an influx of electrons into CdSe NPLs from $CsPbBr_3$ QDs through static PL. **(a)** Static PL spectra of films of $CsPbBr_3$ QDs and CdSe NPLs, normalized by the absorption of each film at the excitation wavelength of 405 nm. The percentages indicate the fraction of $CsPbBr_3$ in each film. As the fraction of $CsPbBr_3$ is decrease and the corresponding fraction of CdSe is increased, the PL of $CsPbBr_3$ is drastically quenched, much more than what would be expected by the reduced fraction of $CsPbBr_3$. **(b)** The integrated PL intensity of the $CsPbBr_3$ emission shown in (a), as compared to the intensity that would be expected for each film based on its fraction of $CsPbBr_3$ in the absence of any electron or energy transfer.

With increasing CdSe NPL fraction, more instances of electron or energy transfer from $CsPbBr_3$ to CdSe can occur, because the latter acts as an acceptor for each process. To gain more insight as to which process dominates, we turn to photoluminescence techniques. Figure 4.5a shows static PL spectra of a neat $CsPbBr_3$ QD film and mixed films containing 95%, 85%, or 35% $CsPbBr_3$ excited at 405 nm. A nearly complete drop of PL intensity is observed for films containing 85% $CsPbBr_3$ QDs (15% CdSe NPLs). Furthermore, Figure 4.5b displays a nonlinear drop in integrated $CsPbBr_3$ PL intensity as the mole fraction of $CsPbBr_3$ is decreased (CdSe fraction increased). Together, the panels in Figure 4.5 demonstrate that either electron transfer or FRET successfully quench $CsPbBr_3$ emission in mixed films.

Photoluminescence excitation (PLE) spectroscopy was also performed to evaluate whether electron transfer, FRET, or both represent a main pathway through which electrons are transferred to CdSe. As shown in Figure 4.6a, PLE spectra of mixed films do not show increased CdSe emission for excitation wavelengths where $CsPbBr_3$ is excited, indicating that $CsPbBr_3$ does not transfer energy to CdSe after photoexcitation with any appreciable efficiency. This suggests that the rising CdSe TA signals with time and the quenched PL of $CsPbBr_3$ result from electron transfer.

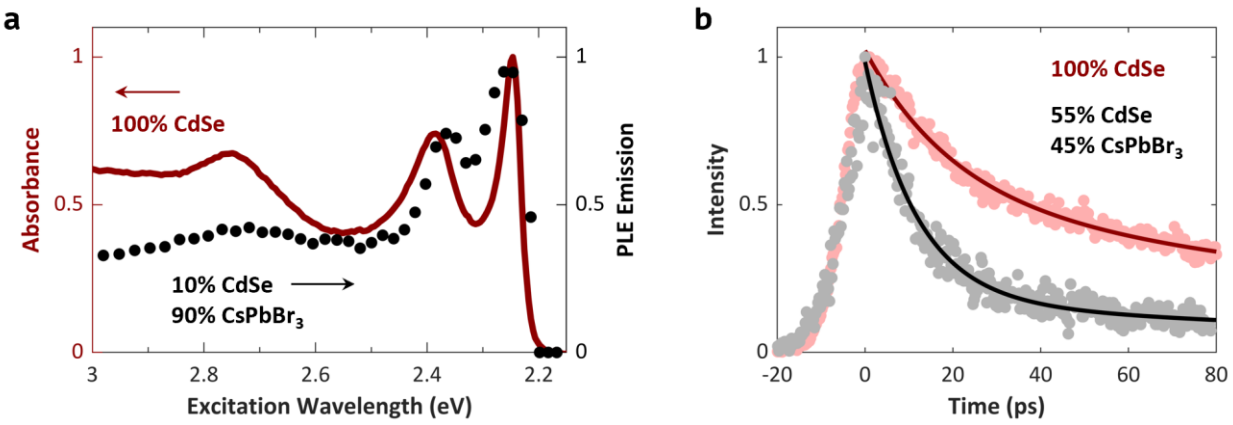

Figure 4.6. Evidence for a lack of hole transfer accompanying electron transfer. **(a)** PLE spectrum (black dots) of a film with 5% CdSe NPLs and 95% $CsPbBr_3$ QDs overlaid with the absorption spectrum (dark red line) of neat CdSe NPLs. **(b)** Time-resolved PL of CdSe NPLs in (red) a neat film of CdSe NPLs versus (black) a mixed film containing 55% CdSe NPLs and 45% $CsPbBr_3$ NPLs. Solid lines are biexponential fits to the data.

Time-resolved PL at low fluence furthers supports dominance of electron transfer in this mixed system. Figure 4.7 shows trPL of the $CsPbBr_3$ component, which becomes shorter-lived in mixed films, indicating outflow of electrons from $CsPbBr_3$ into CdSe. Notably, trPL of the CdSe component (shown in Figure 4.6b) does not exhibit the slowed PL decay or rise in intensity with time that would be expected if energy transfer were providing CdSe with additional excitons that could radiatively recombine. This corroborates PLE in suggesting that electron transfer constitutes the dominant pathway of electronic interaction between $CsPbBr_3$ and CdSe NPs.

4.4.2 Quantification of Electron Transfer Rates

The multiple panels in Figure 4.7 correspond to trPL of $CsPbBr_3$ for four series of films comparing particle dimensionality (CdSe QDs or NPLs mixed with either $CsPbBr_3$ QDs or NPLs). All four sets of films relate increasing rates of electron transfer as the CdSe particle fraction is

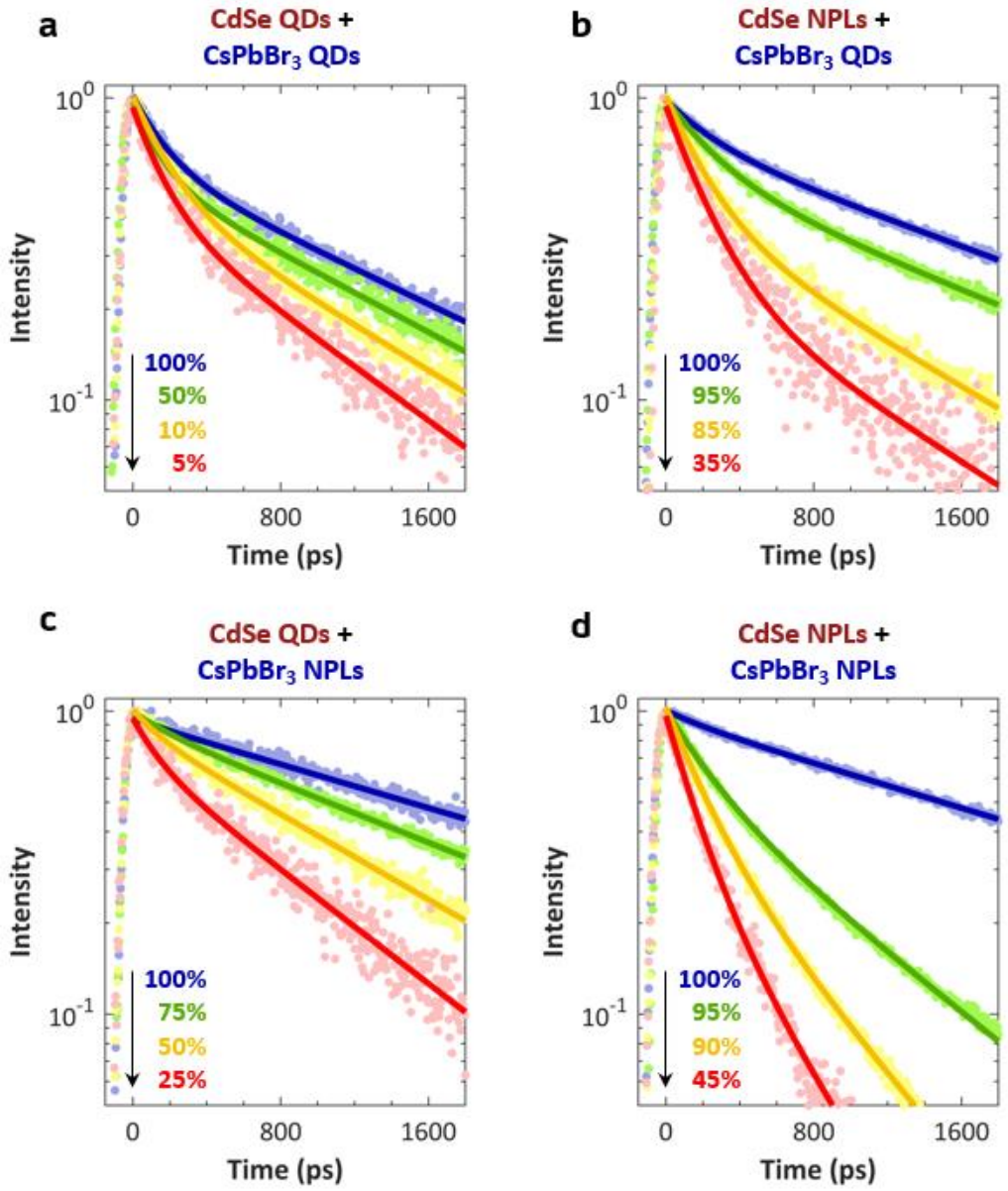

Figure 4.1. Time-resolved PL decay dynamics of the $CsPbBr_3$ emission in mixes of **(a,c)** CdSe QDs or **(b,d)** CdSe NPLs, mixed with either **(a,b)** $CsPbBr_3$ QDs or **(c,d)** $CsPbBr_3$ NPLs. As the fraction of $CsPbBr_3$ is decreased and the fraction of CdSe is increased, the PL decay of the $CsPbBr_3$ emission gets faster. In the mixes containing CdSe QDs, the amount of CdSe required to see fast PL decay is much higher compared

increased, as expected from the additive kinetics of electron transfer. However, much higher amounts of CdSe QDs are needed in order to observe significant differences in the PL decay as compared to CdSe NPLs. For example, in films containing $CsPbBr_3$ NPLs and CdSe NPLs (Figure 4.7d), even with only 5% CdSe, a substantial drop in PL intensity (corresponding to much faster PL decay and electron transfer) is observed. Conversely, in films containing $CsPbBr_3$ QDs and CdSe QDs (Figure 4.7a), even when the film is 95% CdSe, the drop in PL intensity is comparatively small.

Because the driving force for charge transfer in films containing $CsPbBr_3$ QDs versus those containing $CsPbBr_3$ NPLs is not identical in the present measurements, the most direct comparisons that can be made are for films composed of fixed types of $CsPbBr_3$ particles. Figure 4.7a,b compares CdSe QDs versus CdSe NPLs for films containing $CsPbBr_3$ QDs, and Figure 4.7c,d makes the same comparison for films containing $CsPbBr_3$ NPLs. In both cases, it is apparent that CdSe NPLs function as higher efficiency electron acceptors. Because the band gaps of CdSe QDs and NPLs are approximately isoenergetic, the driving force for charge transfer is fixed and does not contribute differences in the observed dynamics, which instead suggests that the disparity of response arises from particle dimensionality. Additional observations in support of this statement are derived from experiments repeated with larger CdSe QDs that absorb near 553 nm and emit near 586 nm, placing the difference in driving force between these CdSe QDs and the CdSe NPLs (calculated from the difference in their emission energies) at 118 meV. Time-resolved PL of films containing these CdSe QDs paired with $CsPbBr_3$ QDs suggest that electron transfer rates are still slow, even though CdSe QDs with a much larger driving force for electron transfer from $CsPbBr_3$ in comparison to the examined CdSe NPLs are employed.

To quantify the observed differences in rates, the $CsPbBr_3$ trPL decay dynamics for each film are fit to biexponential decays, and an amplitude-weighted average lifetime is calculated. In a mixed film containing both $CsPbBr_3$ and CdSe particles, PL decay in $CsPbBr_3$ arises both from the decay processes that occur in pure $CsPbBr_3$ and owing to electron transfer to CdSe. The rate of PL decay in the mixed film can therefore be expressed as

$$k_{\text{mix}} = (1 - x)k_{\text{CsPbBr}_3} + xk_{\text{ET}} \tag{4.3}$$

such that

$$k_{\text{ET}} = \frac{k_{\text{mix}} - (1 - x)k_{\text{CsPbBr}_3}}{x} \tag{4.4}$$

where $\tau_{\text{mix}} = 1/k_{\text{mix}}$ and $\tau_{\text{CsPbBr}_3} = 1/k_{\text{CsPbBr}_3}$ are the amplitude-weighed $CsPbBr_3$ emission lifetimes of the mixed and pure films, respectively, k_{ET} is the rate of electron transfer, and x is the fraction of $CsPbBr_3$ particles in the film that undergo electron transfer. Here, x is calculated by assuming that any decrease in intensity at long times (i.e., 1.8 ns, significantly later than the sub-nanosecond timescale on which electron transfer occurs) beyond that of the neat film must stem from electron transfer that occurred prior, since delay at long times is governed by that of neat $CsPbBr_3$. As such, the ratio of intensities at long times for the film containing both $CsPbBr_3$ and CdSe in comparison to the pure $CsPbBr_3$ film gives the fraction of $CsPbBr_3$ particles that did not undergo electron transfer, $1 - x$, from which x can be determined.

Table 4.1 and Table 4.2 provide the rates of electron transfer for each film obtained from fitting the trPL decays shown in Figure 4.7. Films with either CdSe QDs or NPLs and the same type of $CsPbBr_3$ NPs, such as QDs, can be compared directly to determine what effect dimensionality plays on the rates of electron transfer. The corresponding columns in Table 4.1 and

Table 4.2 show that, for equivalent fractions of CdSe, films containing CdSe NPLs exhibit faster rates of electron transfer.

Table 4.1. Electron transfer rates k_{ET} from $CsPbBr_3$ QDs to indicated CdSe NPs as a function of CdSe fraction.

CdSe Fraction	**k_{ET} ($\times 10^{-3}$ ps^{-1}) w/ CdSe QDs**	**k_{ET} ($\times 10^{-3}$ ps^{-1}) w/ CdSe NPLs**
10 %	-	1.4 ±0.2
15-25 %	-	2.1 ±0.2
40-55 %	1.9 ±0.4	2.2 ±0.2
75-85 %	2.2 ±0.3	3.3 ±0.8
90 %	2.2 ±0.3	-

Table 4.2. Electron transfer rates k_{ET} from $CsPbBr_3$ NPLs to indicated CdSe NPs as a function of CdSe fraction.

CdSe Fraction	**k_{ET} ($\times 10^{-3}$ ps^{-1}) w/ CdSe QDs**	**k_{ET} ($\times 10^{-3}$ ps^{-1}) w/ CdSe NPLs**
10 %	1.1 ±0.2	1.9 ±0.1
15-25 %	1.2 ±0.1	2.8 ±0.3
40-55 %	1.4 ±0.1	3.8 ±0.6
75-85 %	1.7 ±0.2	5.7 ±0.9
90 %	1.7 ±0.5	-

From Table 4.1 and Table 4.2, it can also be seen that rates of electron transfer from $CsPbBr_3$ increase with increasing amounts of CdSe, as would be expected for additive kinetics. Here, the ratio of donor to acceptor in each film was varied in an attempt to pursue characterization of the fundamental bimolecular rate constant, which describes the rate of electron transfer in the

limit of one acceptor per donor. In randomly mixed films, such a situation is difficult to orchestrate, as demonstrated by Figure 4.2; despite mixing of acceptor and donor, the two do not evenly disperse in one another. Regardless, the asymptotic limit of such behavior likely relates the bimolecular limit. The case of small fraction of CdSe in $CsPbBr_3$ can parallel the limit in which a bimolecular rate constant can be obtained; however, the situation is complicated by the fact that electron transfer is not distinctly observable for especially dilute amounts of CdSe QDs in $CsPbBr_3$ QDs.

4.4.3 Discussion

Faster rates of electron transfer in systems containing 2D materials versus their 0D counterparts can perhaps be understood by considering the later spatial extent of the 2D NPLs versus the 0D QDs. The greater NPL surface area per particle presents more opportunities for electron transfer, similar to additive kinetics of discrete electron acceptors.[60,165] Such increased spatial extent facilitates faster rates of FRET,[44] owing to the increase in the number of nearest neighbors that is afforded by the extended area of the NPL. Additionally, the 2D NPLs present a continuous density of acceptor states, whereas the 0D QD acceptors offer discretized energy levels. The continuous density of states of the NPLs offer more opportunities for electron transfer, each with a distinct free energy change. These states are then integrated over in the kinetics of electron transfer and can facilitate an increased overall rate of electron transfer relative to QD acceptors.

Given that the faster rates of charge transfer in systems containing NPLs likely arise from the extended spatial areas of the NPLs, it is probably true that the orientations of the acceptor CdSe NPLs relative to the $CsPbBr_3$ donors influence the rate of charge transfer, particularly in the case of $CsPbBr_3$ NPL donors. The fastest rate would be expected for cofacial arrangement of $CsPbBr_3$ NPLs and CdSe NPLs, such that the opportunities for electron transfer would be optimized. A

similar argument is presented in Rowland et al. for energy transfer between cofacially stacked CdSe NPLs. Future work could benefit from synthetic routes to cofacial arrangements, as well as theoretical analysis of different QD and NPL configurations, as the geometry of each particle is certain to influence the observed electron transfer rate.

In conclusion, electron transfer rates in mixed films of $CsPbBr_3$ and CdSe NPs were identified using static and time-resolved photoluminescence and transient absorption spectroscopies. Rates of electron transfer in films containing different types of $CsPbBr_3$ and CdSe NPs were extracted from trPL decays and show that electron transfer is faster for 2D materials such as NPLs than it is for 0D materials such as QDs. These findings offer potential implications in the design of solar cells or other devices in which it is critical to maximize rates of charge transfer.

4.5 Outlook

One of the more puzzling aspects of this work at the time of its publication was that no energy transfer was observed between the $CsPbBr_3$ and CdSe NCs. The prerequisite conditions for FRET were satisfied – namely, that there was spectral overlap between the donor and the acceptor – and so our expectation was that we would have to analyze rates of both charge and energy transfer. Rather than finding that both types of electronic processes were present but to varying degrees, we seemed no find no evidence of energy transfer whatsoever. The topics of charge and energy transfer, and the interplay between these electronic processes, very much remains an active field of research;[43] as a result, others have continued research in this area and provided some insight into this remaining question from our work.

Some insight into this area has been provided by Yang *et al.*, who treated the topic of energy transfer in $CsPbBr_3$ perovskite solids.[166] When they attempted to induce energy transfer in blended $CsPbBr_3$ / CdSe NC films, they found that diffusion of $CsPbBr_3$ NC excitons into CdSe only had a 4.5% likelihood of occurring. Roughly 70% of the time, $CsPbBr_3$ excitation was quenched by processes such as charge transfer instead, consistent with our results where electron transfer was dominant.

Louidice *et al.* then looked into the distance dependencies of electron vs energy transfer and provided an answer in the form of a study that used AlO_x (alumina) shells grown around $CsPbBr_3$ NCs as the means of controlling interparticle distance between $CsPbBr_3$ NCs and CdSe NPLs.[167] Like us, Louidice *et al.* saw only electron transfer between NCs covered in their native ligands. Once they capped the $CsPbBr_3$ NCs with alumina, they saw both FRET and electron transfer; as the alumina shell was grown thicker, the preference for FRET became more dominant.

One point of discussion from our original work was how the orientations of the nanoparticles relative to one another would be likely to impact the measured rates of charge transfer, particularly for the case of the NPLs. In the past few years, there has been significant progress made in the area of NPL orientation, such that future work in the area of charge transfer studies with oriented NPLs should be an active consideration. Following the initial work of Gao *et al.* in 2017 that showed that diethylene glycol with varying amounts of oleic acid added to control the hydrophobicity of the solvent system could be used to prepare face-down or edge-up NPL monolayers,[101] there have been multiple reports on how solvent systems impact the preparation of face-down or edge-up NPL monolayers.[103,168] An especially creative approach that could then be applied for the preparation of other NP layer is the ink-jet printing technique developed by Bai *et al.*,[169] which likewise relies upon appropriate solvent selection to impose

specific NPL orientation upon the substrate, but avoids having to re-submerge the substrate itself in a solvent bath after the first NP layer has been deposited.

5 Scaling of Auger Recombination Lifetimes in Two-Dimensional Nanoparticles

5.1 Introduction

Nanomaterials offer prospects in optoelectronic applications, ranging from light-emitting diodes (LEDs) and lasers to photovoltaics and sensors. As these devices are operated at progressively higher powers in an attempt to produce higher outputs, nonradiative processes begin to hinder device efficiencies.[170–172] In particular, nonradiative recombination of biexcitons, or Auger recombination, in which an electron and a hole recombine and nonradiatively transfer their energy to a third carrier, is a dominant mechanism through which LED efficiency falls off as the current is raised.[171,173,174] In nanocrystals (NCs), Auger recombination is notoriously fast because of the reduced difficulty in satisfying conservation of momentum.[175,176,57] Owing to their flat dispersion bands, linear momentum is always conserved, such that only conservation of angular momentum needs to be accomplished when undergoing Auger recombination. In contrast, in bulk semiconductors, the three carriers involved in Auger recombination must realize the difficult task

of satisfying conservation of energy and linear momentum on curved dispersion bands.[177] As a result, rates of Auger recombination in nanocrystals are orders of magnitude higher than in bulk semiconductors, leading to picosecond lifetimes[56,57] that hinder the use of quantum dots in commercial devices, despite their otherwise advantageous properties for optoelectronic applications.

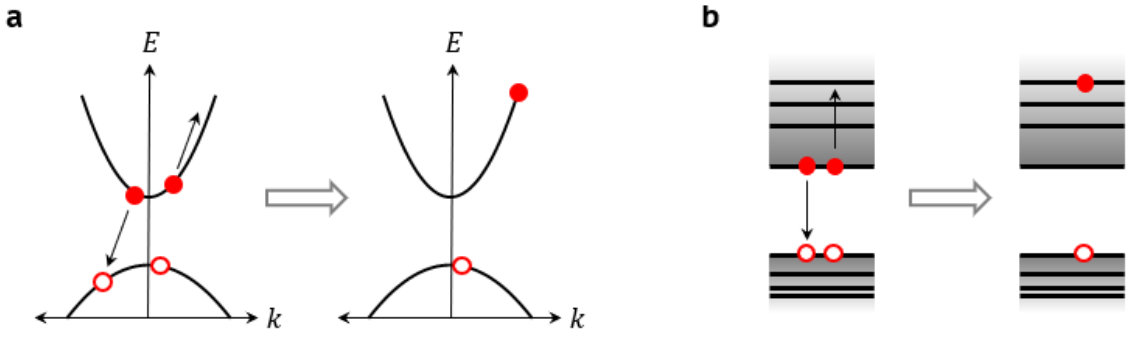

Figure 5.1. Auger recombination in **(a)** bulk semiconductors and **(b)** quantum-confined semiconductor nanocrystals. Since linear momentum is automatically conserved, rates of Auger recombination in semiconductors nanocrystals are notoriously fast.

Colloidal, two-dimensional semiconductor nanocrystals known as nanoplatelets (NPLs) offer a solution to the problem of fast rates of Auger recombination while preserving the benefits that semiconductor NCs are known for. As a result of their two-dimensional electronic structure, they feature reduced rates of Auger recombination,[54,55,58] which has led to many research efforts towards the incorporation of NPLs in LEDs and nanoscale lasers.[58,59,131] However, the mix of quantum-confined and bulk-like dimensions in NPLs along the vertical and lateral axes, respectively, makes it difficult to predict and understand their photophysical behaviors. In this chapter, we present and investigate two aspects of Auger recombination in colloidal nanoplatelet

systems: (1) the area and volume dependence and (2) the temperature dependence of Auger recombination rates.

In zero-dimensional NCs, rates of Auger recombination are understood to obey a universal scaling law, where the rates of Auger recombination in NCs scale linearly as a function of particle volume.[57,178] Essentially, faster rates of Auger recombination in smaller NCs are understood to arise from enhanced state mixing induced by quantum confinement, as well as the stronger Coulombic coupling between carriers induced by smaller nanocrystal volumes.[57] Only a few studies thus far have investigated the scaling of rates of Auger recombination in NPLs, and these initial works have led to disagreements over the dependence of rates on the NPL lateral area.[54,58] In each case, each study attempted to claim lateral area dependence (or lack thereof) with relatively few data points, making it very difficult to discern trends in the data. Here, we attempt to remedy the situation by first conducting a literature search of all reported Auger lifetimes in the literature, so that even individual measurements can be made use of; second, we conduct measurements on eight additional NPLs to further expand the data set. These measurements are analyzed in the context of a theoretical framework developed by Philbin and Rabani of UC Berkeley that argues that lateral area should play a role in determining the NPL Auger recombination rate, though a complete picture still remains elusive for NPLs of large lateral areas.[55]

In the second part of this chapter, we turn to the temperature dependence of Auger recombination in NPLs. In bulk semiconductors, the requirement that linear momentum be conserved leads to a temperature dependence in Auger recombination rates, where as the temperature is decreased, Auger lifetimes become increasingly longer as conservation of momentum becomes progressively more difficult to satisfy.[177] In zero-dimensional NCs, this is

not an issue; since the dispersion bands are flat, carriers are able to satisfy conservation of linear momentum at any temperature – though they must still conserve total angular momentum – and so Auger lifetimes are predicted by theory to be independent of temperature.‡ These requirements and their implications on Auger recombination are summarized in Figure 5.2. Given quantum confinement in one, but not all three dimensions, it is not at all clear how Auger recombination rates will be affected by temperature in two-dimensional NPLs. Here, we show that *biexciton*

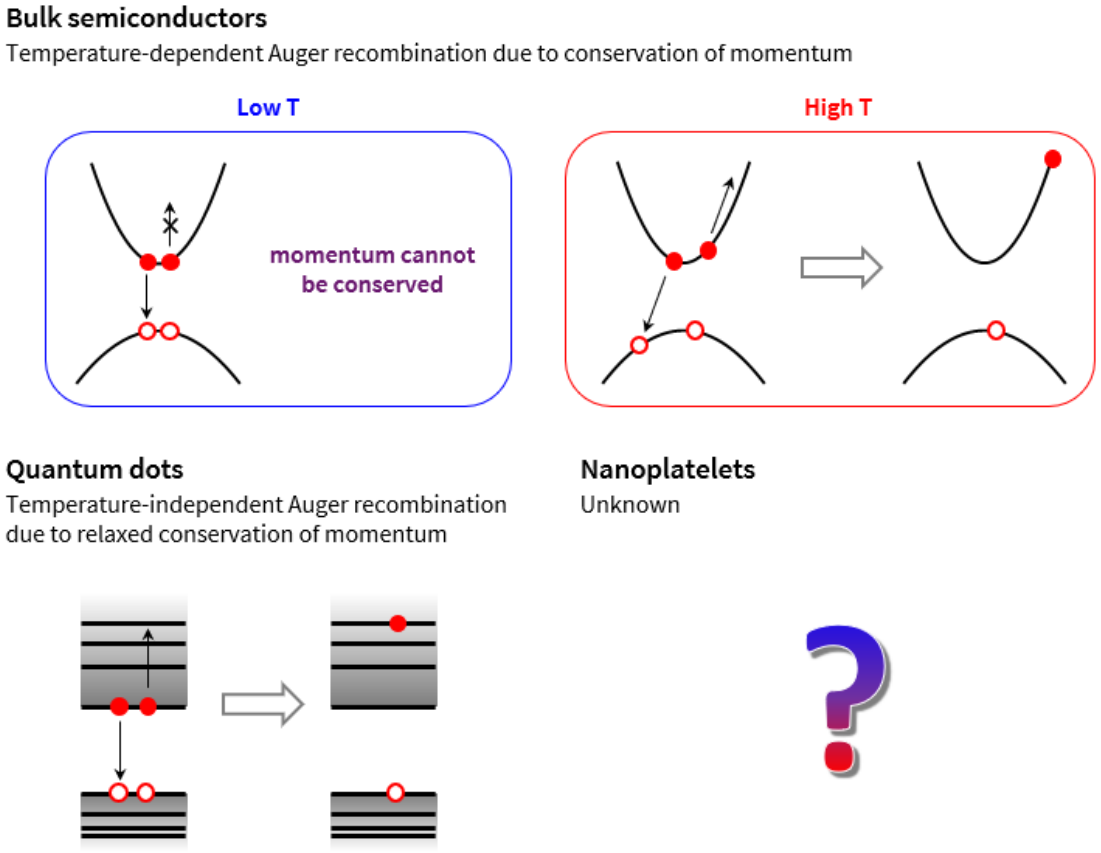

Figure 5.1. Depiction of Auger processes in bulk vs nanocrystals and the impact of temperature on their rates.

‡ Recent work by Kobayashi and Tamai has provided the first experimental investigation (to our knowledge) into the scaling of Auger rates as a function of temperature for quantum dots. Interestingly, they found that rates of Auger recombination in CdTe *do* scale as a function of temperature below 175 °C, which they attribute to a phonon-assisted mechanism.[179,180]

lifetimes are temperature-dependent in NPLs; surprisingly, however, the exhibited temperature dependence is the opposite as what is observed in bulk semiconductors, such that the biexciton recombination lifetime actually gets faster as the temperature is lowered. We show that this arises due to increased biexciton radiative recombination at low temperatures and not Auger recombination. This work emphasizes that, despite the dominance of nonradiative multiexciton recombination at room temperature in NCs, the same cannot be assumed for non-zero-dimensional NCs at other temperatures.

5.2 Experimental Methods

5.2.1 Sample Preparation

For the lateral area-dependent Auger study presented in Section 5.4.1, CdSe NPLs were dispersed in solutions of hexanes or methylcyclohexane at an optical density of roughly 0.2–0.3 at 400 nm in a 1 mm cuvette. For the temperature-dependent Auger study presented in Section 5.4.2, CdSe NPLs were dispersed in a 1:1 mixture of hexane to methylcyclohexane by volume at the same optical density. Methylcyclohexane was used to help the solution freeze as a glassy solid, and the addition of hexane was found to help prevent cloudiness. Around 100–200 μL of each solution was pipetted into the area contained by an o-ring situated on top of a sapphire plate. A second sapphire plate was then positioned over the solutions to create a make-shift sapphire cuvette for loading the samples into a variable-temperature helium cryostat.

5.2.2 Transient Absorption Spectroscopy

Transient absorption (TA) measurements were acquired by photoexciting CdSe NPLs with the 400 nm, frequency-doubled output of a 35 fs Ti:sapphire laser operating at 2 kHz. A chopper was used to reduce the frequency of the pump to 1 kHz. Sample absorption was probed using white light generated by passing 800 nm light through a sapphire plate. Scans were acquired at fluences corresponding to very low ($\langle N \rangle \ll 0.1$) to moderate ($\langle N \rangle \approx 0.2 - 0.5$) average numbers of initial excitons.

5.2.3 Time-Resolved Photoluminescence

Time-resolved photoluminescence (PL) measurements were acquired using a single-photon sensitive streak camera. CdSe NPLs were excited using the 400 nm, frequency-doubled output of a 35 fs Ti:sapphire laser operating at 2 kHz. Emission of the sample was directed through a 420 nm long pass filter on its way to the streak camera.

5.3 Data Processing

Data analysis was conducted in an analogous manner for both transient absorption (TA) and streak camera measurements. In the case of TA measurements, kinetics at the heavy hole bleach maximum (~512 nm for 4 ML NPLs and ~555 nm for 5 ML NPLs) were used for analysis, whereas in streak camera measurements the entire emission spectrum was integrated for analysis. Dynamics were normalized between 1.5 and 2.0 ns for measurements collected in a 2 ns time window, operating under the assumption that dynamics are dominated by single exciton recombination at such late times following photoexcitation. In later renditions of the measurements (particularly in

the streak camera measurements), some measurements were acquired in 5 ns time windows to be particularly certain that only single exciton recombination dynamics were present during the last ~0.5 ns of data collection. Following normalization at late time values, data collected at very low fluences ($\langle N \rangle \ll 0.1$) was differenced from data collected at higher powers to separate out biexciton-only dynamics. These biexciton dynamics were fit to a single exponential, and this process was repeated for multiple measurements at moderate fluences to yield an average Auger recombination lifetime. Error bars thus represent the standard deviation from this set of measurements.

5.4 Results and Discussion

5.4.1 Area and Volume Dependence

The area dependence of rates of Auger recombination in colloidal NPLs has only explicitly been studied in three papers—two in the case of CdSe NPLs,[54,58] and one more recently in the case of $CsPbBr_3$ NPLs.[181] In the case of CdSe NPLs, the results were contradictory, with She *et al.* reporting no lateral area dependence[58] and Li and Lian reporting a linear dependence[54] on the NPL lateral area. However, both of these works established their conclusions based off of relatively few data points; She *et al.* had only three sets of 5 ML NPLs and only two sets of 4 ML NPLs. While Li and Lian did have a more robust series of four 4 ML NPLs of varying lateral areas, for the 3 and 5 ML thick NPLs they only had two lateral areas that were nearly indistinguishable when the standard deviation from transmission electron microscopy (TEM) measurements were taken into consideration.[54]

In any case, it is clear that additional data is needed in order to ascertain the effect (or lack thereof) of NPL lateral area and volume on the Auger recombination rate in colloidal NPLs. One easy way to add more data points is to scavenge the literature for all reports of Auger lifetimes in CdSe NPLs. The results of this literature search are presented in Figure 5.3. From this review, we can see that Auger lifetimes seem to scale with NPL thickness, with thicker NPLs having generally longer Auger lifetimes than thinner NPLs.[44,54,58,182–184] As far as a dependence on lateral area goes, neither the 4 nor 5 ML data seem to immediately suggest a clear picture.

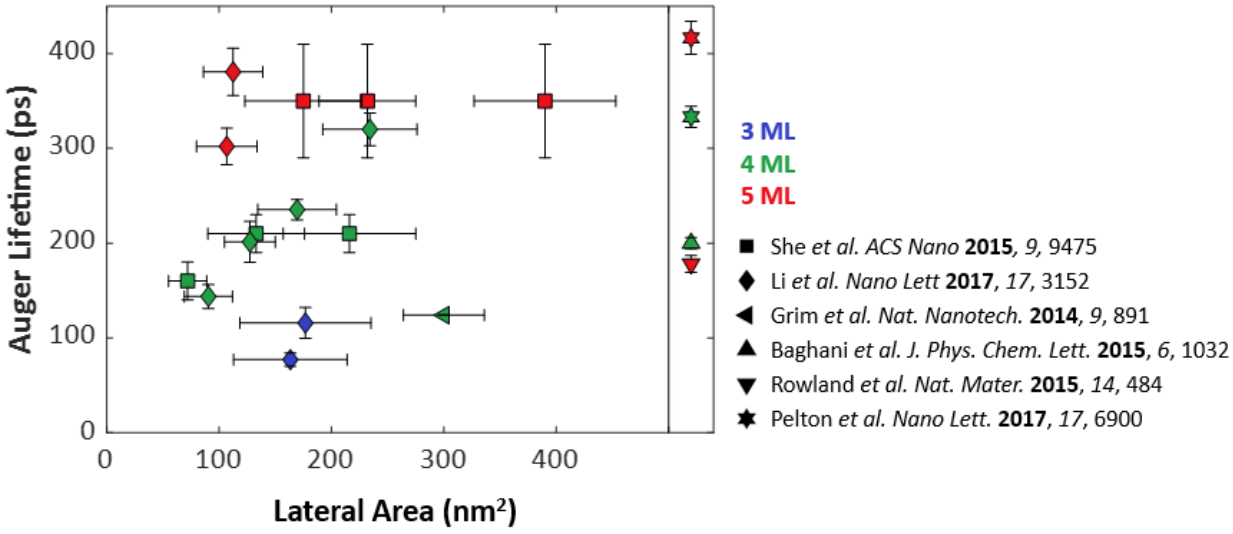

Figure 5.3. All reported Auger lifetimes for CdSe NPLs available in the literature. Points placed in the right bar correspond to NPLs with no reported lateral areas.

In an attempt to solve this conundrum, we measured Auger recombination lifetimes of eight additional 4 and 5 ML CdSe NPLs of known lateral area. These eight samples were carefully selected and treated so as to produce reliable measurements of Auger recombination lifetimes. Nanoplatelet samples with potential contaminants, identified via transient absorption spectroscopy, static photoluminescence, or transmission electron microscopy, were excluded from

analysis; as a result, from an initial set of nineteen samples, only eight were identified to be of suitable quality for further characterization. Notably, this was especially a problem when trying to obtain a sample of 5 ML NPLs of large lateral area; although Wooje Cho of the University of Chicago attempted many times to synthesize and isolate large 5 ML NPLs, he was never able to provide such a sample, thereby limiting the effective range of lateral areas that were able to be included in the study.

Figure 5.4 shows the measured Auger lifetimes of these eight samples against the other 4 and 5 ML NPLs already available in the literature. For both the 4 and the 5 ML NPLs, three of the four data points that were added follow a lateral area dependence, with the fourth measured data point falling as an outlier. Cumulatively, the data presented in Figure 5.4a is indeed suggestive of a lateral area dependence for Auger lifetimes; the data in Figure 5.4b is less persuasive, with the data reported in She *et al.* still providing a counterargument for a lateral area dependence.

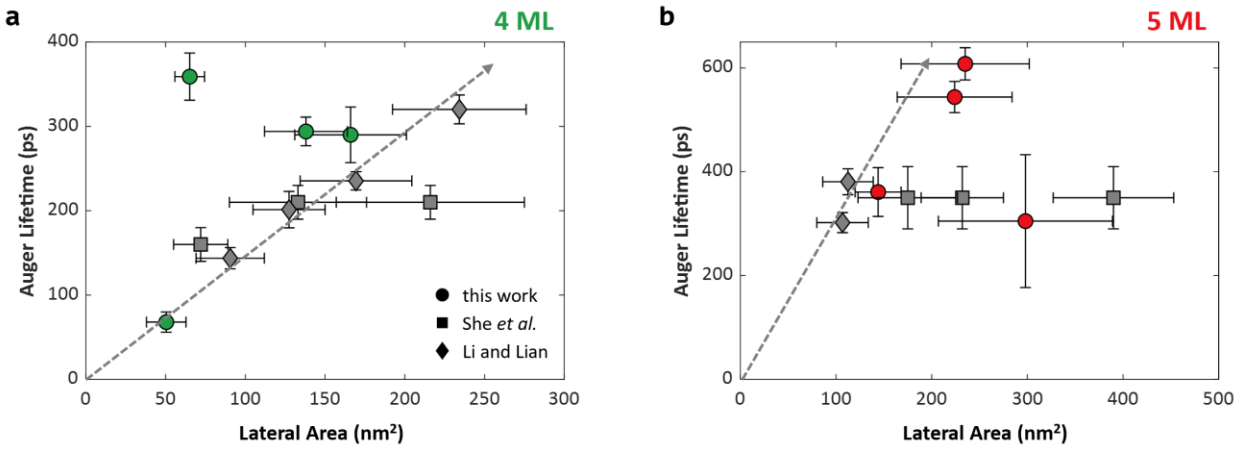

Figure 5.4. Experimentally measured Auger lifetimes for **(a)** 4 ML and **(b)** 5 ML CdSe NPLs. The gray lines are a guide to the eye representing the linear relationships presented in the work of Li and Lian.

Our investigation into the lateral area and volume dependence of Auger lifetimes in colloidal NPLs was driven in part by a collaboration with John Philbin and Eran Rabani of the University of California, Berkeley. Philbin and Rabani were motivated to revisit the approach of modeling Auger recombination in semiconductor nanocrystals via a noninteracting formalism and to instead consider an interacting formalism for the case of Auger recombination in two-dimensional nanocrystals. As shown in Figure 5.5, in a noninteracting formalism, interactions between electrons and holes are ignored. Though the noninteracting formalism has successfully been used to model strongly confined nanostructures, it does not accurately capture Auger recombination in medium or weakly confined NCs. For semiconductor nanocrystals, Philbin and Rabani have previously shown that an interacting formalism, where electrons and holes are correlated (i.e. bound as excitons), but correlations between excitons are ignored, models Auger recombination effectively in both regular and core/shell quantum dots, as well as nanorods, across the full strong-to-weak coupling regime.[185,186] Such a formalism is justified in nanocrystals, where exciton binding energies are strong but biexciton binding energies are small.

Applying the interacting formalism to semiconductor NPLs was previously limited by the computational cost of the approach, but the development of a stochastic formulation for the calculation of Auger lifetimes enabled a reduction in the computation cost that thereby allowed for the calculation of Auger lifetimes in CdSe NPLs up to 8 × 8 nm in lateral area. As such, Figure 5.6 shows the results of applying an interacting formalism (as opposed to a noninteracting formalism) to the calculation of Auger recombination lifetimes in CdSe NPLs.[55] Although both formalisms result in a lateral area dependence, only the interacting formalism matches the order of magnitude for the lifetimes we measure experimentally.

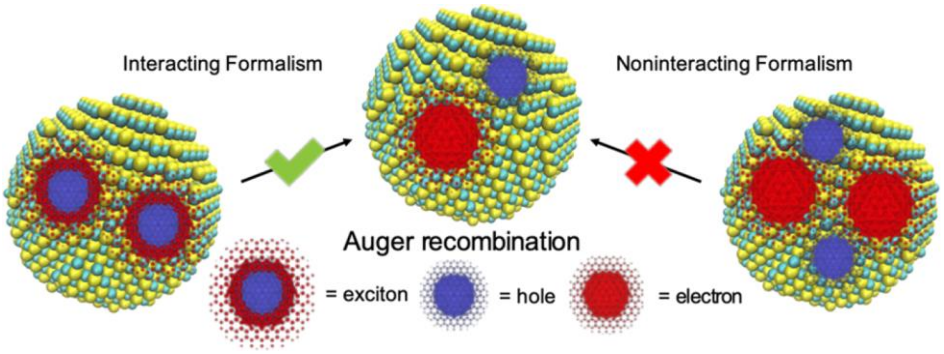

Figure 5.5. Depiction of the interacting and noninteraction formalisms of Auger recombination. In the interacting formalism, the electrons and holes are spatially correlated, but the two excitons of the biexciton are not. In the noninteracting formalism, all of the electron-hole interactions are ignored. Figure reproduced from Ref. 185.

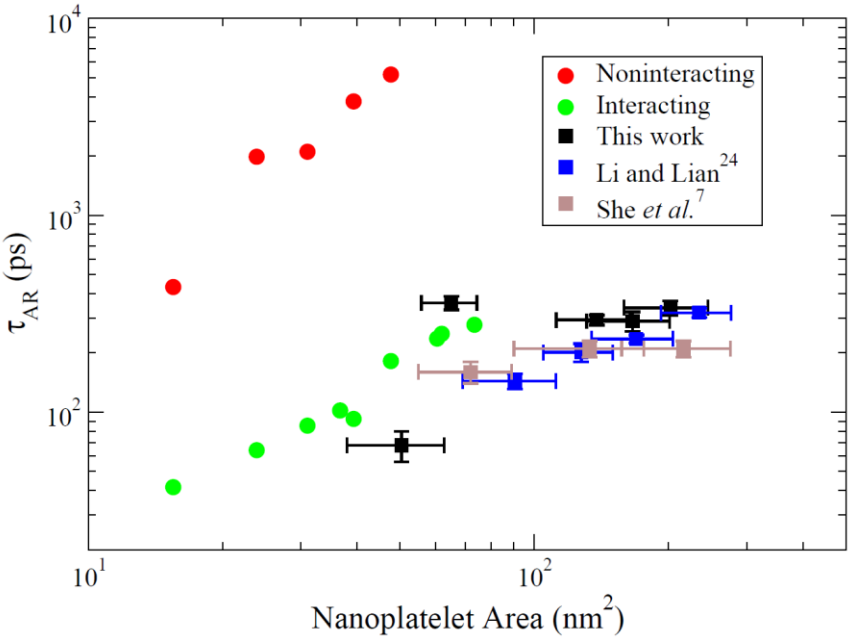

Figure 5.6. Comparison of the noninteracting and interacting formalisms to the experimental Auger lifetime data for 4 ML thick NPLs. Although both formalisms give a dependence of the Auger lifetime on NPL lateral area, the noninteracting formalism produces Auger lifetimes that are one to two orders of magnitude longer than those reported in the literature. Figure reproduced from Ref. 55.

At this point, lateral areas beyond 100 nm^2 are not accessible by theory, which is where most of the experimental data points lie. Although the theoretical data presented in Figure 5.6 clearly supports a lateral area dependence at small lateral areas, one hypothesis for the behavior past 100 nm^2 is that at some point, past the area determined by the biexciton Bohr radius, the rate for Auger recombination will reach a plateau and/or only change minimally with lateral area. Such a picture could unify the data presented in Figure 5.5a and b, where Figure 5.5a contains NPLs of "medium" lateral area while Figure 5.5b contains some NPLs of "large" lateral area. NPLs of different thicknesses do not have noticeably different exciton Bohr radii,[187] so the difference in lateral areas between Figure 5.5b and Figure 5.5a could perhaps account for the differences in behavior that are observed.

5.4.2 Temperature Dependence

The scaling of Auger recombination lifetimes with temperature in two-dimensional colloidal nanoparticles has yet to be investigated, though as mentioned in the introduction, some measurements of Auger coefficients in quantum wells have been performed in the context of evaluating quantum well systems for lasers. In this section, we present time-resolved photoluminescence (trPL) measurements of biexciton lifetimes aimed at extracting Auger lifetimes of 4 and 5 ML CdSe NPLs.

Figure 5.7a shows trPL measurements of 5 ML CdSe NPLs acquired in a 2 ns time window for a range of fluences between 0.57 and 18 $\mu J/cm^2$ at 30 K. The data is normalized past 1.5 ns, in a time range where multiexcitons are expected to have decayed and only single excitons remain. As such, single exciton dynamics dominate the decay of the sample past 1.5 ns. By normalizing the data past 1.5 ns, we emphasize the differences in the numbers of multiexcitons present at early

times. Indeed, as the excitation fluence is raised from 0.57 up to 18 μJ/cm^2, the difference in the number of excitons generated can be seen by the increasing values of $I(0)$, the intensity at $t = 0$.

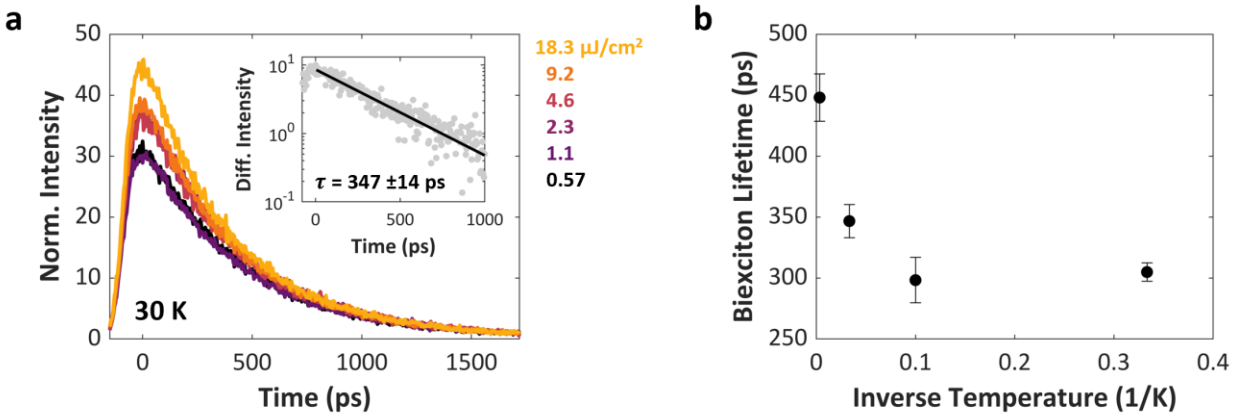

Figure 5.7. Biexciton lifetime dynamics of CdSe NPLs in a 1:1 mixture of hexanes to methylcyclohexane measured using a single photon-sensitive streak camera. **(a)** Example data for 5 ML thick NPLs at 30 K at a range of fluences. The biexciton lifetime can be determined by normalizing the photoluminescence dynamics at long time values (i.e. at 1500+ ps), past the point where multiexciton recombination is expected to have taken place, and then differencing out the single exciton dynamics from the higher power data. The result of the procedure, shown in the inset, yields monoexponential data that can be fitted to determine a biexciton lifetime. **(b)** Biexciton lifetime for 5 ML CdSe NPLs as a function of inverse temperature. As the temperature drops, the biexciton lifetime shortens.

By differencing the data collected at low powers, where any excited NPLs contain only a single exciton, from the data collected at higher powers, where the average number of excitons $\langle N \rangle$ is such that some of the excited NPLs contain biexcitons, we can isolate the biexciton dynamics. These dynamics can then be fit to an exponential function to obtain a biexciton lifetime, the result of which is shown in the inset of Figure 5.7a. Data acquired at a power of 1.1 μJ/cm^2, which exhibited the same dynamics as the data acquired at a power of 0.57 μJ/cm^2, were used for single exciton dynamics, while the data acquired at 9.2 μJ/cm^2 were used for biexciton dynamics.

The biexciton dynamics for these CdSe NPLs at temperatures of 3, 10, 30, and 295 K are displayed in Figure 5.7b. As the temperature falls, the biexciton lifetime gets shorter, decreasing from 448 ±19 ps at room temperature to 305 ±8 ps at 3 K. While this is markedly temperature dependent behavior, it is not the temperature dependent scaling of Auger lifetimes observed in bulk semiconductor systems, where Auger recombination lifetimes get longer as the temperature falls as a result of the lower probability of satisfying conservation of momentum.

The apparent increasing rate of biexciton recombination with decreasing temperature suggests that, rather than nonradiative (Auger) recombination being the dominant recombination mechanism for colloidal NPLs, radiative recombination may instead become dominant at the lower temperatures. To test this hypothesis, we conducted static PL measurements of CdSe NPLs at low temperatures (10 K) and room temperature and compared the integrated PL intensities to determine the extent to which multiexcitons decayed via radiative pathways. The result of these experiments is shown in Figure 5.8. As the excitation fluence is increased, a higher average number of excitons $\langle N \rangle$ per NPL is generated. In the single exciton regime, where $\langle N \rangle \ll 0.1$, increasing the fluence simply changes the number of NPLs that are excited with one exciton. In this regime, the graph of the integrated PL intensity vs. fluence is linear, since the number of emissive NPLs is increasing, and as an ensemble the single excitons undergo radiative recombination at the same rate (determined by the quantum yield of the sample).

As the fluence is increased further and excitation produces biexcitons in some of the NPLs, the conventional picture for NCs dictates that biexcitons overwhelmingly decay nonradiatively. In principle, the radiative biexciton lifetime can be estimated as 4× faster than the single exciton radiative recombination lifetime, owing to the 4 electron-hole recombination pathways that are

possible. A NPL with a 12 ns single exciton radiative lifetime would thus be expected to have a 3 ns biexciton radiative lifetime. Since observed biexciton recombination times at room temperature are on the order of hundreds of picoseconds (or tens of picoseconds in the case of zero-dimensional NCs, for which single exciton radiative lifetimes are even longer), it is concluded that biexciton recombination must be predominantly nonradiative.

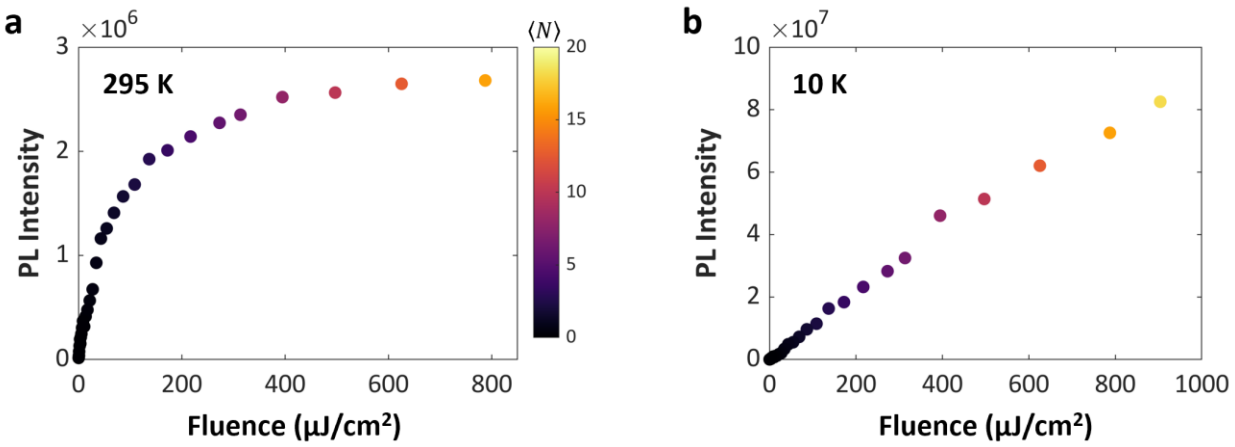

Figure 5.8. Integrated PL intensity of 5 ML CdSe NPLs at **(a)** 295 K and **(b)** 10 K as a function of 400 nm excitation fluence. CdSe NPLs were dispersed in a 1:1 mixture of hexanes to methylcyclohexane at room temperature and then frozen as a glassy solid at 10 K. **(a)** As the excitation fluence of CdSe NPLs at 295 K is increased, the integrated PL intensity saturates. This is the conventional behavior seen in quantum dots and other nanoparticles that is typically ascribed to highly efficient nonradiative recombination of multiexcitons. Color bar indicates the average number of excitons per NPL at each fluence based on an estimated absorption cross-section of $1x10^{-14}$ cm^2. **(b)** At 10 K, the integrated PL intensity increases linearly as a function of fluence, indicating that nonradiative recombination is no longer dominant but rather that multiexcitons undergo radiative recombination nearly as efficiently as single excitons.

As such, the integrated PL intensity saturates with increasing pump fluence, owing to multiexcitons predominantly undergoing nonradiative recombination and only the final single exciton likely decaying radiatively to produce emission. The data presented in Figure 5.8b for CdSe NPLs at room temperature depicts this classical picture of integrated PL intensity that

saturates as a function of fluence, although our estimate of the average number of excitons present in the sample for each fluence indicates that this saturation does not happen until much higher numbers of excitons than 2. Figure 5.8b is linear until at least $\langle N \rangle \approx 1.1$, at which point 42% of photoexcited NPLs contain at least two excitons; this suggests that biexcitons actually contain a significant radiative component, even at room temperature. This is quite different than the standard assumption that biexciton recombination is dominated by nonradiative Auger recombination in quantum-confined systems such as NPLs.

Figure 5.8b shows the integrated PL intensity as a function of fluence at 10 K. Notably, at 10 K we see a complete change in behavior in comparison to that observed at 295 K, which is typical for semiconductor NCs. Instead of the integrated PL intensity saturating as a function of fluence, the integrated PL intensity contains to rise linearly as a function of fluence up through $\langle N \rangle \approx 20$. This suggests that, at low temperatures, both biexcitons and higher order multiexcitons undergo radiative recombination with a similar frequency as single excitons. That is, at 10 K, the biexciton quantum yield is the same as the single exciton quantum yield.

An additional means of investigating the radiative nature of the biexciton is to look at the emission of CdSe NPLs in trPL as a function of temperature. Due to the biexciton binding energy, biexciton emission appears redshifted (i.e. at a lower energy) compared to single exciton emission. We can thus further discern biexciton emission by examining redder wavelengths when exciting at $\langle N \rangle > 0.2$. In Figure 5.9, we plot the emission of CdSe NPLs measured on a single-photon sensitive streak camera at 0.57 and 9.2 μJ/cm^2, integrated in time between 0 and 500 ps. The data is aligned along the higher energy edge, where single exciton emission is expected to dominate at both 0.57 and 9.2 μJ/cm^2. At 295 K (Figure 5.9a), the emission at 9.2 μJ/cm^2, where there exists a

moderate population of biexcitons (8% of the excited population, assuming a 1×10^{-14} cm^2 cross-section), is hardly different than the emission at 0.57 $\mu J/cm^2$, where only single excitons are present. This is consistent with a picture where biexcitons are predominantly nonradiative and decay via Auger recombination. However, when the temperature is lowered to 30 K (Figure 5.9b), the emission at 9.2 $\mu J/cm^2$ increases at lower energies, suggesting increasingly radiative biexcitons. This becomes especially clear at 3 K (Figure 5.9c), where aligning the emission along the high energy edge reveals that low energy emission is significantly enhanced at 9.2 $\mu J/cm^2$.

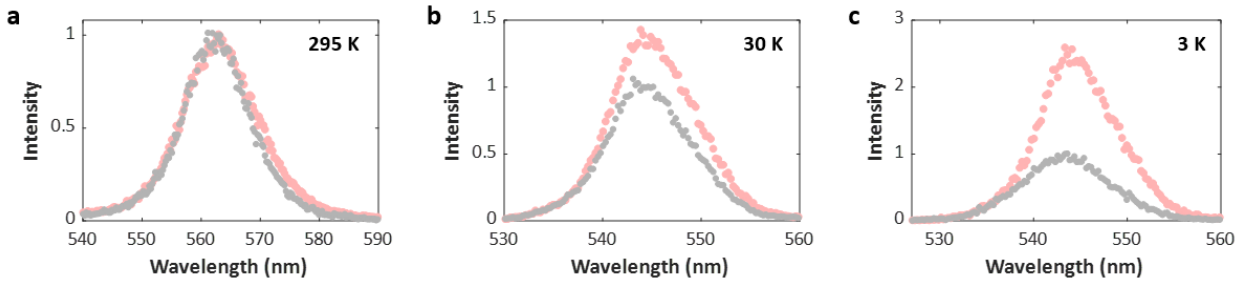

Figure 5.9. Integrated and normalized PL spectra from 0 to 500 ps at **(a)** 295 K **(b)** 30 K and **(c)** 3 K at low powers where only single excitons are formed (0.57 $\mu J/cm^2$, black dots, normalized to an intensity of 1 at the peak wavelength) and slightly higher powers where biexcitons are also present (9.2 $\mu J/cm^2$, red dots, aligned along the blue edge of the single exciton data). As the temperature is lowered, emission at redder wavelengths becomes more prominent owing to more efficient biexciton emission.

The temperature-dependent data presented in Figure 5.7b, taken together with the shorter biexciton lifetimes at lower temperatures, thus cannot be interpreted as temperature-dependent Auger rates, but should rather be treated as temperature-dependent biexciton lifetimes. To fully answer the question of whether Auger lifetimes are influenced by temperature in colloidal NPLs, the fraction of the decay that can be attributed to radiative vs nonradiative recombination needs to be determined.

One peculiar aspect of the lifetimes shown in Figure 5.7b is the fact that radiative recombination is what contributes to the anomalous temperature-dependent behavior where lifetimes *shorten* as a function of temperature. Radiative recombination typically occurs on longer timescales than nonradiative recombination, meaning that an increase in the fraction of radiative decay should lead to longer, rather than shorter, lifetimes. Fast radiative lifetimes for CdSe NPLs have been observed previously for single excitons, where decreasing the temperature caused an increase in the overall PL intensity (i.e. the overall emission, or amount of radiative recombination) yet a decrease in the observed single exciton lifetime.[11] This was explained according to a picture where the bright singlet state lies lower in energy than the dark triplet state. In such a picture, the triplet state is thermally accessible at room temperature; however, as the temperature is lowered, it becomes thermally inaccessible, such that access to the dark state is no longer common and the bright state is populated more often. As a result, emission results predominantly from the bright state, explaining the increase in overall PL intensity and the faster radiative lifetimes observed at lower temperatures. This electronic structure would likewise explain the increased biexciton emission and faster biexciton radiative lifetimes as a function of decreased temperature.

5.4.3 Conclusions

In conclusion, we have investigated scaling of rates of Auger recombination in CdSe NPLs both as a function of lateral area and temperature. Theoretical modeling of Auger recombination fully supports a linear scaling of Auger rates as a function of lateral area. Experimental data supports a linear scaling at small lateral areas but becomes less clear at large lateral areas, where the potential for a saturation in Auger rates is both theoretically defensible and experimentally observed in some studies. Measurements of biexciton lifetimes as a function of temperature

actually reveal that Auger recombination is not the only mechanism present once the temperature is lowered below 295 K; for these two-dimensional NCs, biexciton radiative recombination is not negligible at low temperatures and must be taken into account when evaluating Auger lifetimes.

6 Anisotropic Transient Disordering in Colloidal CdSe Nanoplatelets

6.1 Introduction

Two-dimensional materials, such as transition metal dichalcogenides, black phosphorus, and graphene, present remarkable properties that arise from their structures, which pair spatial extension in the lateral plane with quantum confinement in the vertical direction.[188–190] As a result, 2D semiconductors have received significant attention for atomic-scale transistors, photocatalysts, spintronics, and optoelectronics.[188,191–194] The promise of 2D colloidal nanomaterials such as nanoplatelets (NPLs) likewise stems from their spatially extended lattices, coupled with the benefits of tunable electronic bandgaps and solution processability of well-defined structures who properties do not depend on the selected substrate. The NPL bandgap can be tuned via the number of unit cells comprising the particle thickness,[11,14–16,38,39] ligand identity,[195–198] or composition, (such as the growth of a semiconductor shell or crown,[22,26,199] or compositional alloying[25,200]). As a result of quantum confinement in one dimension paired with spatially extended morphology, NPLs exhibit nearly homogeneous ensemble emission line widths,[11,12] large absorption cross sections,[8,9] and reduced rates of Auger recombination[54,58] compared to zero-dimensional

nanocrystals (NCs). Notably, these features have led to the development of high-performance light-emitting diodes (LEDs)[131,201] and nanoscale lasers with low gain thresholds.[58,59] Although these devices subject the optically active layer to high intensity excitation, the potential of such conditions to engender structural modifications in NPLs is not known.

Following photoexcitation or electrical injection, deposited energy in excess of the band gap heats the lattice through electron-phonon coupling.[202,203] Under low carriers loads, lattice heating is typically negligible; however, at high carrier injection conditions, such as those used in high current LEDs or lasers, lattice heating becomes significant enough to potentially impact structure and device performance.[67,68,204] In NCs, heat deposition is particularly consequential, as finite lattice sizes an large surface-to-volume ratios reduce thermal conductivity[205] and reduce melting points via increased surface energy.[206–208] In highly anisotropic structures such as 2D colloidal NPLs, large, flat facets appear, but the presence of higher surface energy corners and edges may confer greater susceptibility to melting.[209,210] Ultrafast electron diffraction and X-ray scattering studies of 2D materials physically grown on substrates have revealed anisotropic responses following photoexcitation with large atomic displacement and wrinkling of the layers following photoexcitation.[211–213] Because NC structure and shape dictate electronic structure, effects such as rippling of 2D materials can impact bandgap and related optoelectronic properties.[214,215]

Here, we study the response of colloidal NPL crystal structure upon optical excitation using time-resolved X-ray diffraction (TR-XRD). TR-XRD has previously been used to measure transient structural responses to ultrafast optical excitation in semiconductor NCs, revealing effects such as thermal expansion, disordering of the crystal lattice, and phase transitions.[67–69,216–218] Using

three thicknesses of CdSe NPLs, we show that intense optical excitation induces anisotropic disordering of the NPL lattice with more significant out-of-plane than in-plane disordering in 4 and 5 ML NPLs, and the opposite effect in 3 ML NPLs. Recovery dynamics in 5 ML NPLs are probed, revealing slightly faster out-of-plane than in-plane cooling, and overall slower recovery dynamics than in quasi-spherical CdSe NCs.

6.2 Experimental Methods

6.2.1 Time-Resolved X-ray Diffraction

Time-resolved X-ray diffraction (TR-XRD) experiments were conducted at Beamline 11-ID-D of the Advanced Photon Source (Argonne National Laboratory) during standard operation (24 bunch mode). As shown in Figure 6.1, NPLs were dispersed in dodecane and then flowed as a jet using a peristaltic pump. NPLs were excited in an air-free interaction region purged with N_2 using the 400 nm, frequency-doubled output of a 1.6 ps Ti:sapphire laser operating at 10 kHz. NPL structure was probed using 11.72 keV, 79 ps X-ray pulses from the APS. Powder X-ray diffraction (PXRD) patterns were collected on a time-gated Pilatus 2M detector and then azimuthally integrated. PXRD patterns were collected using 60 sec exposures, over the course of which sample was continuously flowed and replenished in the excitation region. Scans were collected and averaged until sufficient signal was acquired. PXRD patterns prior to photoexcitation were collected at least once every five scans to account for possible sample degradation in the data processing. A CeO_2 film was used as a standard for q calibration.

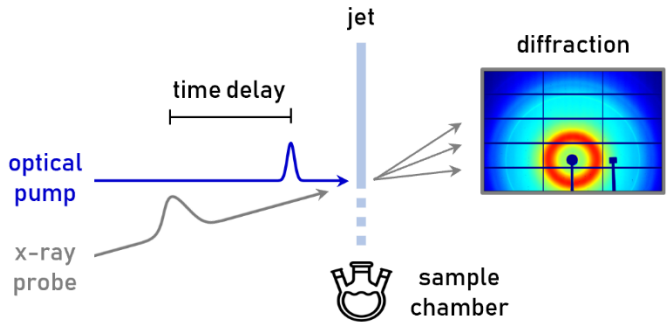

Figure 6.1. Experimental set-up of time-resolved X-ray diffraction. CdSe NPLs dispersed in dodecane are pressurized to produce a free jet. NPLs are excited by 3.1 eV, 1.6 ps laser pulses and probed using 11.7 keV, 79 ps bunched X-ray probe pulses. Powder diffraction (shown here for 3 ML NPLs) is collected on a gated area detector.

6.3 Data Processing

Powder XRD patterns were azimuthally integrated to generate 1D diffraction patterns as a function of q. Integrated powder diffraction patterns were then normalized using the average scattering intensity in the baseline region between the (200) and (220) peaks. For each diffraction pattern at a positive time delay, a diffraction pattern collected prior to photoexcitation was subtracted off to obtain a transient diffraction pattern. This was repeated for each individual scan, after which point scans at identical excitation fluences and time delays were averaged together. Additional details can be found in Refs. 67,68.

Some other important notes regarding data processing:

1. All TR-XRD patterns shown in this work present smoothed data using the `smooth` function in MATLAB R2018b with a span of 3 and the moving average method.

2. All integrals calculated in this work were done so using the `trapz` function in MATLB 2018b, which uses a trapezoidal approximation between data points to estimate the integral.

All peak fits were performed using pseudo-Voigt functions, a linear combination of Gaussian and Lorentzian functions of the form

$$S(q) = a(1-\eta)\exp\left[-\log 2\left(\frac{q-b}{c}\right)^2\right] + a\eta \cdot \frac{1}{1+\left(\frac{q-b}{c}\right)^2} \tag{6.1}$$

where a is the peak intensity, b is the peak position, c is the peak width, and η is the weighting parameter of the Gaussian and Lorentzian components.

6.3.1 Calculation of Heating-Only TR-XRD Patterns

In many of the figures in this chapter, calculated TR-XRD patterns for a situation in which only thermal expansion has occurred (that is, atomic order is still completely preserved) are presented. In such a situation, it is assumed that the static XRD peak intensity and width remain the same; however, the peak position shifts to lower q values due to lattice expansion. As such, the TR-XRD pattern of a pure peak shift can be approximated as the derivative of the static XRD pattern for small shifts in q:

$$\Delta S = S(q)_{\text{pump on}} - S(q)_{\text{pump off}} \tag{6.2}$$

$$= S(q+\Delta q) - S(q) \tag{6.3}$$

$$= \Delta q \cdot \left(\frac{S(q+\Delta q) - S(q)}{\Delta q}\right) \tag{6.4}$$

Taking the limit as $\Delta q \to 0$ (assuming that $\Delta q \neq 0$, as it does not for any data displaying a peak shift), then:

$$\lim_{\Delta q \to 0} \Delta S = \lim_{\Delta q \to 0} \left[\Delta q \cdot \left(\frac{S(q + \Delta q) - S(q)}{\Delta q} \right) \right] \tag{6.5}$$

$$= \Delta q \cdot \lim_{\Delta q \to 0} \left[\frac{S(q + \Delta q) - S(q)}{\Delta q} \right] \tag{6.6}$$

$$= \Delta q \frac{dS}{dq} \tag{6.7}$$

This means that for small peak shifts, the TR-XRD pattern lineshape is approximated by the derivative of the static peak. This methodology is often applied when analyzing absorption patterns of systems that have undergone the optical Stark effect.[219] Thus, to simulate the TR-XRD pattern for thermal expansion, the derivative of the static XRD pattern is calculated and then shifted to correspond to the observed peak shift in TR-XRD. In our case, the Δq factor is irrelevant, as we will only be comparing lineshapes after normalizing the TR-XRD patterns to a maximum value of 1.

Static diffraction patterns were collected at Sector 5 of the Advanced Photon Source. After subtracting out a polynomial baseline, the peak of interest was fit using pseudo-Voigt functions, where the (220) peak was fit to the combination of 3 pseudo-Voigt functions, corresponding to the (220), (202), and (022) components, and the (400) peak was fit to a single pseudo-Voigt function. Then, the derivative of the pseudo-Voigt fit was calculated using the `gradient` function in MATLAB R2018b and the lineshape was shifted along the x-axis to align the maximum of the positive feature of the calculated ΔS pattern with that of the experimental data.

Figure 6.2 shows the results of the above procedure for the (220) peak of 3, 4, and 5 ML NPLs at 30 °C. Results for the (400) peak are more straightforward, as the (400) peak was fit to a single pseudo-Voigt function and so the derivative does not vary in shape (refer to Figure 6.9a).

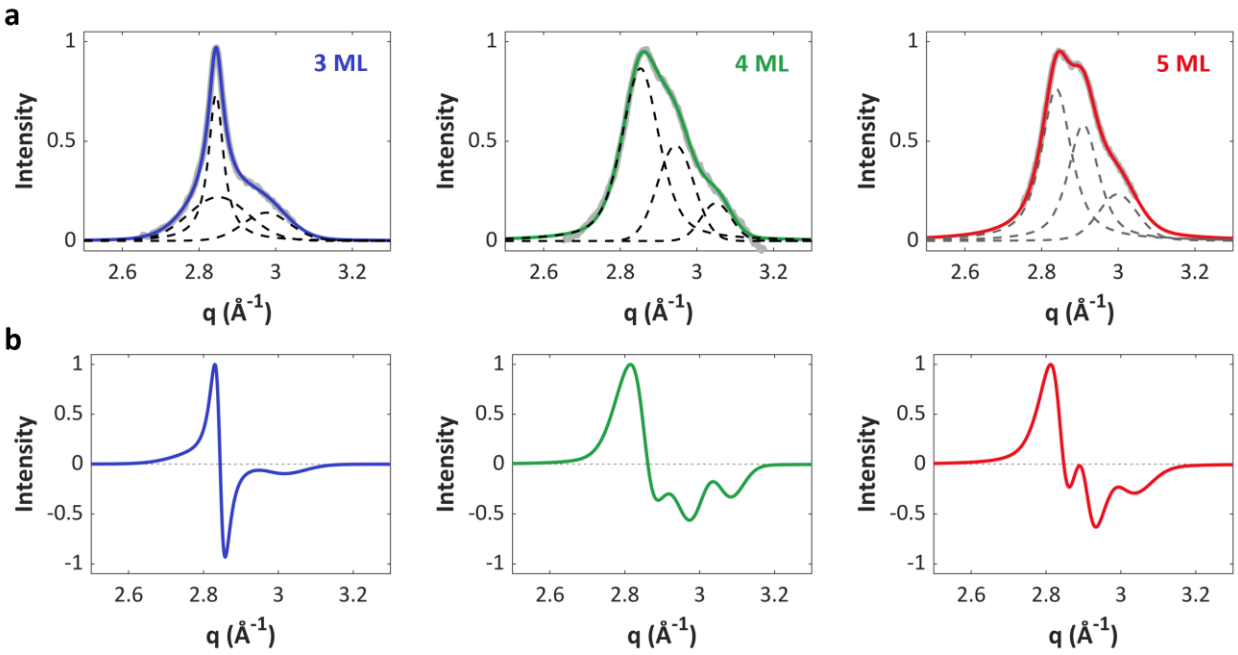

Figure 6.2. (a) Computed static XRD patterns for 3, 4, and 5 ML NPLs, focusing in on the (220) peak region, determined by fitting a region of the experimental XRD data (shown in gray) for each NPL thickness in dodecane at 30 °C. Dashed lines are fits to the (220), (202), and (022) components and solid-colored lines are the sums. **(b)** Derivatives of the computed static XRD patterns shown in (a).

6.4 Results and Discussion

CdSe NPLs of three different thicknesses, shown via transmission electron microscopy (TEM) in Figure 6.3a, were synthesized according to the procedures outlined in Chapter 1. In the thickness (or z) direction, NPLs are composed of n alternating monolayers (ML) of Cd and Se (n = 3, 4, 5) and terminated by one final layer of Cd to achieve NPLs that measure roughly 0.9, 1.2, and 1.5 nm in thickness, respectively. Lateral sizes were 37 nm × 67 nm, 7.4 nm × 23 nm, and 7.6 nm × 41

nm for these 3, 4, and 5 ML NPLs, respectively. Oleate ligands passive the Cd^{2+}-terminated surfaces.

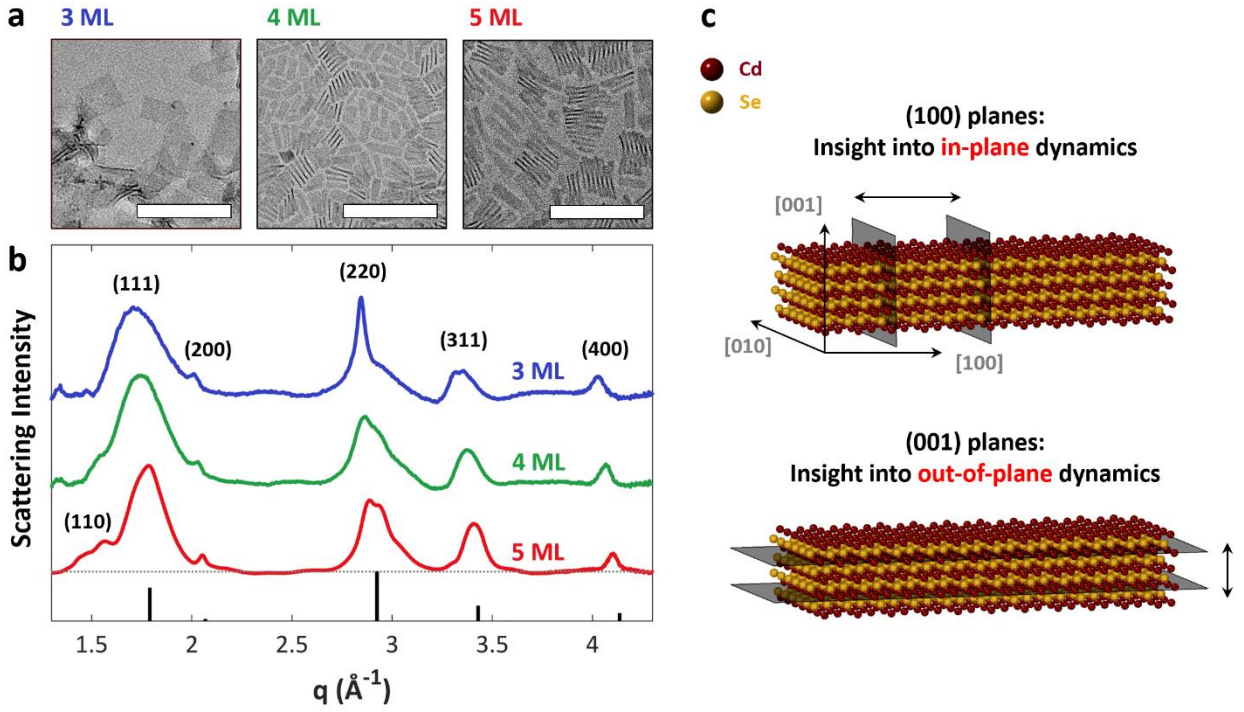

Figure 6.3. Static characterization of CdSe nanoplatelets. **(a)** Transmission electron microscopy images of 3, 4, and 5 ML CdSe NPLs. Scale bars are 100 nm. **(b)** Baseline-subtracted static X-ray diffraction patterns of 3, 4, and 5 ML CdSe NPLs dispersed in solvent (dodecane for 3 and 4 ML, heptamethylnonane for 5 ML) at 30 °C. For reference, the bulk zinc blende CdSe diffraction pattern is shown in black below the experimental data (ICSD 41528). **(c)** Schematic of a 4 ML zinc blende CdSe NPL, showing alternating layers of Cd and Se stacked along the [001] direction. In-plane dynamics can be observed by monitoring the response of the (100) planes after photoexcitation, whereas out-of-plane dynamics can be obtained from the response of the (001) planes.

Atoms pack in a tetragonally-distorted zinc blende crystal structure,[195] giving rise to the static XRD patterns shown in Figure 6.3b. Per convention, here we use (hkl) in parentheses to denote crystal planes and $[hkl]$ in hard brackets to denote crystalline axes, or directions. Tetragonal

distortion manifests in the appearance of the forbidden (110) peak and via multiple components in the (220) peak family, which arise from expansion of the lattice laterally (in the x- and y-directions) and contraction vertically (in the z-direction).[195,220,221] More distortion in thinner NPLs, along with different aspect ratios, result in distinct (220) line shapes for the different NPL thicknesses. NPL thickness increases along the [001] axis, as show in Figure 6.3c, such that the large NPL lateral surfaces are composed of (001) planes. Note that, given the cubic zinc blende crystal structure, other papers sometimes choose to define the NPL surfaces as (100) planes such that the NPL thickness increases along the [100] axis, though the definition with the (001) termination seems to be more popular. Both constructions are equivalent given the zinc blende structure, but it is important to be consistent within the framework that is chosen. Because of Scherrer broadening that arises from reduced unit cell repeats in small crystals, the sharp (400) diffraction peak arises primarily from planes that repeat along the length of the NPL in the longest

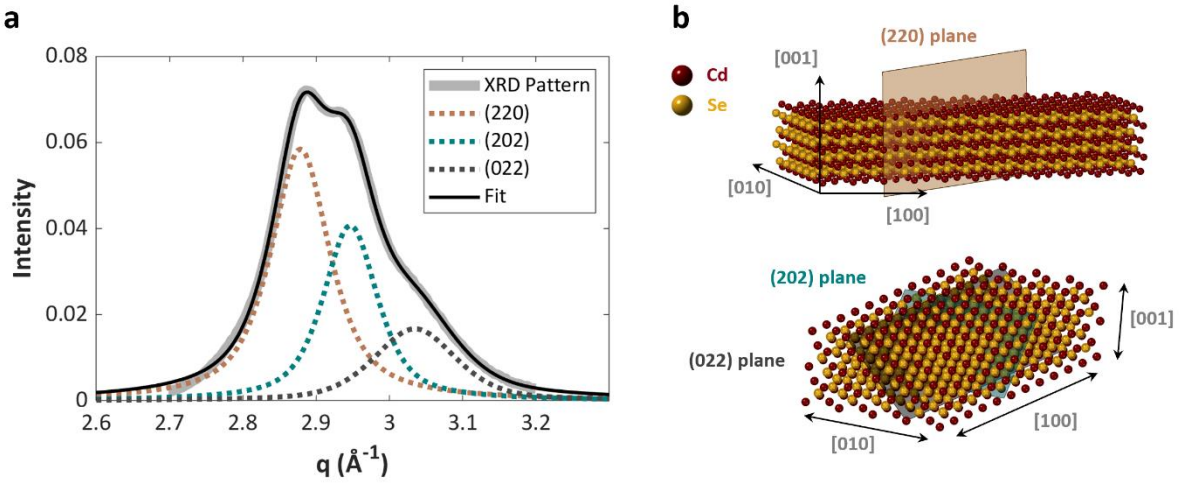

Figure 6.1. (a) Static XRD pattern of 5 ML NPLs in heptamethylnonane, focusing in on the (220) peak. The peak is fit to three pseudo-Voigt functions, corresponding to the (220), (202), and (022) planes, which are not equivalent in tetragonally-distorted CdSe NPLs. **(b)** Visualization of the (220), (202), and (022) planes in a CdSe NPL model.

direction (the [100] axis, or x-direction). Contributions from the (040) and (004) planes, repeating along the much shorter [010] and [001] axes, are likely too weak and too broad to be observed. Similarly, diffraction from (220) planes in the xy plane (parallel to the thickness, or z, direction) is sharp, compared to the convolved, broader (202) and (022) planes (see Figure 6.4). The (400) diffraction peak thus provides insight into in-plane dynamics along the lateral extent of the NPL, whereas both in-plane and out-of-plane dynamics are revealed via analysis of the (220) peak family.

6.4.1 Anisotropic Response to Photoexcitation

To investigate the impact that photoexcitation at elevated fluences imparts on NPL structure, we employed TR-XRD at Beamline 11-ID-D of the Advanced Photon Source (Argonne National Laboratory) as described in the Methods section above. The transient scattering X-ray response, ΔS, was isolated by subtracting the diffraction pattern prior to photoexcitation from that after photoexcitation.

Figure 6.5a shows TR-XRD patterns for 5 ML CdSe NPLs at 40 ps, the time delay with the strongest observed transient response. Inspection of the TR-XRD lineshape for each diffraction peak reveals the extent to which crystalline plans transient disorder after photoexcitation. Thermal expansion only, with no disordering, shifts diffraction peaks to lower q values, resulting in the TR-XRD patterns highlighted in gray. We note that temperature-dependent static X-ray diffraction measurement of 5 ML CdSe NPLs, presented in Figure 6.6, do not show the decrease in scattering intensity with q^2 as expected from Debye-Waller theory. The (400) peak deviates only minimally from this lineshape highlighted in gray, pointing to in-plane thermal expansion with minimal in-plane disordering on the timescale of this experiment. In contrast, the (220) peak family presents

more prominent negative features, signaling loss in diffraction intensity that arises from significant out-of-plane disordering, possibly consistent with buckling that decreases out-of-plane unit cell registry.

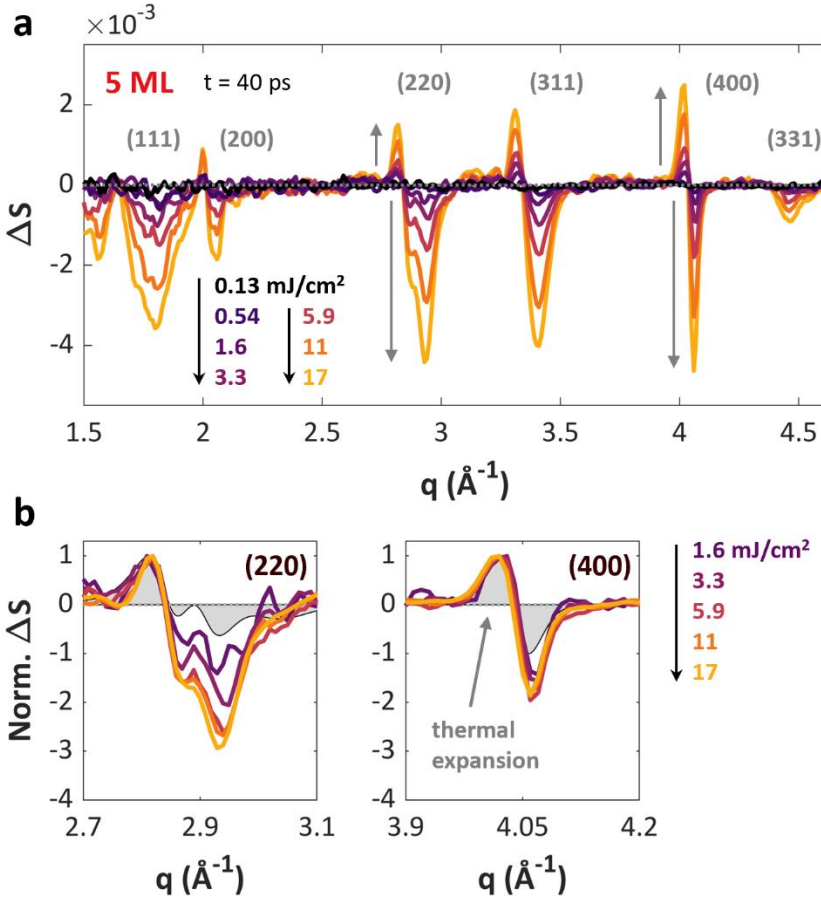

Figure 6.5. Time-resolved X-ray diffraction of 5 ML CdSe NPLs, 40 ps after photoexcitation. **(a)** TR-XRD patterns as a function of increasing fluence. **(b)** TR-XRD patterns, normalize to a maximum of 1, for the (220) and (400) peaks. The area shaded in gray represents the TR-XRD pattern that results from only a peak shift to lower q (i.e. thermal expansion). Deviations from this lineshape arise from loss in diffraction due to transient disordering.

As shown in Figure 6.5b, the excitation fluence dependence of these two peaks is also anisotropic. Although the lineshape of the (400) peak remains relatively unchanged between 1.6

and 17 mJ/cm^2, the (220) peak family progressively loses more scattering intensity. This behavior suggests fairly constant in-plane disordering with marginal fluence dependence, in contrast to the strongly fluence-dependent out-of-plane disordering. This is supported by the picture shown in Figure 6.7, which plots the fraction of disorder as a function of power for the (220) and (400) planes. The fraction of the peak area that arises from disordering is quantified as the component that cannot be attributed to the gray shaded area in Figure 6.9a arising from thermal expansion. Notably, out-of-plane disordering may lead to undesirable changes in electronic properties, such as transition linewidth, as NPL thickness dominates these characteristics.

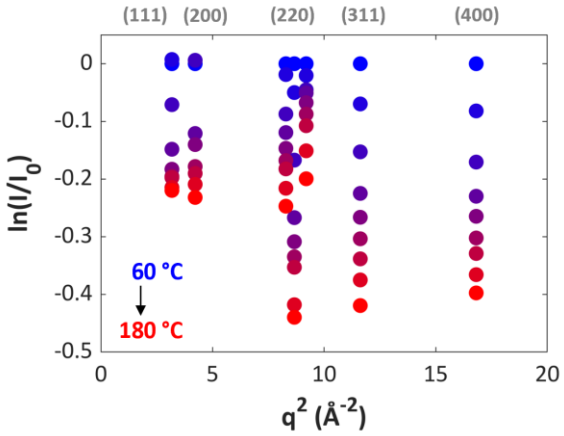

Figure 6.6. Natural log of the normalized peak intensity versus q^2, plotted every 15 °C between 60 °C and 180 °C. A linear relationship, not observed here, would be expected by Debye-Waller theory.

Such anisotropic response to photoexcitation is not present in quasi-spherical wurtzite[67] or quasi-spherical zinc blende CdSe NCs, which both display isotropic changes to the lattice, as well as substantial disordering at comparable fluences. Furthermore, the relative lack of in-plane disordering in CdSe NPLs even at elevated fluences suggests that CdSe NPLs are more robust to optical excitation than quasi-spherical CdSe NCs. The highest fluence probed here of 17 mJ/cm^2

corresponds to an average of 4 excitons/nm^3 (based on an absorption cross-section of 4 × 10^{-14} cm^2), yet NPLs retain in-plane crystallinity. This is in contrast to quasi-spherical CdSe NCs, which exhibit extensive disordering—akin to melting—at exciton densities above 1 exciton/nm^3.[67] This is likely due to the prominence of flat faces over much of the NPL surface, in comparison to the highly convex surfaces of quasi-spherical NCs.

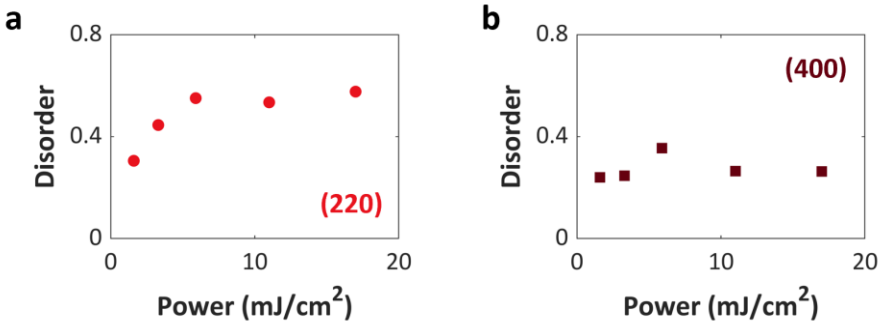

Figure 6.8. Fraction of the **(a)** (220) or **(b)** (400) peak area that stems from transient disordering for 5 ML NPLs.

6.4.2 Thickness Dependence

Figure 6.9 displays normalized TR-XRD patterns of the (220) and (400) peaks for 3, 4, and 5 ML NPLs. As the NPL thickness increases, the response of the (220) peak family changes in accordance with the differing distributions of the (220), (202), and (022) components observed in static diffraction (see Figure 6.3b). Interestingly, the 3 ML sample exhibits disordering in the (220) plane at all examined powers, possibly due to the enhanced flexibility of the thinner structures. As shown in Figure 6.8, the lowest power at which we discern changes in scattering intensity (1 mJ/cm^2) in the (220) peak family features the same extent of disordering as observed at higher studied fluences. This is markedly different than the previously observed behavior for quasi-spherical CdSe NCs,[67] where thermal expansion is the dominant response at low powers and

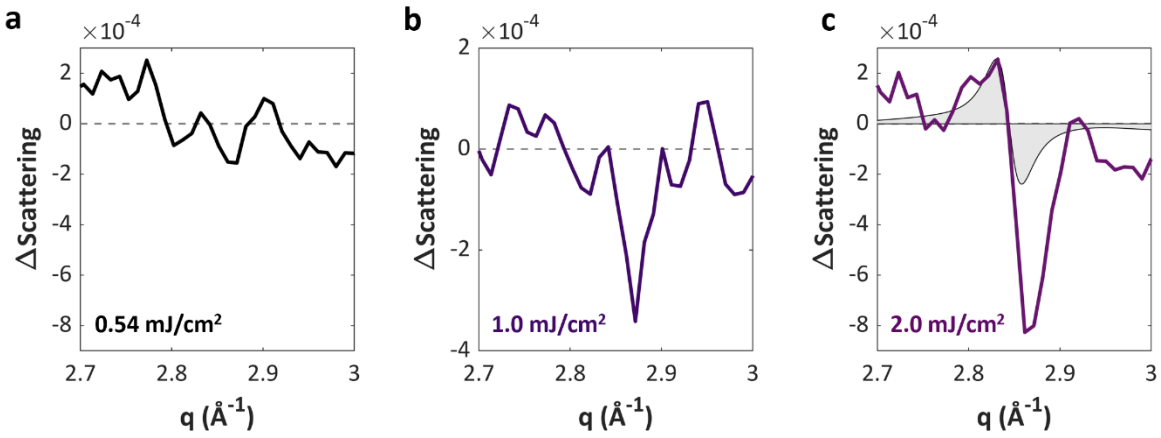

Figure 6.2. TR-XRD patterns of the (220) peak in 3 ML CdSe NPLs, 40 ps after photoexcitation at **(a)** 0.54, **(b)** 1.0, and **(c)** 2.0 mJ/cm^2. The shaded gray area in (c) is the TR-XRD pattern that results from only a peak shift to lower q (i.e. thermal expansion only, with no disordering).

disordering only arises with increasing fluence.

To quantify the extent of disordering in each plane as a function of NPL thickness, in Figure 6.9b we plot the fraction of the integrated peak area that stems from transient disordering for the (220) vs (400) peaks at ~10 mJ/cm^2, which corresponds to ~2-3 excitons/nm^3 in all three samples. The area that arises from disordering is quantified as the component that cannot be attributed to the gray shaded area in Figure 6.9a arising from thermal expansion. Consistent with the qualitative results obtained from Figure 6.5b, Figure 6.9b shows that disordering for 5 ML NPLs is anisotropic. In the (400) direction, disordering contributes to 40 ± 2% of the peak area, while disordering contributes to 53 ± 2% of the peak area in the (220) direction. 4 ML NPLs display similar trends, suggesting that thick NPLs respond to photoexcitation anisotropically with more pronounced disordering in the out-of-plane direction. On the other hand, disordering only contributes to 18 ± 1% of the (220) peak area for 3 ML NPLs, compared to 53 ± 9% for the (400) plane. Thinner NPLs thus display anisotropic disordering in an opposite manner, with stronger in-

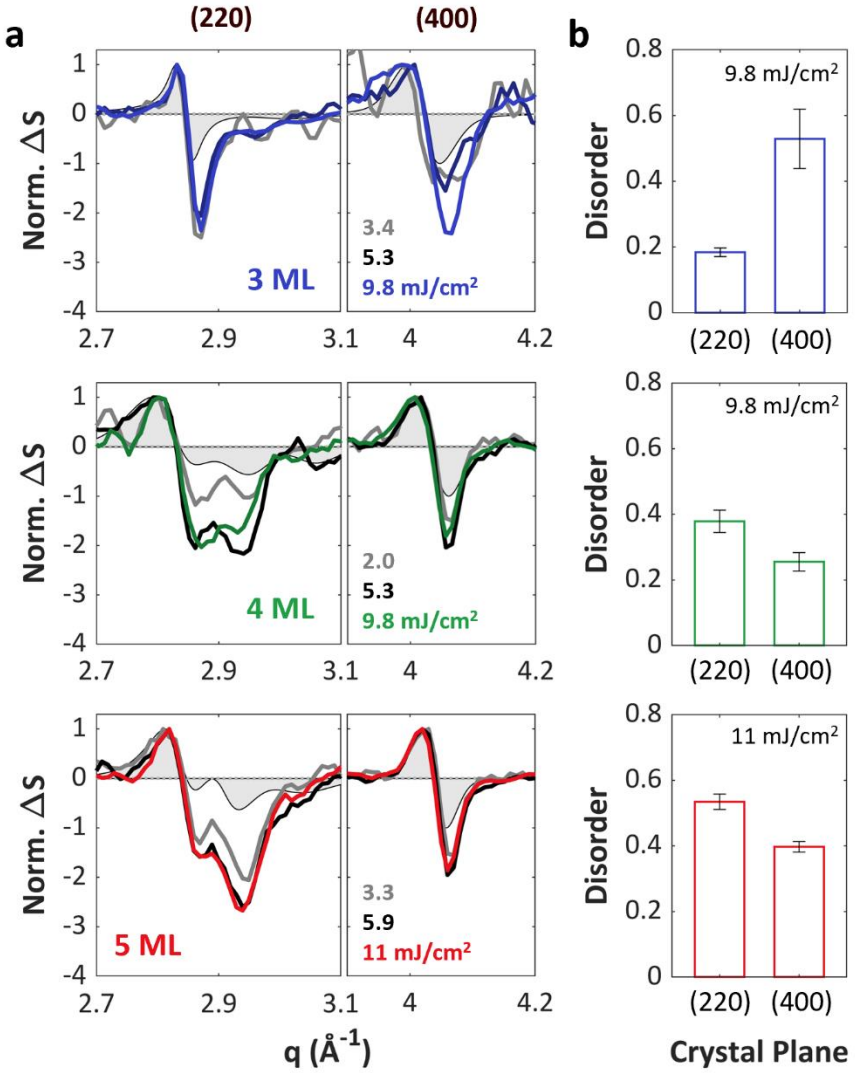

Figure 6.3. Thickness dependence of NPL thermal response. **(a)** TR-XRD patterns, normalized to a maximum of 1, of the (220) and (400) peaks 40 ps after photoexcitation for 3, 4, and 5 ML NPLs at comparable fluences. The areas shaded in gray represent the TR-XRD patterns that result from only a peak shift to lower q (i.e. thermal expansion). **(b)** Fraction of the integrated $|\Delta S|$ peak area that stems from transient disordering for the (220) vs (400) planes at ~10 mJ/cm² for each thickness.

plane disordering, perhaps because of their enhanced flexibility.

6.4.3 Recovery Dynamics

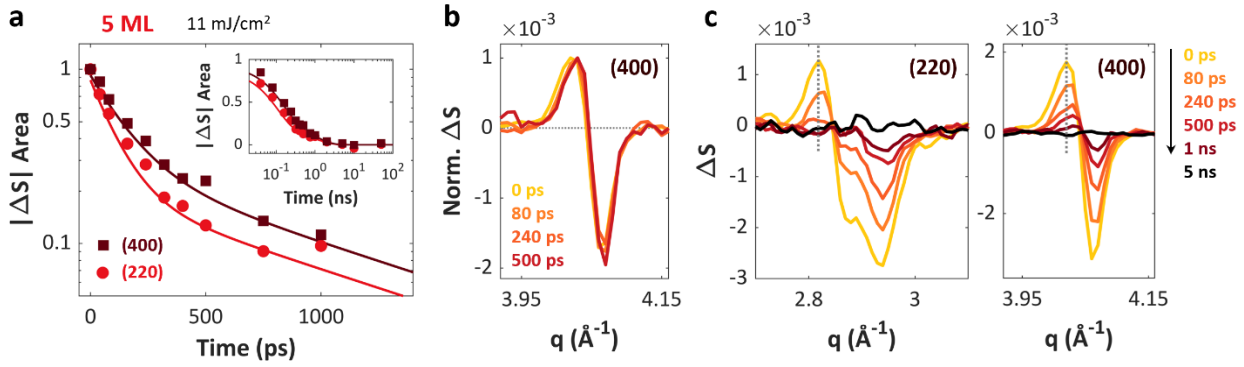

Figure 6.10. Cooling and recrystallization dynamics of 5 ML CdSe NPLs. **(a)** Recovery dynamics in 5 ML NPLs after 400 nm excitation at 11 mJ/cm², determined by integrating $|\Delta S|$ for each peak. For each curve, dynamics are normalized to 1. Solid lines are biexponential fits to the data. Inset shows fit to longer time delays. **(b)** TR-XRD of the (400) peak at four different time points early in the recovery process, normalized to a maximum value of 1. No change in lineshape is apparent. **(c)** TR-XRD patterns of the (220) and (400) peaks up to 5 ns after photoexcitation.

Recovery dynamics of the 5 ML diffraction peaks, generated by integrating the absolute value of the change in scattering intensity at each diffraction peak as a function of delay time, are plotted in Figure 6.10a. Analysis of recovery dynamics yields information regarding the time scales of both cooling (the reversal of thermal expansion) and recrystallization (the reversal of disordering). Indeed, as shown in Figure 6.10a, recovery appears biexponential with τ_1 requiring about 100 ps and τ_2 occurring on a nanosecond timescale. Though admittedly not outside error bars, a slight difference in fitted τ_1 values appears to exist, as the (220) peak family recovers with τ_1 = 107 ± 29 ps while the (400) peak recovers with τ_1 = 147 ± 42 ps. Since the (220) peak family dynamics probe both in-plane and out-of-plane recovery, these lifetimes point to potentially anisotropic recovery dynamics, with faster out-of-plane cooling. This can perhaps be attributed to shorter distances and more rapid surface scattering in the out-of-plane direction compared to the

in-plane direction. The second, slower recovery component of $\tau_2 \approx 1$ ns is attributed to slower dissipation at the surface/ligand interface. Notably, complete recovery in CdSe NPLs is much slower than that of quasi-spherical CdSe NCs, where the latter cool and recrystallize within a few hundred picoseconds.[67]

TR-XRD lineshape during recovery aids assignment of the two lifetimes to cooling versus recrystallization. Figure 6.10b displays normalized transient diffraction patterns for the 5 ML (400) peak following photoexcitation, whereas Figure 6.10c displays unnormalized transient diffraction patterns for both the (220) and (400) peaks. Over the first 500 ps following photoexcitation, the degree of disordering (i.e. the peak lineshape) in the (400) peak displayed in Figure 6.10b remains unchanged, suggesting that any recrystallization thus far is minor. Instead, the disappearance of the (220) peak positive component and the shift of the (400) peak to progressively higher q values in Figure 6.10c indicate that the fast component of the recovery dynamics corresponds to cooling. Recrystallization occurs over nanoseconds, as evidenced by the loss of diffraction intensity due to disordering remaining past 1 ns.

6.4.4 Conclusions

In conclusion, we have shown that CdSe NPL lattices respond anisotropically to controlled fluence optical excitation. Following excitation, the crystal lattice undergoes both thermal expansion and disordering, but to differing degrees along different axes. Out-of-plane disordering is more significant than in-plane disordering for 4 and 5 ML NPLs, while the opposite holds true for thinner 3 ML NPLs. These findings offer significant implications for optoelectronic devices, where the ability to operate at high excitation densities without loss of tailored properties is advantageous. In particular, out-of-plane disordering in NPLs could lead to changes in the

bandgap, resulting in lower color gamut in LEDs or detrimental transition line broadening effects in lasing.[222] Together, these results suggest that both NC composition and structure influence crystal lattice stability and resulting optical performance.

6.5 Outlook

When considering the structural and thermal response of colloidal nanocrystals to photoexcitation, it is important to consider the environment that the nanoparticles are in. In these experiments, CdSe NPLs were dispersed in dodecane, such that heat transfer took place across multiple interfaces: between the inorganic semiconductor and the organic ligand, and between the organic ligand and the dodecane solvent. The role of the ligand and how it affects rates of heat transfer has only thus far been investigated via TR-XRD for $CuInSe_2$ NCs with oleylamine versus sulfide ligands; the results showed that the use of an organic versus inorganic ligand had significant effects on the recovery dynamics following photoexcitation.[69] The role of the solvent in these TR-XRD experiments has yet to be investigated at all; all of our experiments have been conducted in dodecane, as it is a sufficiently high boiling point solvent that we are able to circulate the nanocrystals as a jet for hours without appreciable loss of solution.

References

(1) Murray, C. B.; Norris, D. J.; Bawendi, M. G. Synthesis and Characterization of Nearly Monodisperse CdE (E = Sulfur, Selenium, Tellurium) Semiconductor Nanocrystallites. *J. Am. Chem. Soc.* **1993**, *115* (19), 8706–8715.

(2) Ekimov, A. I.; Onushchenko, A. A. Quantum Size Effect in Three-Dimensional Microscopic Semiconductor Crystals. *Pisma Zh Eksp Teor Fiz* **1981**, *34* (6), 363–366.

(3) Brus, L. Zero-Dimensional "Excitons" in Semiconductor Clusters. *IEEE J. Quantum Electron.* **1986**, *22* (9), 1909–1914.

(4) Efros, A. L.; Brus, L. E. Nanocrystal Quantum Dots: From Discovery to Modern Development. *ACS Nano* **2021**, *15* (4), 6192–6210.

(5) Pietryga, J. M.; Park, Y.-S.; Lim, J.; Fidler, A. F.; Bae, W. K.; Brovelli, S.; Klimov, V. I. Spectroscopic and Device Aspects of Nanocrystal Quantum Dots. *Chem. Rev.* **2016**, *116* (18), 10513–10622.

(6) Talapin, D. V.; Shevchenko, E. V. Introduction: Nanoparticle Chemistry. *Chem. Rev.* **2016**, *116* (18), 10343–10345.

(7) Zhang, Z.; Sun, H. Manipulation of the Optical Properties of Colloidal 2D CdSe Nanoplatelets. *Adv. Photonics Res.* **2021**, 2100045.

(8) Yeltik, A.; Delikanli, S.; Olutas, M.; Kelestemur, Y.; Guzelturk, B.; Demir, H. V. Experimental Determination of the Absorption Cross-Section and Molar Extinction Coefficient of Colloidal CdSe Nanoplatelets. *J. Phys. Chem. C* **2015**, *119* (47), 26768–26775.

(9) Achtstein, A. W.; Antanovich, A.; Prudnikau, A.; Scott, R.; Woggon, U.; Artemyev, M. Linear Absorption in CdSe Nanoplates: Thickness and Lateral Size Dependency of the Intrinsic Absorption. *J. Phys. Chem. C* **2015**, *119* (34), 20156–20161.

(10) Zhang, Z.; Thung, Y. T.; Chen, X.; Wang, L.; Fan, W.; Ding, L.; Sun, H. Study of Complex Optical Constants of Neat Cadmium Selenide Nanoplatelets Thin Films by Spectroscopic Ellipsometry. *J. Phys. Chem. Lett.* **2021**, *12* (1), 191–198.

(11) Ithurria, S.; Tessier, M. D.; Mahler, B.; Lobo, R. P. S. M.; Dubertret, B.; Efros, Al. L. Colloidal Nanoplatelets with Two-Dimensional Electronic Structure. *Nat. Mater.* **2011**, *10* (12), 936–941.

(12) Tessier, M. D.; Javaux, C.; Maksimovic, I.; Loriette, V.; Dubertret, B. Spectroscopy of Single CdSe Nanoplatelets. *ACS Nano* **2012**, *6* (8), 6751–6758.

(13) van der Bok, J. C.; Dekker, D. M.; Peerlings, M. L. J.; Salzmann, B. B. V.; Meijerink, A. Luminescence Line Broadening of CdSe Nanoplatelets and Quantum Dots for Application in w-LEDs. *J. Phys. Chem. C* **2020**, *124* (22), 12153–12160.

(14) Cho, W.; Kim, S.; Coropceanu, I.; Srivastava, V.; Diroll, B. T.; Hazarika, A.; Fedin, I.; Galli, G.; Schaller, R. D.; Talapin, D. V. Direct Synthesis of Six-Monolayer (1.9 nm) Thick Zinc-Blende CdSe Nanoplatelets Emitting at 585 nm. *Chem. Mater.* **2018**, *30* (20), 6957–6960.

(15) Christodoulou, S.; Climente, J. I.; Planelles, J.; Brescia, R.; Prato, M.; Martín-García, B.; Khan, A. H.; Moreels, I. Chloride-Induced Thickness Control in CdSe Nanoplatelets. *Nano Lett.* **2018**, *18* (10), 6248–6254.

(16) Delikanli, S.; Yu, G.; Yeltik, A.; Bose, S.; Erdem, T.; Yu, J.; Erdem, O.; Sharma, M.; Sharma, V. K.; Quliyeva, U.; Shendre, S.; Dang, C.; Zhang, D. H.; Sum, T. C.; Fan, W.; Demir, H. V. Ultrathin Highly Luminescent Two-Monolayer Colloidal CdSe Nanoplatelets. *Adv. Funct. Mater.* **2019**, *29* (35), 1901028.

(17) Kurtina, D. A.; Garshev, A. V.; Vasilieva, I. S.; Shubin, V. V.; Gaskov, A. M.; Vasiliev, R. B. Atomically Thin Population of Colloidal CdSe Nanoplatelets: Growth of Rolled-up Nanosheets and Strong Circular Dichroism Induced by Ligand Exchange. *Chem. Mater.* **2019**, *31* (23), 9652–9663.

(18) Reichhelm, A.; Hübner, R.; Damm, C.; Nielsch, K.; Eychmüller, A. Increasing the Diversity and Understanding of Semiconductor Nanoplatelets by Colloidal Atomic Layer Deposition. *Phys. Status Solidi RRL – Rapid Res. Lett.* **2020**, *14* (9), 2000282.

(19) Di Giacomo, A.; Rodà, C.; Khan, A. H.; Moreels, I. Colloidal Synthesis of Laterally Confined Blue-Emitting 3.5 Monolayer CdSe Nanoplatelets. *Chem. Mater.* **2020**, *32* (21), 9260–9267.

(20) Meerbach, C.; Wu, C.; Erwin, S. C.; Dang, Z.; Prudnikau, A.; Lesnyak, V. Halide-Assisted Synthesis of Cadmium Chalcogenide Nanoplatelets. *Chem. Mater.* **2020**, *32* (1), 566–574.

(21) Moghaddam, N.; Dabard, C.; Dufour, M.; Po, H.; Xu, X.; Pons, T.; Lhuillier, E.; Ithurria, S. Surface Modification of CdE (E: S, Se, and Te) Nanoplatelets to Reach Thicker Nanoplatelets and Homostructures with Confinement-Induced Intraparticle Type I Energy Level Alignment. *J. Am. Chem. Soc.* **2021**, *143* (4), 1863–1872.

(22) Mahler, B.; Nadal, B.; Bouet, C.; Patriarche, G.; Dubertret, B. Core/Shell Colloidal Semiconductor Nanoplatelets. *J. Am. Chem. Soc.* **2012**, *134* (45), 18591–18598.

(23) Tessier, M. D.; Spinicelli, P.; Dupont, D.; Patriarche, G.; Ithurria, S.; Dubertret, B. Efficient Exciton Concentrators Built from Colloidal Core/Crown CdSe/CdS Semiconductor Nanoplatelets. *Nano Lett.* **2014**, *14* (1), 207–213.

(24) Yadav, S.; Singh, A.; Sapra, S. Long-Lived Emission in Type-II CdS/ZnSe Core/Crown Nanoplatelet Heterostructures. *J. Phys. Chem. C* **2017**, *121* (48), 27241–27246.

(25) Kelestemur, Y.; Dede, D.; Gungor, K.; Usanmaz, C. F.; Erdem, O.; Demir, H. V. Alloyed Heterostructures of $CdSe_xS_{1-x}$ Nanoplatelets with Highly Tunable Optical Gain Performance. *Chem. Mater.* **2017**, *29* (11), 4857–4865.

(26) Ithurria, S.; Talapin, D. V. Colloidal Atomic Layer Deposition (c-ALD) Using Self-Limiting Reactions at Nanocrystal Surface Coupled to Phase Transfer between Polar and Nonpolar Media. *J. Am. Chem. Soc.* **2012**, *134* (45), 18585–18590.

(27) Chu, A.; Livache, C.; Ithurria, S.; Lhuillier, E. Electronic Structure Robustness and Design Rules for 2D Colloidal Heterostructures. *J. Appl. Phys.* **2018**, *123* (3), 035701.

(28) Bouet, C.; Laufer, D.; Mahler, B.; Nadal, B.; Heuclin, H.; Pedetti, S.; Patriarche, G.; Dubertret, B. Synthesis of Zinc and Lead Chalcogenide Core and Core/Shell Nanoplatelets Using Sequential Cation Exchange Reactions. *Chem. Mater.* **2014**, *26* (9), 3002–3008.

(29) Izquierdo, E.; Robin, A.; Keuleyan, S.; Lequeux, N.; Lhuillier, E.; Ithurria, S. Strongly Confined HgTe 2D Nanoplatelets as Narrow Near-Infrared Emitters. *J. Am. Chem. Soc.* **2016**, *138* (33), 10496–10501.

(30) Akkerman, Q. A.; Martín-García, B.; Buha, J.; Almeida, G.; Toso, S.; Marras, S.; Bonaccorso, F.; Petralanda, U.; Infante, I.; Manna, L. Ultrathin Orthorhombic PbS Nanosheets. *Chem. Mater.* **2019**, *31* (19), 8145–8153.

(31) Koh, W.; Dandu, N. K.; Fidler, A. F.; Klimov, V. I.; Pietryga, J. M.; Kilina, S. V. Thickness-Controlled Quasi-Two-Dimensional Colloidal PbSe Nanoplatelets. *J. Am. Chem. Soc.* **2017**, *139* (6), 2152–2155.

(32) Galle, T.; Samadi Khoshkhoo, M.; Martin-Garcia, B.; Meerbach, C.; Sayevich, V.; Koitzsch, A.; Lesnyak, V.; Eychmüller, A. Colloidal PbSe Nanoplatelets of Varied Thickness with Tunable Optical Properties. *Chem. Mater.* **2019**, *31* (10), 3803–3811.

(33) Galle, T.; Spittel, D.; Weiß, N.; Shamraienko, V.; Decker, H.; Georgi, M.; Hübner, R.; Metzkow, N.; Steinbach, C.; Schwarz, D.; Lesnyak, V.; Eychmüller, A. Simultaneous Ligand and Cation Exchange of Colloidal CdSe Nanoplatelets toward PbSe Nanoplatelets for Application in Photodetectors. *J. Phys. Chem. Lett.* **2021**, *12* (21), 5214–5220.

(34) Sichert, J. A.; Tong, Y.; Mutz, N.; Vollmer, M.; Fischer, S.; Milowska, K. Z.; García Cortadella, R.; Nickel, B.; Cardenas-Daw, C.; Stolarczyk, J. K.; Urban, A. S.; Feldmann, J. Quantum Size Effect in Organometal Halide Perovskite Nanoplatelets. *Nano Lett.* **2015**, *15* (10), 6521–6527.

(35) Weidman, M. C.; Seitz, M.; Stranks, S. D.; Tisdale, W. A. Highly Tunable Colloidal Perovskite Nanoplatelets through Variable Cation, Metal, and Halide Composition. *ACS Nano* **2016**, *10* (8), 7830–7839.

(36) Weidman, M. C.; Goodman, A. J.; Tisdale, W. A. Colloidal Halide Perovskite Nanoplatelets: An Exciting New Class of Semiconductor Nanomaterials. *Chem. Mater.* **2017**, *29* (12), 5019–5030.

(37) Bekenstein, Y.; Koscher, B. A.; Eaton, S. W.; Yang, P.; Alivisatos, A. P. Highly Luminescent Colloidal Nanoplates of Perovskite Cesium Lead Halide and Their Oriented Assemblies. *J. Am. Chem. Soc.* **2015**, *137* (51), 16008–16011.

(38) Akkerman, Q. A.; Motti, S. G.; Srimath Kandada, A. R.; Mosconi, E.; D'Innocenzo, V.; Bertoni, G.; Marras, S.; Kamino, B. A.; Miranda, L.; De Angelis, F.; Petrozza, A.; Prato, M.; Manna, L. Solution Synthesis Approach to Colloidal Cesium Lead Halide Perovskite Nanoplatelets with Monolayer-Level Thickness Control. *J. Am. Chem. Soc.* **2016**, *138* (3), 1010–1016.

(39) Bohn, B. J.; Tong, Y.; Gramlich, M.; Lai, M. L.; Döblinger, M.; Wang, K.; Hoye, R. L. Z.; Müller-Buschbaum, P.; Stranks, S. D.; Urban, A. S.; Polavarapu, L.; Feldmann, J. Boosting

Tunable Blue Luminescence of Halide Perovskite Nanoplatelets through Postsynthetic Surface Trap Repair. *Nano Lett.* **2018**, *18* (8), 5231–5238.

(40) Porotnikov, D.; Zamkov, M. Progress and Prospects of Solution-Processed Two-Dimensional Semiconductor Nanocrystals. *J. Phys. Chem. C* **2020**, *124* (40), 21895–21908.

(41) Scott, R.; Heckmann, J.; Prudnikau, A. V.; Antanovich, A.; Mikhailov, A.; Owschimikow, N.; Artemyev, M.; Climente, J. I.; Woggon, U.; Grosse, N. B.; Achtstein, A. W. Directed Emission of CdSe Nanoplatelets Originating from Strongly Anisotropic 2D Electronic Structure. *Nat. Nanotechnol.* **2017**, *12* (12), 1155–1160.

(42) Guzelturk, B.; Demir, H. V. Near-Field Energy Transfer Using Nanoemitters For Optoelectronics. *Adv. Funct. Mater.* **2016**, *26* (45), 8158–8177.

(43) Irgen-Gioro, S.; Yang, M.; Padgaonkar, S.; Chang, W. J.; Zhang, Z.; Nagasing, B.; Jiang, Y.; Weiss, E. A. Charge and Energy Transfer in the Context of Colloidal Nanocrystals. *Chem. Phys. Rev.* **2020**, *1* (1), 011305.

(44) Rowland, C. E.; Fedin, I.; Zhang, H.; Gray, S. K.; Govorov, A. O.; Talapin, D. V.; Schaller, R. D. Picosecond Energy Transfer and Multiexciton Transfer Outpaces Auger Recombination in Binary CdSe Nanoplatelet Solids. *Nat. Mater.* **2015**, *14* (5), 484–489.

(45) Guzelturk, B.; Olutas, M.; Delikanli, S.; Kelestemur, Y.; Erdem, O.; Demir, H. V. Nonradiative Energy Transfer in Colloidal CdSe Nanoplatelet Films. *Nanoscale* **2015**, *7* (6), 2545–2551.

(46) Singldinger, A.; Gramlich, M.; Gruber, C.; Lampe, C.; Urban, A. S. Nonradiative Energy Transfer between Thickness-Controlled Halide Perovskite Nanoplatelets. *ACS Energy Lett.* **2020**, *5* (5), 1380–1385.

(47) Taghipour, N.; Hernandez Martinez, P. L.; Ozden, A.; Olutas, M.; Dede, D.; Gungor, K.; Erdem, O.; Perkgoz, N. K.; Demir, H. V. Near-Unity Efficiency Energy Transfer from

Colloidal Semiconductor Quantum Wells of CdSe/CdS Nanoplatelets to a Monolayer of MoS_2. *ACS Nano* **2018**, *12* (8), 8547–8554.

(48) Guzelturk, B.; Erdem, O.; Olutas, M.; Kelestemur, Y.; Demir, H. V. Stacking in Colloidal Nanoplatelets: Tuning Excitonic Properties. *ACS Nano* **2014**, *8* (12), 12524–12533.

(49) Liu, J.; Guillemeney, L.; Abécassis, B.; Coolen, L. Long Range Energy Transfer in Self-Assembled Stacks of Semiconducting Nanoplatelets. *Nano Lett.* **2020**, *20* (5), 3465–3470.

(50) Sippel, P.; Albrecht, W.; van der Bok, J. C.; Van Dijk-Moes, R. J. A.; Hannappel, T.; Eichberger, R.; Vanmaekelbergh, D. Femtosecond Cooling of Hot Electrons in CdSe Quantum-Well Platelets. *Nano Lett.* **2015**, *15* (4), 2409–2416.

(51) Pelton, M.; Ithurria, S.; Schaller, R. D.; Dolzhnikov, D. S.; Talapin, D. V. Carrier Cooling in Colloidal Quantum Wells. *Nano Lett.* **2012**, *12* (12), 6158–6163.

(52) Olutas, M.; Guzelturk, B.; Kelestemur, Y.; Yeltik, A.; Delikanli, S.; Demir, H. V. Lateral Size-Dependent Spontaneous and Stimulated Emission Properties in Colloidal CdSe Nanoplatelets. *ACS Nano* **2015**, *9* (5), 5041–5050.

(53) Gong, K.; Zeng, Y.; Kelley, D. F. Extinction Coefficients, Oscillator Strengths, and Radiative Lifetimes of CdSe, CdTe, and CdTe/CdSe Nanocrystals. *J. Phys. Chem. C* **2013**, *117* (39), 20268–20279.

(54) Li, Q.; Lian, T. Area- and Thickness-Dependent Biexciton Auger Recombination in Colloidal CdSe Nanoplatelets: Breaking the "Universal Volume Scaling Law." *Nano Lett.* **2017**, *17* (5), 3152–3158.

(55) Philbin, J. P.; Brumberg, A.; Diroll, B. T.; Cho, W.; Talapin, D. V.; Schaller, R. D.; Rabani, E. Area and Thickness Dependence of Auger Recombination in Nanoplatelets. *J. Chem. Phys.* **2020**, *153* (5), 054104.

(56) Klimov, V. I. Quantization of Multiparticle Auger Rates in Semiconductor Quantum Dots. *Science* **2000**, *287* (5455), 1011–1013.

(57) Robel, I.; Gresback, R.; Kortshagen, U.; Schaller, R. D.; Klimov, V. I. Universal Size-Dependent Trend in Auger Recombination in Direct-Gap and Indirect-Gap Semiconductor Nanocrystals. *Phys. Rev. Lett.* **2009**, *102* (17), 177404.

(58) She, C.; Fedin, I.; Dolzhnikov, D. S.; Dahlberg, P. D.; Engel, G. S.; Schaller, R. D.; Talapin, D. V. Red, Yellow, Green, and Blue Amplified Spontaneous Emission and Lasing Using Colloidal CdSe Nanoplatelets. *ACS Nano* **2015**, *9* (10), 9475–9485.

(59) Guzelturk, B.; Kelestemur, Y.; Olutas, M.; Delikanli, S.; Demir, H. V. Amplified Spontaneous Emission and Lasing in Colloidal Nanoplatelets. *ACS Nano* **2014**, *8* (7), 6599–6605.

(60) Diroll, B. T.; Fedin, I.; Darancet, P.; Talapin, D. V.; Schaller, R. D. Surface-Area-Dependent Electron Transfer Between Isoenergetic 2D Quantum Wells and a Molecular Acceptor. *J. Am. Chem. Soc.* **2016**, *138* (35), 11109–11112.

(61) Ruckebusch, C.; Sliwa, M.; Pernot, P.; de Juan, A.; Tauler, R. Comprehensive Data Analysis of Femtosecond Transient Absorption Spectra: A Review. *J. Photochem. Photobiol. C Photochem. Rev.* **2012**, *13* (1), 1–27.

(62) van Stokkum, I. H. M.; Larsen, D. S.; van Grondelle, R. Global and Target Analysis of Time-Resolved Spectra. *Biochim. Biophys. Acta BBA - Bioenerg.* **2004**, *1657* (2–3), 82–104.

(63) Dorofeev, G. A.; Streletskii, A. N.; Povstugar, I. V.; Protasov, A. V.; Elsukov, E. P. Determination of Nanoparticle Sizes by X-Ray Diffraction. *Colloid J.* **2012**, *74* (6), 675–685.

(64) Calvin, S.; Luo, S. X.; Caragianis-Broadbridge, C.; McGuinness, J. K.; Anderson, E.; Lehman, A.; Wee, K. H.; Morrison, S. A.; Kurihara, L. K. Comparison of Extended X-Ray Absorption Fine Structure and Scherrer Analysis of X-Ray Diffraction as Methods for Determining Mean Sizes of Polydisperse Nanoparticles. *Appl. Phys. Lett.* **2005**, *87* (23), 233102.

(65) Borchert, H.; Shevchenko, E. V.; Robert, A.; Mekis, I.; Kornowski, A.; Grübel, G.; Weller, H. Determination of Nanocrystal Sizes: A Comparison of TEM, SAXS, and XRD Studies of Highly Monodisperse $CoPt_3$ Particles. *Langmuir* **2005**, *21* (5), 1931–1936.

(66) Medasani, B.; Vasiliev, I. Computational Study of the Surface Properties of Aluminum Nanoparticles. *Surf. Sci.* **2009**, *603* (13), 2042–2046.

(67) Kirschner, M. S.; Hannah, D. C.; Diroll, B. T.; Zhang, X.; Wagner, M. J.; Hayes, D.; Chang, A. Y.; Rowland, C. E.; Lethiec, C. M.; Schatz, G. C.; Chen, L. X.; Schaller, R. D. Transient Melting and Recrystallization of Semiconductor Nanocrystals Under Multiple Electron–Hole Pair Excitation. *Nano Lett.* **2017**, *17* (9), 5314–5320.

(68) Kirschner, M. S.; Diroll, B. T.; Guo, P.; Harvey, S. M.; Helweh, W.; Flanders, N. C.; Brumberg, A.; Watkins, N. E.; Leonard, A. A.; Evans, A. M.; Wasielewski, M. R.; Dichtel, W. R.; Zhang, X.; Chen, L. X.; Schaller, R. D. Photoinduced, Reversible Phase Transitions in All-Inorganic Perovskite Nanocrystals. *Nat. Commun.* **2019**, *10*, 504.

(69) Harvey, S. M.; Houck, D. W.; Kirschner, M. S.; Flanders, N. C.; Brumberg, A.; Leonard, A. A.; Watkins, N. E.; Chen, L. X.; Dichtel, W. R.; Zhang, X.; Korgel, B. A.; Wasielewski, M. R.; Schaller, R. D. Transient Lattice Response upon Photoexcitation in $CuInSe_2$ Nanocrystals with Organic or Inorganic Surface Passivation. *ACS Nano* **2020**, *14* (10), 13548–13556.

(70) Brumberg, A.; Kirschner, M. S.; Diroll, B. T.; Williams, K. R.; Flanders, N. C.; Harvey, S. M.; Leonard, A. A.; Watkins, N. E.; Liu, C.; Kinigstein, E. D.; Yu, J.; Evans, A. M.; Liu, Y.; Cuthriell, S. A.; Panuganti, S.; Dichtel, W. R.; Kanatzidis, M. G.; Wasielewski, M. R.; Zhang, X.; Chen, L. X.; Schaller, R. D. Anisotropic Transient Disordering of Colloidal, Two-Dimensional CdSe Nanoplatelets upon Optical Excitation. *Nano Lett.* **2021**, *21* (3), 1288–1294.

(71) Diroll, B. T.; Brumberg, A.; Leonard, A. A.; Panuganti, S.; Watkins, N. E.; Cuthriell, S. A.; Harvey, S. M.; Kinigstein, E. D.; Yu, J.; Zhang, X.; Kanatzidis, M. G.; Wasielewski, M. R.; Chen, L. X.; Schaller, R. D. Photothermal Behaviour of Titanium Nitride

Nanoparticles Evaluated by Transient X-Ray Diffraction. *Nanoscale* **2021**, *13* (4), 2658–2664.

(72) Bertrand, G. H. V.; Polovitsyn, A.; Christodoulou, S.; Khan, A. H.; Moreels, I. Shape Control of Zincblende CdSe Nanoplatelets. *Chem. Commun.* **2016**, *52* (80), 11975–11978.

(73) Bose, S.; Song, Z.; Fan, W. J.; Zhang, D. H. Effect of Lateral Size and Thickness on the Electronic Structure and Optical Properties of Quasi Two-Dimensional CdSe and CdS Nanoplatelets. *J. Appl. Phys.* **2016**, *119* (14), 143107.

(74) Chikan, V.; Kelley, D. F. Synthesis of Highly Luminescent GaSe Nanoparticles. *Nano Lett.* **2002**, *2* (2), 141–145.

(75) Ithurria, S.; Dubertret, B. Quasi 2D Colloidal CdSe Platelets with Thicknesses Controlled at the Atomic Level. *J. Am. Chem. Soc.* **2008**, *130* (49), 16504–16505.

(76) Tyagi, P.; Arveson, S. M.; Tisdale, W. A. Colloidal Organohalide Perovskite Nanoplatelets Exhibiting Quantum Confinement. *J. Phys. Chem. Lett.* **2015**, *6* (10), 1911–1916.

(77) Benchamekh, R.; Gippius, N. A.; Even, J.; Nestoklon, M. O.; Jancu, J.-M.; Ithurria, S.; Dubertret, B.; Efros, Al. L.; Voisin, P. Tight-Binding Calculations of Image-Charge Effects in Colloidal Nanoscale Platelets of CdSe. *Phys. Rev. B* **2014**, *89* (3), 035307.

(78) Richter, M. Nanoplatelets as Material System between Strong Confinement and Weak Confinement. *Phys. Rev. Mater.* **2017**, *1* (1), 016001.

(79) Rajadell, F.; Climente, J. I.; Planelles, J. Excitons in Core-Only, Core-Shell and Core-Crown CdSe Nanoplatelets: Interplay between in-Plane Electron-Hole Correlation, Spatial Confinement, and Dielectric Confinement. *Phys. Rev. B* **2017**, *96* (3), 035307.

(80) Scott, R.; Achtstein, A. W.; Prudnikau, A. V.; Antanovich, A.; Siebbeles, L. D. A.; Artemyev, M.; Woggon, U. Time-Resolved Stark Spectroscopy in CdSe Nanoplatelets: Exciton Binding Energy, Polarizability, and Field-Dependent Radiative Rates. *Nano Lett.* **2016**, *16* (10), 6576–6583.

(81) Zhang, Y.; Mascarenhas, A. Scaling of Exciton Binding Energy and Virial Theorem in Semiconductor Quantum Wells and Wires. *Phys. Rev. B* **1999**, *59* (3), 2040–2044.

(82) Naeem, A.; Masia, F.; Christodoulou, S.; Moreels, I.; Borri, P.; Langbein, W. Giant Exciton Oscillator Strength and Radiatively Limited Dephasing in Two-Dimensional Platelets. *Phys. Rev. B* **2015**, *91* (12), 121302.

(83) Berkelbach, T. C.; Hybertsen, M. S.; Reichman, D. R. Theory of Neutral and Charged Excitons in Monolayer Transition Metal Dichalcogenides. *Phys. Rev. B* **2013**, *88* (4), 045318.

(84) Ugeda, M. M.; Bradley, A. J.; Shi, S.-F.; da Jornada, F. H.; Zhang, Y.; Qiu, D. Y.; Ruan, W.; Mo, S.-K.; Hussain, Z.; Shen, Z.-X.; Wang, F.; Louie, S. G.; Crommie, M. F. Giant Bandgap Renormalization and Excitonic Effects in a Monolayer Transition Metal Dichalcogenide Semiconductor. *Nat. Mater.* **2014**, *13* (12), 1091–1095.

(85) Tarucha, S.; Okamoto, H.; Iwasa, Y.; Miura, N. Exciton Binding Energy in GaAs Quantum Wells Deduced from Magneto-Optical Absorption Measurement. *Solid State Commun.* **1984**, *52* (9), 815–819.

(86) Tran Thoai, D. B. Exciton Binding Energy in Semiconductor Quantum Wells and in Heterostructures. *Phys. B Condens. Matter* **1990**, *164* (3), 295–299.

(87) David, A.; Miller, B. Optical Physics of Quantum Wells. In *Quantum Dynamics of Simple Systems*; Oppo, G.-L., Barnett, S. M., Riis, E., Wilkinson, M., Eds.; CRC Press: Boca Raton, FL, 2017; pp 239–266.

(88) Miller, D. A. B.; Chemla, D. S.; Damen, T. C.; Gossard, A. C.; Wiegmann, W.; Wood, T. H.; Burrus, C. A. Electric Field Dependence of Optical Absorption near the Band Gap of Quantum-Well Structures. *Phys. Rev. B* **1985**, *32* (2), 1043–1060.

(89) Stier, A. V.; McCreary, K. M.; Jonker, B. T.; Kono, J.; Crooker, S. A. Exciton Diamagnetic Shifts and Valley Zeeman Effects in Monolayer WS_2 and MoS_2 to 65 Tesla. *Nat. Commun.* **2016**, *7* (1), 10643.

(90) Stier, A. V.; Wilson, N. P.; Clark, G.; Xu, X.; Crooker, S. A. Probing the Influence of Dielectric Environment on Excitons in Monolayer WSe_2: Insight from High Magnetic Fields. *Nano Lett.* **2016**, *16* (11), 7054–7060.

(91) Stier, A. V.; Wilson, N. P.; Velizhanin, K. A.; Kono, J.; Xu, X.; Crooker, S. A. Magnetooptics of Exciton Rydberg States in a Monolayer Semiconductor. *Phys. Rev. Lett.* **2018**, *120* (5), 057405.

(92) Plechinger, G.; Nagler, P.; Arora, A.; Granados del Águila, A.; Ballottin, M. V.; Frank, T.; Steinleitner, P.; Gmitra, M.; Fabian, J.; Christianen, P. C. M.; Bratschitsch, R.; Schüller, C.; Korn, T. Excitonic Valley Effects in Monolayer WS_2 under High Magnetic Fields. *Nano Lett.* **2016**, *16* (12), 7899–7904.

(93) Chernikov, A.; Berkelbach, T. C.; Hill, H. M.; Rigosi, A.; Li, Y.; Aslan, O. B.; Reichman, D. R.; Hybertsen, M. S.; Heinz, T. F. Exciton Binding Energy and Nonhydrogenic Rydberg Series in Monolayer WS_2. *Phys. Rev. Lett.* **2014**, *113* (7), 076802.

(94) Nash, K. J.; Skolnick, M. S.; Claxton, P. A.; Roberts, J. S. Diamagnetism as a Probe of Exciton Localization in Quantum Wells. *Phys. Rev. B* **1989**, *39* (15), 10943–10954.

(95) Walck, S. N.; Reinecke, T. L. Exciton Diamagnetic Shift in Semiconductor Nanostructures. *Phys. Rev. B* **1998**, *57* (15), 9088–9096.

(96) Stier, A. V.; McCreary, K. M.; Jonker, B. T.; Kono, J.; Crooker, S. A. Magnetoreflection Spectroscopy of Monolayer Transition-Metal Dichalcogenide Semiconductors in Pulsed Magnetic Fields. *J. Vac. Sci. Technol. B Nanotechnol. Microelectron. Mater. Process. Meas. Phenom.* **2016**, *34* (4), 04J102.

(97) Bugajski, M.; Kuszko, W.; Reginski, K. Diamagnetic Shift of Exciton Energy Levels in GaAs-$Ga_{1-x}Al_xAs$ Quantum Wells. *Solid State Commun.* **1986**, *60* (8), 669–673.

(98) Shields, P. A.; Nicholas, R. J.; Grandjean, N.; Massies, J. Magneto-Photoluminescence of AlGaN/GaN Quantum Wells. *J. Cryst. Growth* **2001**, *230* (3–4), 487–491.

(99) Cunningham, P. D.; Souza, J. B.; Fedin, I.; She, C.; Lee, B.; Talapin, D. V. Assessment of Anisotropic Semiconductor Nanorod and Nanoplatelet Heterostructures with Polarized Emission for Liquid Crystal Display Technology. *ACS Nano* **2016**, *10* (6), 5769–5781.

(100) Beaudoin, E.; Davidson, P.; Abecassis, B.; Bizien, T.; Constantin, D. Reversible Strain Alignment and Reshuffling of Nanoplatelet Stacks Confined in a Lamellar Block Copolymer Matrix. *Nanoscale* **2017**, *9* (44), 17371–17377.

(101) Gao, Y.; Weidman, M. C.; Tisdale, W. A. CdSe Nanoplatelet Films with Controlled Orientation of Their Transition Dipole Moment. *Nano Lett.* **2017**, *17* (6), 3837–3843.

(102) Suarez, I.; Munoz, R.; Chirvony, V.; Martinez-Pastor, J. P.; Artemyev, M.; Prudnikau, A.; Antanovich, A.; Mikhailov, A. Multilayers of CdSe/CdS/ZnCdS Core/Wings/Shell Nanoplatelets Integrated in a Polymer Waveguide. *IEEE J. Sel. Top. Quantum Electron.* **2017**, *23* (5), 1–8.

(103) Erdem, O.; Gungor, K.; Guzelturk, B.; Tanriover, I.; Sak, M.; Olutas, M.; Dede, D.; Kelestemur, Y.; Demir, H. V. Orientation-Controlled Nonradiative Energy Transfer to Colloidal Nanoplatelets: Engineering Dipole Orientation Factor. *Nano Lett.* **2019**, *19* (7), 4297–4305.

(104) Wang, L. W.; Zunger, A. Electronic Structure Pseudopotential Calculations of Large (~1000 Atoms) Si Quantum Dots. *J. Phys. Chem.* **1994**, *98* (8), 2158–2165.

(105) Rabani, E.; Hetényi, B.; Berne, B. J.; Brus, L. E. Electronic Properties of CdSe Nanocrystals in the Absence and Presence of a Dielectric Medium. *J. Chem. Phys.* **1999**, *110* (11), 5355–5369.

(106) Rohlfing, M.; Louie, S. G. Electron-Hole Excitations and Optical Spectra from First Principles. *Phys. Rev. B* **2000**, *62* (8), 4927–4944.

(107) Chen. *Multiple Curve Fitting with Common Parameters Using NLINFIT*; 2016.

(108) Jana, S.; Phan, T. N. T.; Bouet, C.; Tessier, M. D.; Davidson, P.; Dubertret, B.; Abécassis, B. Stacking and Colloidal Stability of CdSe Nanoplatelets. *Langmuir* **2015**, *31* (38), 10532–10539.

(109) Beaudoin, E.; Abecassis, B.; Constantin, D.; Degrouard, J.; Davidson, P. Strain-Controlled Fluorescence Polarization in a CdSe Nanoplatelet–Block Copolymer Composite. *Chem. Commun.* **2015**, *51* (19), 4051–4054.

(110) Matsunaga, T.; Endo, H.; Takeda, M.; Shibayama, M. Microscopic Structure Analysis of Clay−Poly(Ethylene Oxide) Mixed Solution in a Flow Field by Contrast-Variation Small-Angle Neutron Scattering. *Macromolecules* **2010**, *43* (11), 5075–5082.

(111) Dykes, L. M. C.; Torkelson, J. M.; Burghardt, W. R.; Krishnamoorti, R. Shear-Induced Orientation in Polymer/Clay Dispersions via in Situ X-Ray Scattering. *Polymer* **2010**, *51* (21), 4916–4927.

(112) Kunneman, L. T.; Schins, J. M.; Pedetti, S.; Heuclin, H.; Grozema, F. C.; Houtepen, A. J.; Dubertret, B.; Siebbeles, L. D. A. Nature and Decay Pathways of Photoexcited States in CdSe and CdSe/CdS Nanoplatelets. *Nano Lett.* **2014**, *14* (12), 7039–7045.

(113) Morgan, D. P.; Kelley, D. F. Exciton Localization and Radiative Lifetimes in CdSe Nanoplatelets. *J. Phys. Chem. C* **2019**, *123* (30), 18665–18675.

(114) Li, Q.; Liu, Q.; Schaller, R. D.; Lian, T. Reducing the Optical Gain Threshold in Two-Dimensional CdSe Nanoplatelets by the Giant Oscillator Strength Transition Effect. *J. Phys. Chem. Lett.* **2019**, *10* (7), 1624–1632.

(115) Ayari, S.; Quick, M. T.; Owschimikow, N.; Christodoulou, S.; Bertrand, G. H. V.; Artemyev, M.; Moreels, I.; Woggon, U.; Jaziri, S.; Achtstein, A. W. Tuning Trion Binding Energy and Oscillator Strength in a Laterally Finite 2D System: CdSe Nanoplatelets as a Model System for Trion Properties. *Nanoscale* **2020**, *12* (27), 14448–14458.

(116) Halim, H.; Trieb, D.; Huber, N.; Martínez-Negro, M.; Meyer, L.-A.; Basché, T.; Morsbach, S.; Zhang, K. A. I.; Riedinger, A. Lateral Size Dependence in FRET between

Semiconductor Nanoplatelets and Conjugated Fluorophores. *J. Phys. Chem. C* **2020**, *124* (45), 25028–25037.

(117) Shin, A. J.; Hossain, A. A.; Tenney, S. M.; Tan, X.; Tan, L. A.; Foley, J. J.; Atallah, T. L.; Caram, J. R. Dielectric Screening Modulates Semiconductor Nanoplatelet Excitons. *J. Phys. Chem. Lett.* **2021**, *12* (20), 4958–4964.

(118) Law, M.; Greene, L. E.; Johnson, J. C.; Saykally, R.; Yang, P. Nanowire Dye-Sensitized Solar Cells. *Nat. Mater.* **2005**, *4* (6), 455–459.

(119) Salant, A.; Shalom, M.; Tachan, Z.; Buhbut, S.; Zaban, A.; Banin, U. Quantum Rod-Sensitized Solar Cell: Nanocrystal Shape Effect on the Photovoltaic Properties. *Nano Lett.* **2012**, *12* (4), 2095–2100.

(120) Milliron, D. J.; Hughes, S. M.; Cui, Y.; Manna, L.; Li, J.; Wang, L.-W.; Alivisatos, A. P. Colloidal Nanocrystal Heterostructures with Linear and Branched Topology. *Nature* **2004**, *430* (6996), 190–195.

(121) Kongkanand, A.; Tvrdy, K.; Takechi, K.; Kuno, M.; Kamat, P. V. Quantum Dot Solar Cells. Tuning Photoresponse through Size and Shape Control of CdSe−TiO_2 Architecture. *J. Am. Chem. Soc.* **2008**, *130* (12), 4007–4015.

(122) Benkstein, K. D.; Kopidakis, N.; van de Lagemaat, J.; Frank, A. J. Influence of the Percolation Network Geometry on Electron Transport in Dye-Sensitized Titanium Dioxide Solar Cells. *J. Phys. Chem. B* **2003**, *107* (31), 7759–7767.

(123) Mor, G. K.; Shankar, K.; Paulose, M.; Varghese, O. K.; Grimes, C. A. Use of Highly-Ordered TiO_2 Nanotube Arrays in Dye-Sensitized Solar Cells. *Nano Lett.* **2006**, *6* (2), 215–218.

(124) Gur, I. Air-Stable All-Inorganic Nanocrystal Solar Cells Processed from Solution. *Science* **2005**, *310* (5747), 462–465.

(125) Liu, R.; Bloom, B. P.; Waldeck, D. H.; Zhang, P.; Beratan, D. N. Controlling the Electron-Transfer Kinetics of Quantum-Dot Assemblies. *J. Phys. Chem. C* **2017**, *121* (27), 14401–14412.

(126) Gur, I.; Fromer, N. A.; Chen, C.-P.; Kanaras, A. G.; Alivisatos, A. P. Hybrid Solar Cells with Prescribed Nanoscale Morphologies Based on Hyperbranched Semiconductor Nanocrystals. *Nano Lett.* **2007**, *7* (2), 409–414.

(127) Milliron, D. J.; Gur, I.; Alivisatos, A. P. Hybrid Organic–Nanocrystal Solar Cells. *MRS Bull.* **2005**, *30* (1), 41–44.

(128) Zhu, H.; Song, N.; Lv, H.; Hill, C. L.; Lian, T. Near Unity Quantum Yield of Light-Driven Redox Mediator Reduction and Efficient H_2 Generation Using Colloidal Nanorod Heterostructures. *J. Am. Chem. Soc.* **2012**, *134* (28), 11701–11708.

(129) Elmalem, E.; Saunders, A. E.; Costi, R.; Salant, A.; Banin, U. Growth of Photocatalytic CdSe-Pt Nanorods and Nanonets. *Adv. Mater.* **2008**, *20* (22), 4312–4317.

(130) Zhukovskyi, M.; Tongying, P.; Yashan, H.; Wang, Y.; Kuno, M. Efficient Photocatalytic Hydrogen Generation from Ni Nanoparticle Decorated CdS Nanosheets. *ACS Catal.* **2015**, *5* (11), 6615–6623.

(131) Zhang, F.; Wang, S.; Wang, L.; Lin, Q.; Shen, H.; Cao, W.; Yang, C.; Wang, H.; Yu, L.; Du, Z.; Xue, J.; Li, L. S. Super Color Purity Green Quantum Dot Light-Emitting Diodes Fabricated by Using CdSe/CdS Nanoplatelets. *Nanoscale* **2016**, *8* (24), 12182–12188.

(132) Giovanella, U.; Pasini, M.; Lorenzon, M.; Galeotti, F.; Lucchi, C.; Meinardi, F.; Luzzati, S.; Dubertret, B.; Brovelli, S. Efficient Solution-Processed Nanoplatelet-Based Light-Emitting Diodes with High Operational Stability in Air. *Nano Lett.* **2018**, *18* (6), 3441–3448.

(133) Li, M.; Zhi, M.; Zhu, H.; Wu, W.-Y.; Xu, Q.-H.; Jhon, M. H.; Chan, Y. Ultralow-Threshold Multiphoton-Pumped Lasing from Colloidal Nanoplatelets in Solution. *Nat. Commun.* **2015**, *6* (1).

(134) Cui, Y. Nanowire Nanosensors for Highly Sensitive and Selective Detection of Biological and Chemical Species. *Science* **2001**, *293* (5533), 1289–1292.

(135) Kunneman, L. T.; Tessier, M. D.; Heuclin, H.; Dubertret, B.; Aulin, Y. V.; Grozema, F. C.; Schins, J. M.; Siebbeles, L. D. A. Bimolecular Auger Recombination of Electron–Hole Pairs in Two-Dimensional CdSe and CdSe/CdZnS Core/Shell Nanoplatelets. *J. Phys. Chem. Lett.* **2013**, *4* (21), 3574–3578.

(136) She, C.; Fedin, I.; Dolzhnikov, D. S.; Demortière, A.; Schaller, R. D.; Pelton, M.; Talapin, D. V. Low-Threshold Stimulated Emission Using Colloidal Quantum Wells. *Nano Lett.* **2014**, *14* (5), 2772–2777.

(137) Marcus, R. A. Chemical and Electrochemical Electron-Transfer Theory. *Annu. Rev. Phys. Chem.* **1964**, *15* (1), 155–196.

(138) Huang, J.; Stockwell, D.; Huang, Z.; Mohler, D. L.; Lian, T. Photoinduced Ultrafast Electron Transfer from CdSe Quantum Dots to Re-Bipyridyl Complexes. *J. Am. Chem. Soc.* **2008**, *130* (17), 5632–5633.

(139) El-Ballouli, A. O.; Alarousu, E.; Bernardi, M.; Aly, S. M.; Lagrow, A. P.; Bakr, O. M.; Mohammed, O. F. Quantum Confinement-Tunable Ultrafast Charge Transfer at the PbS Quantum Dot and Phenyl-C_{61}-Butyric Acid Methyl Ester Interface. *J. Am. Chem. Soc.* **2014**, *136* (19), 6952–6959.

(140) Zhu, H.; Yang, Y.; Hyeon-Deuk, K.; Califano, M.; Song, N.; Wang, Y.; Zhang, W.; Prezhdo, O. V.; Lian, T. Auger-Assisted Electron Transfer from Photoexcited Semiconductor Quantum Dots. *Nano Lett.* **2014**, *14* (3), 1263–1269.

(141) Olshansky, J. H.; Ding, T. X.; Lee, Y. V.; Leone, S. R.; Alivisatos, A. P. Hole Transfer from Photoexcited Quantum Dots: The Relationship between Driving Force and Rate. *J. Am. Chem. Soc.* **2015**, *137* (49), 15567–15575.

(142) Zhu, H.; Yang, Y.; Wu, K.; Lian, T. Charge Transfer Dynamics from Photoexcited Semiconductor Quantum Dots. *Annu. Rev. Phys. Chem.* **2016**, *67* (1), 259–281.

(143) Hyeon-Deuk, K.; Kim, J.; Prezhdo, O. V. Ab Initio Analysis of Auger-Assisted Electron Transfer. *J. Phys. Chem. Lett.* **2015**, *6* (2), 244–249.

(144) Graff, B. M.; Bloom, B. P.; Wierzbinski, E.; Waldeck, D. H. Electron Transfer in Nanoparticle Dyads Assembled on a Colloidal Template. *J. Am. Chem. Soc.* **2016**, *138* (40), 13260–13270.

(145) Bridewell, V. L.; Alam, R.; Karwacki, C. J.; Kamat, P. V. CdSe/CdS Nanorod Photocatalysts: Tuning the Interfacial Charge Transfer Process through Shell Length. *Chem. Mater.* **2015**, *27* (14), 5064–5071.

(146) Swarnkar, A.; Chulliyil, R.; Ravi, V. K.; Irfanullah, M.; Chowdhury, A.; Nag, A. Colloidal $CsPbBr_3$ Perovskite Nanocrystals: Luminescence beyond Traditional Quantum Dots. *Angew. Chem.* **2015**, *127* (51), 15644–15648.

(147) Li, J.; Xu, L.; Wang, T.; Song, J.; Chen, J.; Xue, J.; Dong, Y.; Cai, B.; Shan, Q.; Han, B.; Zeng, H. 50-Fold EQE Improvement up to 6.27% of Solution-Processed All-Inorganic Perovskite $CsPbBr_3$ QLEDs via Surface Ligand Density Control. *Adv. Mater.* **2017**, *29* (5), 1603885.

(148) Kulbak, M.; Cahen, D.; Hodes, G. How Important Is the Organic Part of Lead Halide Perovskite Photovoltaic Cells? Efficient $CsPbBr_3$ Cells. *J. Phys. Chem. Lett.* **2015**, *6* (13), 2452–2456.

(149) de Weerd, C.; Gomez, L.; Zhang, H.; Buma, W. J.; Nedelcu, G.; Kovalenko, M. V.; Gregorkiewicz, T. Energy Transfer between Inorganic Perovskite Nanocrystals. *J. Phys. Chem. C* **2016**, *120* (24), 13310–13315.

(150) Mondal, N.; De, A.; Samanta, A. All-Inorganic Perovskite Nanocrystal Assisted Extraction of Hot Electrons and Biexcitons from Photoexcited CdTe Quantum Dots. *Nanoscale* **2018**, *10* (2), 639–645.

(151) Dana, J.; Maity, P.; Jana, B.; Maiti, S.; Ghosh, H. N. Concurrent Ultrafast Electron- and Hole-Transfer Dynamics in $CsPbBr_3$ Perovskite and Quantum Dots. *ACS Omega* **2018**, *3* (3), 2706–2714.

(152) Yang, Y. A.; Wu, H.; Williams, K. R.; Cao, Y. C. Synthesis of CdSe and CdTe Nanocrystals without Precursor Injection. *Angew. Chem. Int. Ed.* **2005**, *44* (41), 6712–6715.

(153) Protesescu, L.; Yakunin, S.; Bodnarchuk, M. I.; Krieg, F.; Caputo, R.; Hendon, C. H.; Yang, R. X.; Walsh, A.; Kovalenko, M. V. Nanocrystals of Cesium Lead Halide Perovskites ($CsPbX_3$, X = Cl, Br, and I): Novel Optoelectronic Materials Showing Bright Emission with Wide Color Gamut. *Nano Lett.* **2015**, *15* (6), 3692–3696.

(154) Bertolotti, F.; Nedelcu, G.; Vivani, A.; Cervellino, A.; Masciocchi, N.; Guagliardi, A.; Kovalenko, M. V. Crystal Structure, Morphology, and Surface Termination of Cyan-Emissive, Six-Monolayers-Thick $CsPbBr_3$ Nanoplatelets from X-Ray Total Scattering. *ACS Nano* **2019**, *13* (12), 14294–14307.

(155) Jasieniak, J.; Smith, L.; van Embden, J.; Mulvaney, P.; Califano, M. Re-Examination of the Size-Dependent Absorption Properties of CdSe Quantum Dots. *J. Phys. Chem. C* **2009**, *113* (45), 19468–19474.

(156) Makarov, N. S.; Guo, S.; Isaienko, O.; Liu, W.; Robel, I.; Klimov, V. I. Spectral and Dynamical Properties of Single Excitons, Biexcitons, and Trions in Cesium–Lead-Halide Perovskite Quantum Dots. *Nano Lett.* **2016**, *16* (4), 2349–2362.

(157) Shevchenko, E. V.; Talapin, D. V.; Kotov, N. A.; O'Brien, S.; Murray, C. B. Structural Diversity in Binary Nanoparticle Superlattices. *Nature* **2006**, *439* (7072), 55–59.

(158) Overgaag, K.; Evers, W.; de Nijs, B.; Koole, R.; Meeldijk, J.; Vanmaekelbergh, D. Binary Superlattices of PbSe and CdSe Nanocrystals. *J. Am. Chem. Soc.* **2008**, *130* (25), 7833–7835.

(159) Chen, Z.; Moore, J.; Radtke, G.; Sirringhaus, H.; O'Brien, S. Binary Nanoparticle Superlattices in the Semiconductor−Semiconductor System: CdTe and CdSe. *J. Am. Chem. Soc.* **2007**, *129* (50), 15702–15709.

(160) Ravi, V. K.; Markad, G. B.; Nag, A. Band Edge Energies and Excitonic Transition Probabilities of Colloidal $CsPbX_3$ (X = Cl, Br, I) Perovskite Nanocrystals. *ACS Energy Lett.* **2016**, *1* (4), 665–671.

(161) Spittel, D.; Poppe, J.; Meerbach, C.; Ziegler, C.; Hickey, S. G.; Eychmüller, A. Absolute Energy Level Positions in CdSe Nanostructures from Potential-Modulated Absorption Spectroscopy (EMAS). *ACS Nano* **2017**, *11* (12), 12174–12184.

(162) Morgan, D. P.; Maddux, C. J. A.; Kelley, D. F. Transient Absorption Spectroscopy of CdSe Nanoplatelets. *J. Phys. Chem. C* **2018**, *122* (41), 23772–23779.

(163) Grimaldi, G.; Geuchies, J. J.; van der Stam, W.; du Fossé, I.; Brynjarsson, B.; Kirkwood, N.; Kinge, S.; Siebbeles, L. D. A.; Houtepen, A. J. Spectroscopic Evidence for the Contribution of Holes to the Bleach of Cd-Chalcogenide Quantum Dots. *Nano Lett.* **2019**, *19* (5), 3002–3010.

(164) Hunsche, S.; Dekorsy, T.; Klimov, V.; Kurz, H. Ultrafast Dynamics of Carrier-Induced Absorption Changes in Highly-Excited CdSe Nanocrystals. *Appl. Phys. B Laser Opt.* **1996**, *62* (1), 3–10.

(165) Infelta, P. P.; Gratzel, M.; Thomas, J. K. Luminescence Decay of Hydrophobic Molecules Solubilized in Aqueous Micellar Systems. A Kinetic Model. *J. Phys. Chem.* **1974**, *78* (2), 190–195.

(166) Yang, M.; Moroz, P.; Miller, E.; Porotnikov, D.; Cassidy, J.; Ellison, C.; Medvedeva, X.; Klinkova, A.; Zamkov, M. Energy Transport in $CsPbBr_3$ Perovskite Nanocrystal Solids. *ACS Photonics* **2020**, *7* (1), 154–164.

(167) Loiudice, A.; Saris, S.; Buonsanti, R. Tunable Metal Oxide Shell as a Spacer to Study Energy Transfer in Semiconductor Nanocrystals. *J. Phys. Chem. Lett.* **2020**, *11* (9), 3430–3435.

(168) Momper, R.; Zhang, H.; Chen, S.; Halim, H.; Johannes, E.; Yordanov, S.; Braga, D.; Blülle, B.; Doblas, D.; Kraus, T.; Bonn, M.; Wang, H. I.; Riedinger, A. Kinetic Control over Self-Assembly of Semiconductor Nanoplatelets. *Nano Lett.* **2020**, *20* (6), 4102–4110.

(169) Bai, P.; Hu, A.; Liu, Y.; Jin, Y.; Gao, Y. Printing and *In Situ* Assembly of CdSe/CdS Nanoplatelets as Uniform Films with Unity In-Plane Transition Dipole Moment. *J. Phys. Chem. Lett.* **2020**, *11* (11), 4524–4529.

(170) Ryu, H.-Y.; Kim, H.-S.; Shim, J.-I. Rate Equation Analysis of Efficiency Droop in InGaN Light-Emitting Diodes. *Appl. Phys. Lett.* **2009**, *95* (8), 081114.

(171) Kioupakis, E.; Rinke, P.; Delaney, K. T.; Van de Walle, C. G. Indirect Auger Recombination as a Cause of Efficiency Droop in Nitride Light-Emitting Diodes. *Appl. Phys. Lett.* **2011**, *98* (16), 161107.

(172) Cho, J.; Schubert, E. F.; Kim, J. K. Efficiency Droop in Light-Emitting Diodes: Challenges and Countermeasures. *Laser Photonics Rev.* **2013**, *7* (3), 408–421.

(173) Vaxenburg, R.; Lifshitz, E.; Efros, Al. L. Suppression of Auger-Stimulated Efficiency Droop in Nitride-Based Light Emitting Diodes. *Appl. Phys. Lett.* **2013**, *102* (3), 031120.

(174) Lim, J.; Park, Y.-S.; Wu, K.; Yun, H. J.; Klimov, V. I. Droop-Free Colloidal Quantum Dot Light-Emitting Diodes. *Nano Lett.* **2018**, *18* (10), 6645–6653.

(175) Pan, J. L. Reduction of the Auger Rate in Semiconductor Quantum Dots. *Phys. Rev. B* **1992**, *46* (7), 3977–3998.

(176) Klimov, V. I.; McBranch, D. W.; Leatherdale, C. A.; Bawendi, M. G. Electron and Hole Relaxation Pathways in Semiconductor Quantum Dots. *Phys. Rev. B* **1999**, *60* (19), 13740–13749.

(177) Haug, A. Band-to-Band Auger Recombination in Semiconductors. *J. Phys. Chem. Solids* **1988**, *49* (6), 599–605.

(178) Li, Y.; Ding, T.; Luo, X.; Chen, Z.; Liu, X.; Lu, X.; Wu, K. Biexciton Auger Recombination in Mono-Dispersed, Quantum-Confined CsPbBr3 Perovskite Nanocrystals Obeys Universal Volume-Scaling. *Nano Res.* **2019**, *12* (3), 619–623.

(179) Kobayashi, Y.; Tamai, N. Size-Dependent Multiexciton Spectroscopy and Moderate Temperature Dependence of Biexciton Auger Recombination in Colloidal CdTe Quantum Dots. *J. Phys. Chem. C* **2010**, *114* (41), 17550–17556.

(180) Hyeon-Deuk, K.; Kobayashi, Y.; Tamai, N. Evidence of Phonon-Assisted Auger Recombination and Multiple Exciton Generation in Semiconductor Quantum Dots Revealed by Temperature-Dependent Phonon Dynamics. *J. Phys. Chem. Lett.* **2014**, *5* (1), 99–105.

(181) Li, Q.; Yang, Y.; Que, W.; Lian, T. Size- and Morphology-Dependent Auger Recombination in $CsPbBr_3$ Perovskite Two-Dimensional Nanoplatelets and One-Dimensional Nanorods. *Nano Lett.* **2019**, *19* (8), 5620–5627.

(182) Grim, J. Q.; Christodoulou, S.; Di Stasio, F.; Krahne, R.; Cingolani, R.; Manna, L.; Moreels, I. Continuous-Wave Biexciton Lasing at Room Temperature Using Solution-Processed Quantum Wells. *Nat. Nanotechnol.* **2014**, *9* (11), 891–895.

(183) Baghani, E.; O'Leary, S. K.; Fedin, I.; Talapin, D. V.; Pelton, M. Auger-Limited Carrier Recombination and Relaxation in CdSe Colloidal Quantum Wells. *J. Phys. Chem. Lett.* **2015**, *6* (6), 1032–1036.

(184) Pelton, M.; Andrews, J. J.; Fedin, I.; Talapin, D. V.; Leng, H.; O'Leary, S. K. Nonmonotonic Dependence of Auger Recombination Rate on Shell Thickness for CdSe/CdS Core/Shell Nanoplatelets. *Nano Lett.* **2017**, *17* (11), 6900–6906.

(185) Philbin, J. P.; Rabani, E. Electron–Hole Correlations Govern Auger Recombination in Nanostructures. *Nano Lett.* **2018**, *18* (12), 7889–7895.

(186) Philbin, J. P.; Rabani, E. Auger Recombination Lifetime Scaling for Type I and Quasi-Type II Core/Shell Quantum Dots. *J. Phys. Chem. Lett.* **2020**, *11* (13), 5132–5138.

(187) Brumberg, A.; Harvey, S. M.; Philbin, J. P.; Diroll, B. T.; Lee, B.; Crooker, S. A.; Wasielewski, M. R.; Rabani, E.; Schaller, R. D. Determination of the In-Plane Exciton Radius in 2D CdSe Nanoplatelets *via* Magneto-Optical Spectroscopy. *ACS Nano* **2019**, *13* (8), 8589–8596.

(188) Manzeli, S.; Ovchinnikov, D.; Pasquier, D.; Yazyev, O. V.; Kis, A. 2D Transition Metal Dichalcogenides. *Nat. Rev. Mater.* **2017**, *2* (8).

(189) Xia, F.; Wang, H.; Jia, Y. Rediscovering Black Phosphorus as an Anisotropic Layered Material for Optoelectronics and Electronics. *Nat. Commun.* **2014**, *5* (1).

(190) Berger, C.; Song, Z.; Li, T.; Li, X.; Ogbazghi, A. Y.; Feng, R.; Dai, Z.; Marchenkov, A. N.; Conrad, E. H.; First, P. N.; de Heer, W. A. Ultrathin Epitaxial Graphite: 2D Electron Gas Properties and a Route toward Graphene-Based Nanoelectronics. *J. Phys. Chem. B* **2004**, *108* (52), 19912–19916.

(191) Butler, S. Z.; Hollen, S. M.; Cao, L.; Cui, Y.; Gupta, J. A.; Gutiérrez, H. R.; Heinz, T. F.; Hong, S. S.; Huang, J.; Ismach, A. F.; Johnston-Halperin, E.; Kuno, M.; Plashnitsa, V. V.; Robinson, R. D.; Ruoff, R. S.; Salahuddin, S.; Shan, J.; Shi, L.; Spencer, M. G.; Terrones, M.; Windl, W.; Goldberger, J. E. Progress, Challenges, and Opportunities in Two-Dimensional Materials Beyond Graphene. *ACS Nano* **2013**, *7* (4), 2898–2926.

(192) Jariwala, D.; Sangwan, V. K.; Lauhon, L. J.; Marks, T. J.; Hersam, M. C. Emerging Device Applications for Semiconducting Two-Dimensional Transition Metal Dichalcogenides. *ACS Nano* **2014**, *8* (2), 1102–1120.

(193) Schwierz, F.; Pezoldt, J.; Granzner, R. Two-Dimensional Materials and Their Prospects in Transistor Electronics. *Nanoscale* **2015**, *7* (18), 8261–8283.

(194) Wang, Q. H.; Kalantar-Zadeh, K.; Kis, A.; Coleman, J. N.; Strano, M. S. Electronics and Optoelectronics of Two-Dimensional Transition Metal Dichalcogenides. *Nat. Nanotechnol.* **2012**, *7* (11), 699–712.

(195) Antanovich, A.; Achtstein, A. W.; Matsukovich, A.; Prudnikau, A.; Bhaskar, P.; Gurin, V.; Molinari, M.; Artemyev, M. A Strain-Induced Exciton Transition Energy Shift in CdSe Nanoplatelets: The Impact of an Organic Ligand Shell. *Nanoscale* **2017**, *9* (45), 18042–18053.

(196) Dufour, M.; Qu, J.; Greboval, C.; Méthivier, C.; Lhuillier, E.; Ithurria, S. Halide Ligands To Release Strain in Cadmium Chalcogenide Nanoplatelets and Achieve High Brightness. *ACS Nano* **2019**, *13* (5), 5326–5334.

(197) Diroll, B. T.; Schaller, R. D. Shape-Selective Optical Transformations of CdSe Nanoplatelets Driven by Halide Ion Ligand Exchange. *Chem. Mater.* **2019**, *31* (9), 3556–3563.

(198) Diroll, B. T. Ligand-Dependent Tuning of Interband and Intersubband Transitions of Colloidal CdSe Nanoplatelets. *Chem. Mater.* **2020**.

(199) Polovitsyn, A.; Dang, Z.; Movilla, J. L.; Martín-García, B.; Khan, A. H.; Bertrand, G. H. V.; Brescia, R.; Moreels, I. Synthesis of Air-Stable CdSe/ZnS Core–Shell Nanoplatelets with Tunable Emission Wavelength. *Chem. Mater.* **2017**, *29* (13), 5671–5680.

(200) Tenne, R.; Pedetti, S.; Kazes, M.; Ithurria, S.; Houben, L.; Nadal, B.; Oron, D.; Dubertret, B. From Dilute Isovalent Substitution to Alloying in CdSeTe Nanoplatelets. *Phys. Chem. Chem. Phys.* **2016**, *18* (22), 15295–15303.

(201) Liu, B.; Altintas, Y.; Wang, L.; Shendre, S.; Sharma, M.; Sun, H.; Mutlugun, E.; Demir, H. V. Record High External Quantum Efficiency of 19.2% Achieved in Light-Emitting Diodes of Colloidal Quantum Wells Enabled by Hot-Injection Shell Growth. *Adv. Mater.* **2020**, *32* (8), 1905824.

(202) Meyer, J. R.; Bartoli, F. J.; Kruer, M. R. Optical Heating in Semiconductors. *Phys. Rev. B* **1980**, *21* (4), 1559–1568.

(203) Sadasivam, S.; Chan, M. K. Y.; Darancet, P. Theory of Thermal Relaxation of Electrons in Semiconductors. *Phys. Rev. Lett.* **2017**, *119* (13).

(204) Kirschner, M. S.; Diroll, B. T.; Brumberg, A.; Leonard, A. A.; Hannah, D. C.; Chen, L. X.; Schaller, R. D. Optical Signatures of Transiently Disordered Semiconductor Nanocrystals. *ACS Nano* **2018**, *12* (10), 10008–10015.

(205) Ong, W.-L.; Rupich, S. M.; Talapin, D. V.; McGaughey, A. J. H.; Malen, J. A. Surface Chemistry Mediates Thermal Transport in Three-Dimensional Nanocrystal Arrays. *Nat. Mater.* **2013**, *12* (5), 410–415.

(206) Goldstein, A. N.; Echer, C. M.; Alivisatos, A. P. Melting in Semiconductor Nanocrystals. *Science* **1992**, *256* (5062), 1425–1427.

(207) Liu, M.; Wang, R. Y. Size-Dependent Melting Behavior of Colloidal In, Sn and Bi Nanocrystals. *Sci. Rep.* **2015**, *5*, 16353.

(208) Robinson, I. Nanoparticle Structure by Coherent X-Ray Diffraction. *J. Phys. Soc. Jpn.* **2013**, *82* (2), 021012.

(209) Barnard, A. S.; Zapol, P. A Model for the Phase Stability of Arbitrary Nanoparticles as a Function of Size and Shape. *J. Chem. Phys.* **2004**, *121* (9), 4276–4283.

(210) Rowland, C. E.; Fedin, I.; Diroll, B. T.; Liu, Y.; Talapin, D. V.; Schaller, R. D. Elevated Temperature Photophysical Properties and Morphological Stability of CdSe and CdSe/CdS Nanoplatelets. *J. Phys. Chem. Lett.* **2018**, *9* (2), 286–293.

(211) Mannebach, E. M.; Li, R.; Duerloo, K.-A.; Nyby, C.; Zalden, P.; Vecchione, T.; Ernst, F.; Reid, A. H.; Chase, T.; Shen, X.; Weathersby, S.; Hast, C.; Hettel, R.; Coffee, R.; Hartmann, N.; Fry, A. R.; Yu, Y.; Cao, L.; Heinz, T. F.; Reed, E. J.; Dürr, H. A.; Wang, X.; Lindenberg, A. M. Dynamic Structural Response and Deformations of Monolayer

MoS_2 Visualized by Femtosecond Electron Diffraction. *Nano Lett.* **2015**, *15* (10), 6889–6895.

(212) Tung, I.-C.; Krishnamoorthy, A.; Sadasivam, S.; Zhou, H.; Zhang, Q.; Seyler, K. L.; Clark, G.; Mannebach, E. M.; Nyby, C.; Ernst, F.; Zhu, D.; Glownia, J. M.; Kozina, M. E.; Song, S.; Nelson, S.; Kumazoe, H.; Shimojo, F.; Kalia, R. K.; Vashishta, P.; Darancet, P.; Heinz, T. F.; Nakano, A.; Xu, X.; Lindenberg, A. M.; Wen, H. Anisotropic Structural Dynamics of Monolayer Crystals Revealed by Femtosecond Surface X-Ray Scattering. *Nat. Photonics* **2019**, *13* (6), 425–430.

(213) Hu, J.; Vanacore, G. M.; Cepellotti, A.; Marzari, N.; Zewail, A. H. Rippling Ultrafast Dynamics of Suspended 2D Monolayers, Graphene. *Proc. Natl. Acad. Sci.* **2016**, *113* (43), E6555–E6561.

(214) Miró, P.; Ghorbani-Asl, M.; Heine, T. Spontaneous Ripple Formation in MoS_2 Monolayers: Electronic Structure and Transport Effects. *Adv. Mater.* **2013**, *25* (38), 5473–5475.

(215) Shcherbinin, S. A.; Zhou, K.; Dmitriev, S. V.; Korznikova, E. A.; Davletshin, A. R.; Kistanov, A. A. Two-Dimensional Black Phosphorus Carbide: Rippling and Formation of Nanotubes. *J. Phys. Chem. C* **2020**, *124* (18), 10235–10243.

(216) Jurgilaitis, A.; Enquist, H.; Andreasson, B. P.; Persson, A. I. H.; Borg, B. M.; Caroff, P.; Dick, K. A.; Harb, M.; Linke, H.; Nüske, R.; Wernersson, L.-E.; Larsson, J. Time-Resolved X-Ray Diffraction Investigation of the Modified Phonon Dispersion in InSb Nanowires. *Nano Lett.* **2014**, *14* (2), 541–546.

(217) Wittenberg, J. S.; Miller, T. A.; Szilagyi, E.; Lutker, K.; Quirin, F.; Lu, W.; Lemke, H.; Zhu, D.; Chollet, M.; Robinson, J.; Wen, H.; Sokolowski-Tinten, K.; Alivisatos, A. P.; Lindenberg, A. M. Real-Time Visualization of Nanocrystal Solid–Solid Transformation Pathways. *Nano Lett.* **2014**, *14* (4), 1995–1999.

(218) Szilagyi, E.; Wittenberg, J. S.; Miller, T. A.; Lutker, K.; Quirin, F.; Lemke, H.; Zhu, D.; Chollet, M.; Robinson, J.; Wen, H.; Sokolowski-Tinten, K.; Lindenberg, A. M.

Visualization of Nanocrystal Breathing Modes at Extreme Strains. *Nat. Commun.* **2015**, *6* (1).

(219) Joffre, M.; Hulin, D.; Migus, A.; Antonetti, A. Dynamics of the Optical Stark Effect in Semiconductors. *J. Mod. Opt.* **1988**, *35* (12), 1951–1964.

(220) Li, Z.; Peng, X. Size/Shape-Controlled Synthesis of Colloidal CdSe Quantum Disks: Ligand and Temperature Effects. *J. Am. Chem. Soc.* **2011**, *133* (17), 6578–6586.

(221) Chen, D.; Gao, Y.; Chen, Y.; Ren, Y.; Peng, X. Structure Identification of Two-Dimensional Colloidal Semiconductor Nanocrystals with Atomic Flat Basal Planes. *Nano Lett.* **2015**, *15* (7), 4477–4482.

(222) Tomar, R.; Kulkarni, A.; Chen, K.; Singh, S.; van Thourhout, D.; Hodgkiss, J. M.; Siebbeles, L. D. A.; Hens, Z.; Geiregat, P. Charge Carrier Cooling Bottleneck Opens Up Nonexcitonic Gain Mechanisms in Colloidal CdSe Quantum Wells. *J. Phys. Chem. C* **2019**, *123* (14), 9640–9650.